A FINITE ELEMENT STUDY OF HUMAN THIGH AREA IN SEATED POSTURE FOR PRESSURE ULCER PREDICTION AND PREVENTION

By

Sheng Chen

A DISSERTATION

Submitted to
Michigan State University
in partial fulfillment of the requirements
for the degree of

Mechanical Engineering – Doctor of Philosophy

2019

ABSTRACT

A FINITE ELEMENT STUDY OF HUMAN THIGH AREA IN SEATED POSTURE FOR
PRESSURE ULCER PREDICTION AND PREVENTION

By

Sheng Chen

Pressure ulcers (PUs), also known as pressure sores, are localized damage to the skin and underlying tissues, usually occurring over a bony prominence and caused by sitting or lying in one position for long time. PUs are a detriment to the well-being of people who lose their mobility either permanently or temporarily, and high morbidity and mortality are associated with PUs. Although the initiating mechanism of PUs is still unclear, it is commonly accepted that internal normal and shear stresses, due to the presence of unrelieved external loads, play a central role in the formation and development of these wounds. Despite the significance of internal stresses in PUs formation, interfacial pressures, which are a surface measure of stress, are the indicators commonly used to develop practices and protocols to minimize loading on the soft tissue. However, no direct correlation exists between interfacial pressure and internal stresses of soft tissue. Therefore, tools and methods that can show internal distributions of soft tissue's stresses and strains as a response to external loading are needed.

The ability of finite element (FE) models to accurately represent the anatomical structure of the leg and buttocks area and to estimate the localized stress/strain fields within highly deformable media, makes them powerful tools to investigate soft tissue response to external loadings. Despite the significant advancement previous studies have achieved, there are still important aspects in human thigh-buttock soft tissue modeling area that need to be improved. Two challenges are identified in this dissertation: 1) Microstructurally motivated skin modeling for an individual skin layer in finite element model. 2) Parameters estimation associated with large deformations.

To address the first challenge, a microstructurally based constitutive model is proposed to describe the mechanical behavior of skin. The constitutive model incorporated the distribution of collagen fiber bundle orientations and relative collagen content measured from histology, and shows good agreement with the tensile test data.

To address the second challenge, an optimization procedure that is able to match nonlinear behaviors between FE simulation and *in vivo* experimental data is developed. The difference between 3D and semi-3D model is quantified, and the accuracy of four commonly used constitutive model representing soft tissue nonlinear mechanical behavior is compared.

Finally, a thigh FE model that has detailed anatomical representation of different soft tissue types, i.e., skin, fat, and muscle, is developed. The subject-specific *in vivo* experimental data are used to inform the optimization procedure to obtain best-fit constitutive parameters for different soft tissue types. The research in this dissertation provides an approach to describe the *in vivo* mechanical behavior of soft tissues in thigh-buttock area accurately through FE modeling. The constitutive parameters informed by *in vivo* data in this dissertation are valuable to facilitate future FE modeling studies to achieve accurate internal stress/strain distribution of soft tissues in thigh-buttock area.

To my parents and my wife.

ACKNOWLEDGEMENTS

I would like to thank my advisor, Dr. Sara Roccabianca, who has been a great mentor and a dear friend to me while pursuing my PhD. Her patient guidance, rich knowledge, positive energy and hard-working spirit motivated me along this journey.

I would also like to thank my dissertation committee, Dr. Tamara Reid Bush, Dr. Seungik Baek, and Dr. Weiyi Lu for their guidance and insights on my research.

Last but not least, I would like to thank my parents and wife, for their endless love and support.

TABLE OF CONTENTS

LIST OF TABLES

animal 5, while transverse experimental data are from animal 10. Best-fit constitutive parameters of the simulated stress-stretch curves shown in the figure are as follows. Upper back sample in axial direction (animal 5) $c^{gm} = 3.07\ MPa$, $c_1 = 53.27\ MPa$, $c_2 = 51.26$, $G_q = 0.977$; and transverse direction (animal 10) $c^{gm} = 0.82\ MPa$, $c_1 = 65.62MPa$, $c_2 = 38.06$, $G_q = 0.952$. Lower back sample in axial direction (animal 5) $c^{gm} = 5.91\ MPa$, $c_1 = 69.94\ MPa$, $c_2 = 32.33$, $G_q = 0.978$; and transverse direction (animal 10) $c^{gm} = 0.72\ MPa$, $c_1 = 10.71\ MPa$, $c_2 = 66.88$, $G_q = 0.976$.. 41

1. INTRODUCTION AND LITERATURE REVIEW

1.1. Overview

Pressure ulcers (PUs), also known as pressure sores, are localized damage to the skin and underlying tissues, usually occurring over a bony prominence and caused by sitting or lying in one position for long time. People with reduced mobility are critically vulnerable to PUs, including elders, people with spinal cord injuries, and people temporarily disabled due to diseases or medical treatments. PUs are a detriment to the well-being of people who lose their mobility either permanently or temporarily, and high morbidity and mortality are associated with PUs [1]. Each year in the US an estimated 2.5 million people develop PUs [2]. In the year 2013, almost 30,000 deaths were caused by complications associated with this condition globally [3]. Further, the healing time of PUs can be long, ranging from several weeks to several months, depending on the stage of the ulcer and factors like age and other medical complications. Even when healing occurs, it is often not complete, leading to a high reoccurrence rate [4].

Several hypotheses have been made on the biomechanical mechanism involved with the formation of PUs. These include cellular death due to mechanical distortion [5], tissue decay due to reduced interstitial flow and lymphatic drainage [6] or reduced blood perfusion [7], and localized ischemia [8], [9]. Although the initiating mechanism of PUs is still unclear, it is commonly accepted that internal normal and shear stresses, due to the presence of unrelieved external loads, play a central role in the formation and development of these wounds [9]–[12]. Therefore, it is crucial to evaluate the internal stresses caused by the physiological loading associated with sitting or lying down to assess the risk of tissue injury. Despite the significance of internal stresses in PUs formation, interfacial pressures, which are a surface measure of stress, are the indicators commonly used to develop practices and protocols to minimize loading on the soft

1

tissue, for example for timing between posture changing or for the selection of materials for hospital mattresses [13], [14]. However, previous published studies, that focused both on animal [15] and numerical models [16], [17], have pointed out that no direct correlation exists between interfacial pressure and internal stresses of soft tissue. Therefore, tools and methods that can show internal distributions of soft tissue's stresses and strains as a response to external loading are needed.

The ability of finite element (FE) models to accurately represent the anatomical structure of the leg and buttocks area and to estimate the localized stress/strain fields within highly deformable media, makes them powerful tools to investigate soft tissue response to external loadings [18]. Indeed, FE models were employed in previous studies to identify and investigate external and internal factors that may affect stress/strain distributions within the soft tissue during sitting [19]–[21], a position in which both disabled and normal people spend majority of time during the day [22]–[25]. Despite the significant advancement previous studies have achieved, there are still important aspects in human thigh-buttock soft tissue modeling area that need to be improved. Two challenges are identified in this dissertation: 1) Microstructurally motivated skin modeling for an individual skin layer in finite element model. 2) Parameters estimation associated with large deformations.

1.2. Skin mechanical model

In the past 20 years, there has been a growing effort on developing more anatomically accurate FE models, however, one component that has still been significantly overlooked in this effort is the skin. This might be due to the fact that FE models have been mostly used as a tool to assess the stresses and strains in deep tissue, because deep tissue injuries are harder to detect compared to superficially formed PUs. However, superficially formed PUs, which are more involved with

friction and shear forces are also a major form of PUs [26]. Previous FE studies either model the bulk properties of all soft tissues (i.e., skin, fat, muscle) together [21], [27], or model skin and fat as one component [19], [28]. The only few studies that modeled the skin separately used simple phenomenological constitutive models [16], [20]. A separate, accurate representation of the skin in a FE model is important to investigate PUs formation due to the following reasons:

(1) *Different mechanical properties of tissues*. Skin is a very thin layer compared to muscle and fat. Collagen fibers in skin, which are the main weight-bearing structure, have preferred directions parallel to the surface [29]. Hence, mechanical response from the skin layer may come from extension rather than compression during sitting contact.

(2) *Different vulnerability to pressure*. Due to the differences in composition, structure, and metabolic rate, different tissues (i.e., muscle, fat and skin) may have different pressure tolerance [30]. Thus, stress or strain threshold criteria for PUs formation should be considered for different types of tissues separately, both in experimental testing and in numerical simulation.

Skin microstructure. Skin is a thin, multilayered membrane that acts as the body's major barrier, both biologically and mechanically, against the external environment by fulfilling multiple biological purposes (i.e., regulation of heat and water exchange with the surroundings, protection from mechanical, bacterial or viral insults). Its structure can be approximately subdivided in three principal layers: the epidermis, the dermis and the hypodermis. The outermost layer (epidermis) is a thin cellular membrane that serves as a barrier but does not contribute to the mechanical behaviors. The middle layer (dermis) is mostly composed by a matrix of collagen and elastin fibers,
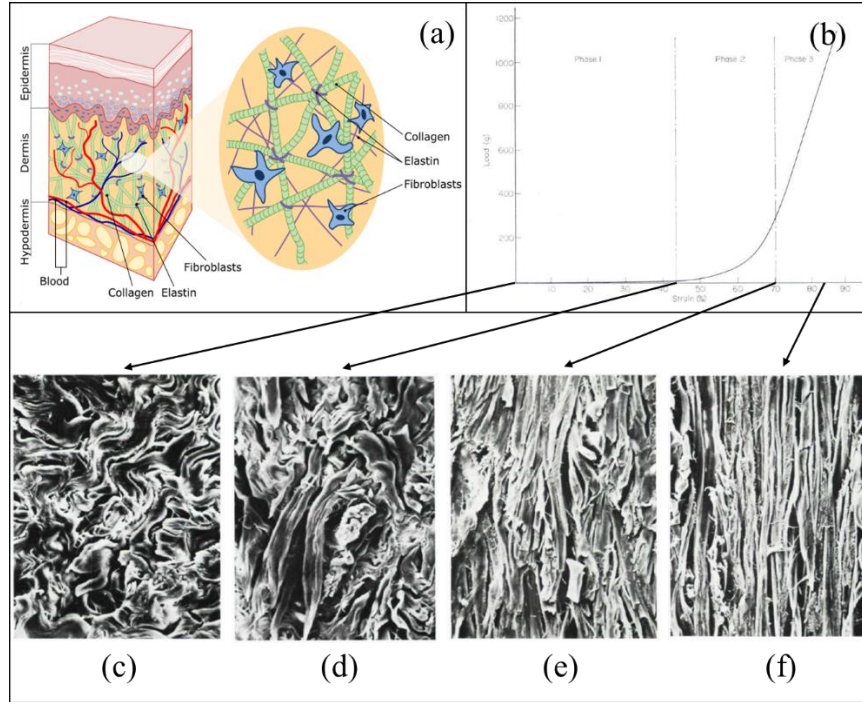
Figure 1. (**a**) Schematic of skin structure. (**b**) A typical load-strain graph obtained in an *in vitro* uniaxial test of human abdominal skin, three phases of extension are indicated in the graph. (**c-f**) Collagen network, parallel section through mid-dermis, under the scanning electron microscope at different strain levels. (**c**) Unstressed skin, collagen fibers appear wavy and multidirectional. (**d**) Strain level corresponding to the end of phase 1, fibers have reoriented towards load axis. (**e**) Strain level corresponding to the end of phase 2, fibers appear aligned in the direction of the load and almost straight. (**f**) Strain level corresponding to mid-phase 3, fibers appear aligned, straight, and compacted. Pictures (**b-f**) from [31], numbering changed from original.

and endows strength and compliance to the skin. The innermost layer (hypodermis) serves as a supportive substratum and is primarily made of adipose tissue (**Figure 1 a**). Collagen is the major load-bearing constituent of the dermis and accounts for approximately 60%~80% of skin dry weight [32], [33]. Brown [31] examined the structure of human skin under scanning electron microscopy. His study showed that the nonlinear stress-strain response of skin (**Figure 1 b**) is due to the re-orientation, alignment, and straightening of undulated collagen fibers during extension (**Figure 1 c – f**). A study by Finlay [34] showed that anisotropy of skin is attributed to the non-uniform distribution of collagen fiber orientation. These observations demonstrate the important role collagen fibers play in skin mechanical behavior. As a result, the quantification of the collagen network structure is considered a key step in the development of a microstructural model of skin
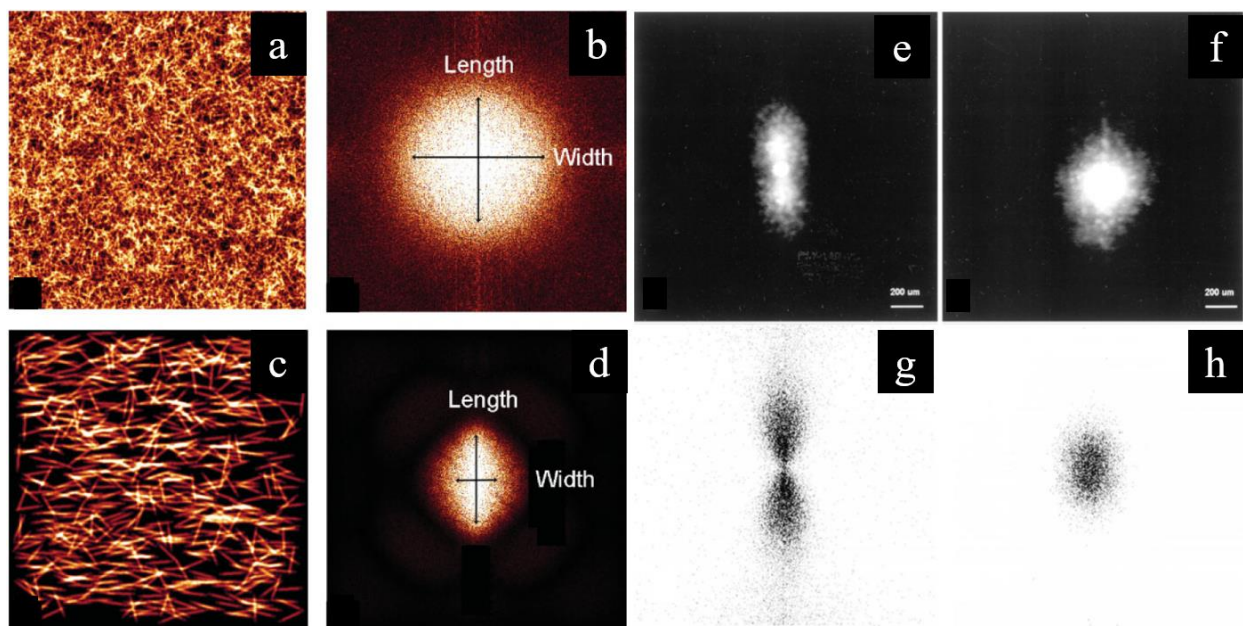
Figure 2. Computer-generated images (**a, c**) and the power plots of Fourier analysis (**b, d**) previously published in [35]. Specifically, (**a**) and (**c**) show two examples of the computer-generated images, which were used to validate the accuracy of Fourier analysis generated power plots in representing fiber orientation preference. The images consist of ellipses with a width/length ratio of 1:10. (**b**) and (**d**) are the power plot generated by Fourier analysis, of (**a**) and (**c**), respectively. The network represented in (**b**) corresponds to an orientation index of 1, and the network represented in (**d**) corresponds to an orientation index of 0. (**e-h**) Laser scatter images and first-order power plots previously published in [36]. (**e**) The laser scatter image of lesional sclerodermic skin (LS) produces an elongated scatter plot, indicating a higher orientation of collagen bundles when compared to control skin (CS), shown in (**f**), which produces a circular scatter plot. (**g-h**) First-order power plots from the fast Fourier transform of the images shown in (**e-f**). (**g**) LS creates a power plot with a preferential distribution with two maxima, and CS, shown in (**h**) is characterized by a power plot with a circular pattern. Numbering changed from original studies.

mechanical behavior. For example, van Zuijlen *et al.* [35] developed an image analysis technique that used Fourier analysis to assess collagen orientation on image of human skin acquired by confocal laser scanning microscopy. The fiber orientation index was evaluated by calculating the width to length ratio of the power plot of histology images generated by Fourier analysis (**Figure 2 a-d**). The orientation index ranges between 0 and 1, which represents the cases of perfectly aligned fibers and randomly distributed fibers, respectively. In another study, Vries *et al.* [36] used two methods, specifically the laser scatter method and the fast Fourier transform (FFT), to describe collagen orientation, then collagen structure indicators, such as orientation ratio, orientation variation, and bundle spacing, were evaluated based on the laser scatter images and FFT power

plots (**Figure 2 e-h**). These studies, however, provided mostly qualitative measurement that indicated the preferential direction or level of anisotropy of the collagen network, rather than quantitative measurement. Studies that quantified collagen orientation distribution which could be implemented into structural constitutive model are still rare [37], [38].

Skin constitutive modeling. Skin is a nonlinear, anisotropic, and viscoelastic material and different models have been developed to describe several aspects of skin mechanical behavior [38]–[45]. The literature review that follows discusses papers that mainly focus on two aspects: (1) the development of nonlinear and anisotropic constitutive model of skin, and (2) experimental measures of collagen microstructural organization.

Skin constitutive models can be categorized into two types: phenomenological models and microstructural model. Phenomenological models focus on finding a mathematical form that describes the stress-strain experimental data, without making hypothesis on the physiological meaning of the each parameter. For example, Alexander and Cook [39], first, mechanically tested *in vivo* the skin from the upper back of healthy adult males using a suction cup device and obtained biaxial mechanical data. Second, they described these data by employing a relationship of the form

$$N = \frac{C}{\lambda}\left[\lambda^2 - \frac{1}{\lambda^2 \lambda_p^2}\right] e^{K(I_1 - 3)^2}, \tag{1}$$

where N is the skin tension (stress) in testing direction, λ and λ_p are extension ratios in the test direction and in the perpendicular direction, respectively, and C and K are material constants with the dimension of a tension and dimensionless, respectively.

In another study, Tong and Fung [44] proposed a strain energy function of the form

$$W = \frac{1}{2}(\alpha_1 e_1^2 + \alpha_2 e_2^2 + \alpha_3 e_{12}^2 + 2\alpha_4 e_1 e_2) +$$

$$\frac{1}{2} c e^{(a_1 e_1^2 + a_2 e_2^2 + a_3 e_{12}^2 + 2a_4 e_1 e_2 + \gamma_1 e_1^3 + \gamma_2 e_2^3 + \gamma_4 e_1^2 e_2 + \gamma_5 e_1 e_2^2)}, \tag{2}$$

where α_i, a_i, γ_i and c are constitutive parameters, α_i, c with the dimension of a stress, while a_i, γ_i dimensionless, and e_{ij} are the components of the Green strain tensor. In this study, two stress-strain experimental datasets were collected on rabbit skin in two perpendicular directions, each set was collected with one principal direction of stretch and the perpendicular direction fixed. The authors determined the constitutive parameters by fitting the experimental data at two selected points, one at a low stress level and one at a high stress level.

Following the idea proposed by Tong and Fung to employ an exponential functional to describe the mechanics of skin, Veronda and Westmann [45] developed a strain energy function of the form

$$W = c_1\left[e^{\beta(I_1 - 3)} - 1\right] + c_2(I_2 - 3) + g(I_3), \tag{3}$$

where c_1, c_2, β are constitutive parameters, the first two with the dimension of stresses and the last dimensionless, $I_1 = tr(\mathbf{C})$, $I_2 = \frac{1}{2}[(tr(\mathbf{C}))^2 - tr(\mathbf{C}^2)]$ and $I_3 = det(\mathbf{C})$ are, respectively, the first, second, and third invariant of the right Cauchy-Green strain tensor, $\mathbf{C} = \mathbf{F}^T\mathbf{F}$, where $\mathbf{F}$ is the deformation gradient. Then, the Authors determined the best-fit constitutive parameter values by optimizing the form shown in **Equation (3)** to describe uniaxial stress-stretch data collected on cat skin. Phenomenological models provide accurate description of the experimental data, however, they offer little insight on skin microstructure. In contrast, microstructural models connect macroscopic level mechanical response of skin to its microstructure by associating constitutive parameters to physiologically meaningful measurements.
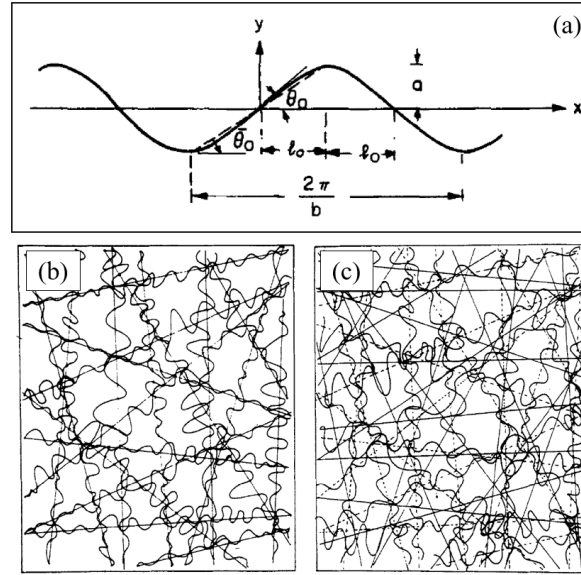
Figure 3. (**a**) Geometry of a model collagen fiber as described in [46]. (**b-c**) Schematics of the collagen and elastin network structure in flat tissue from [42], [43]. (**b**) Tissues with high density of crosslinks and elastin induced collagen undulation. (**c**) Tissues with low density of crosslinks and inherent collagen undulation. Thick lines represent collagen; thin lines represent elastin, and dotted lines represent overall collagen fiber direction.

As one of the early attempts to develop microstructural model, Comninou and Yannas [46] modeled fiber undulation as long sinusoidal beams (**Figure 3 a**). The model however did not include collagen structure experimental data to determine the geometrical parameters of the sinusoidal beams, further the effect of fiber orientation was only briefly discussed in a qualitatively manner. Then, Lanir [42], [43] proposed a modeling framework that described skin structure as a ground matrix in which collagen and elastin fiber embedded (**Figure 3 b-c**). The assumptions made in this framework have crucial influence on later skin microstructural models [47]. The total strain energy function was assumed be to the sum of strain energy functions of each component. The fibers were modeled to have no compressive strength and to be buckled under zero load. Further, each fiber was considered to have the capability of supporting only a uniaxial strain, estimated as the tensorial transformation of the overall strain in the fiber's direction. The undulation and orientation of the fibers were described using probability density functions.

8

In another study, Groves *et al.* [40] developed a microstructural model to compare human and murine skin mechanical characteristics. The model described the skin as a composite structure made of ground matrix and three families of parallel fibers. The ground matrix was described by the Veronda-Westmann material shown in **Equation (3)**. Three fiber families were included in the model, the mechanical behavior of each fiber family was described by employing the strain energy function developed in [48]. In this study by Weiss *et al.*, however, there is a lack of microstructural experimental data, which resulted in the necessity of increasing the number of constitutive parameters, 4 for each collagen family and 14 for the model overall, to ensure a good mechanical description. The redundancy in constitutive parameter offered good fitting results to experimental data, but somewhat diminished the physical meaning of each parameter. A later study from Karimi *et al.* [41] had similar issues, the model employed 4 fiber families, and although the mean orientation angle of the collagen fibers was measured experimentally, it was still not enough to characterize the collagen structure in details in the constitutive model.
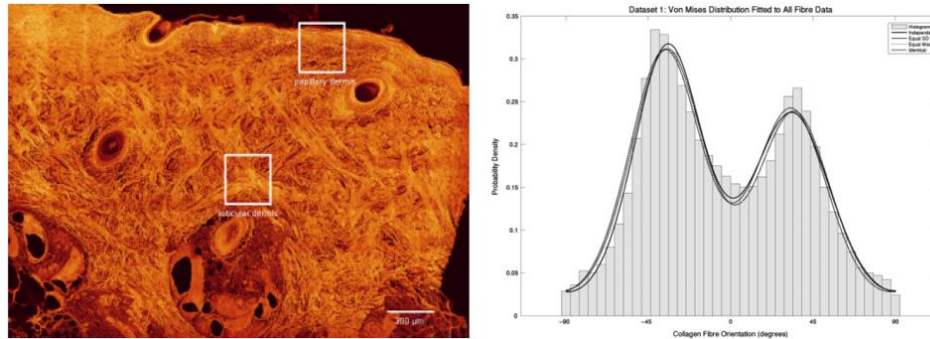
Figure 4. **Left**: Maximum intensity projection for a 60 μm transverse section showing collagen fibers in bright red. **Right**: A mixture of two von Mises distribution fitted to fiber orientations presented in the form of histogram, under various symmetry assumptions. Pictures are from [37].

As discussed in the section *Skin microstructure*, quantifying collagen structure is a key step to develop accurate skin microstructural models that have physiologically meaningful parameters. Jor *et al.* [37] used a structural-tensor approach to determine the collagen spatial distribution of

porcine skin. Orientation data were fitted to a mixture of two von Mises distributions (**Figure 4**). In a later study, Jor *et al.* [49] tested porcine skin *in vitro* using a multi-axial tensile test. With the collagen structural data parameters, a modeling framework was proposed to simulate the experiments. The fibers were assumed to be linearly elastic and the ground matrix was assumed to behave like an isotropic neo-Hookean material. One drawback of these studies is that the collagen fiber microstructure was examined in a plane perpendicular to the skin surface, while the preferred orientation of collagen fibers in the dermis is parallel to skin surface [29].

More recently, Ní Annaidh *et al.* [38] developed an automated image analysis routine (**Figure 5 a-f**) that can calculate the orientation distribution of collagen network using Van Gieson stained histology slides of human back skin. The image analysis routine can distinguish each single collagen fiber in the field and fit an ellipse along the fiber direction. The direction of the major axis of the fitted ellipse represented the orientation of the collagen fiber. The standardized π-periodic Von Mises distribution was used to fit the probability density of collagen fiber orientation distribution (**Figure 5 g**). Finally, the resulting structural parameters were then employed in the Gasser-Ogden-Holzapfel model [50] to fit the uniaxial tensile data. The model was not only capable of fitting the known experimental data, but also able to provide good prediction of stress-stretch response of skin sample along different direction as long as the unique structural data of that sample were provided.
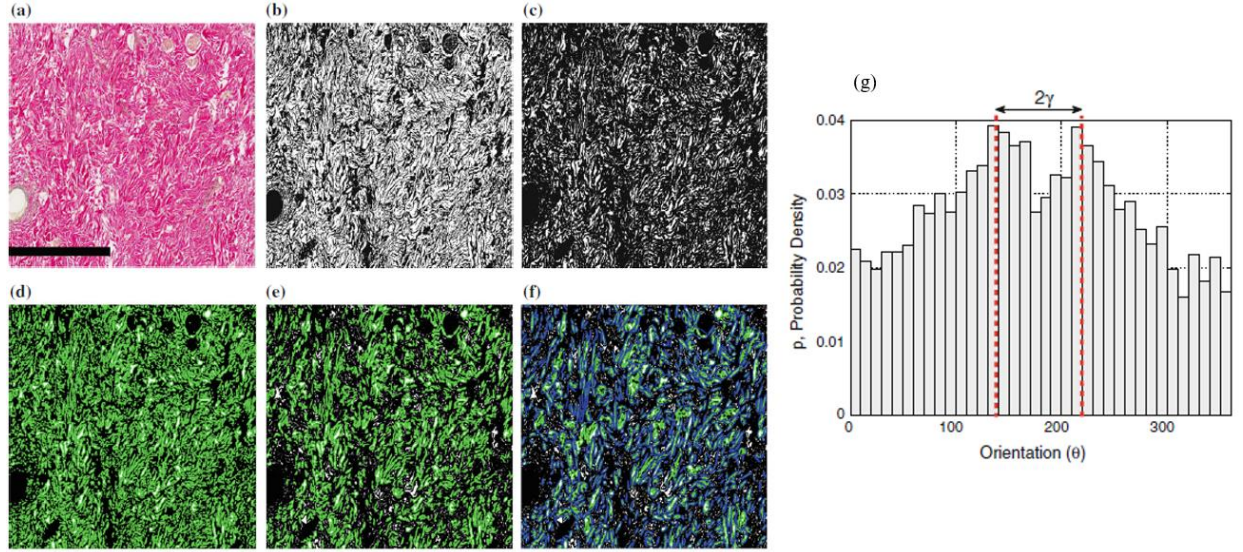
Figure 5. Images output from automated algorithm. (**a**) Original histology slide. Scale bar is 1 mm. (**b**) Binarized image after automated thresholding. (**c**) Binarized image after erosion step. (**d**) All identified collagen bundles outlined in green. (**e**) Remaining bundles which meet area and eccentricity criteria. (**f**) Best fit ellipse about each fiber that meets the specified criteria. (**g**) Histogram of collagen orientations. The two distinct peaks correspond to the preferred orientation of the two fiber families. All images are from [38].

Based on image analysis routine shown in [38], this dissertation will further improve the automated routine's ability recognizing collagen, and reduce the loss of pixel during the process (i.e., binarization step). Collagen undulation level will also be experimentally measured and implemented into the microstructural model.

Preferred collagen fiber orientation. The studies by Jor's group and Ní Annaidh's group showed, through histological data, the existence of a two peak orientation distribution of collagen fibers within the skin dermis. This suggests that, when implementing a microstructurally accurate skin layer into a FE model, we need to determine the preferred collagen fiber orientation across the human body, and specifically within the regions of interest. In this context, we consider the angle associated with the bisector of the two peak distribution as the preferred collagen fiber orientation angle. It has been shown before that the preferred collagen orientation angle is closely related to the skin tension lines [51]. Langer's lines might be the best-known skin tension lines mapping on human body. However, Langer's descriptions have often been misquoted and his

illustrations incorrectly reproduced [52]. This fact can be shown by simply searching "Langer's lines" on a search engine like Google when a variety of line mappings on human body return as results, some of them showing drastic differences between one another. Indeed, it is of great importance to determine the proper mapping of tension lines for the implementation of collagen fibers in the skin layer FE model.

In 1834, Guillaume Dupuytren [53], [54] for the first time made the observation that elliptical wounds were produced by a round instrument on human body. Inspired by Dupuytren's observation, in 1861, Langer [55] used rounded shaped instruments to stab through skin of cadavers, providing a thorough mapping of the long axis direction of the elliptical shaped wounds (**Figure 6 a – c**). This mapping became of great importance in the context of surgical procedure, because surgeons were seeking to identify techniques that resulted in optimal healing and least conspicuous appearance of the surgical incision. It became apparent that the proper direction of the incision is the one that allows the collagen formed under the scar to be aligned along the same direction with collagen of neighboring tissues, and that the mapping provided by Langer seemed to be related to this information. In 1935, however, Webster [56] first suggested surgeons should place incisions in natural wrinkle lines, rather than Langer's lines. In 1940's, Kraissl also noted that lines used by surgeons for elective surgical incisions did not correspondent to Langer's lines. In 1951, Kraissl [57] further provided a complete mapping of wrinkle lines of the whole body (**Figure 6 d - f**). Wrinkle lines can be demonstrated by existent wrinkles, gentle compression of the relaxed skin, muscles contraction or a combination of these methods. Later on, Borges and Alexander [58], [59] described the relaxed skin tension lines (RSTLs), which can be obtained through pinching test. The difference between RSTLs and wrinkle lines are subtle and reconcilable,

while Langer's lines differ considerably from both [56]. Nonetheless, RSTLs and wrinkle lines are often shown and erroneously claimed to be Langer's line [53].
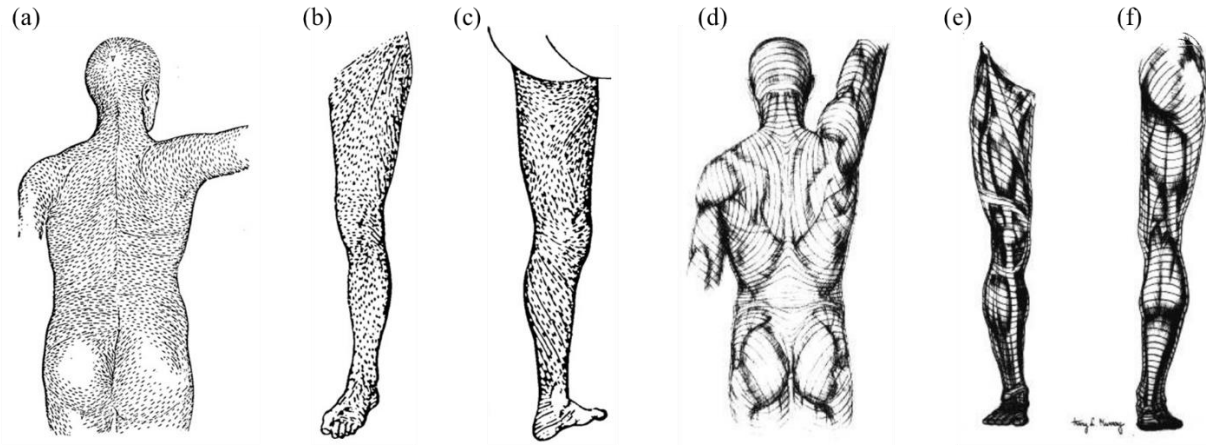
Figure 6. Langer's lines and wrinkle lines on selected body parts. (**a**) Langer's lines on the posterior trunk and scalp. (**b**) Langer's lines on the anterior leg. (**c**) Langer's lines on the posterior leg. (**d**) Wrinkle lines on the posterior trunk and scalp. (**e**) Wrinkle lines on the anterior leg. (**f**) Wrinkle lines on the posterior leg.

When it comes to the question that which tension line mapping should be used for collagen fiber implementation in skin for a FE model, we argue that wrinkle lines are the most appropriate for the model that is proposed in this dissertation. Wrinkle lines and RSTLs have been estimated on the skin of a living person, while Langer's lines were obtained through study on skin cadavers. For this reason, wrinkle lines and RSTLs can take into account the action of muscle and movement of joints, which play an important role in causing skin tension lines. The static state of the cadaver and the relaxed state of underlying tissues after death might significantly change the tension line distribution compared to a living person. Furthermore, by using x-ray diffraction and micoradiographic technique, Homstrand [51] demonstrated that the major part of the collagen is parallel with the wrinkle lines. The surgeons' observation of wound healing from surgical incisions also endorsed wrinkle lines rather than Langer's lines to be the proper tension lines determining the preferred collagen fiber directions. Therefore, the preferred fiber orientation within the FE model skin layer will be determined by wrinkle lines in this dissertation.

1.3.   FE models of leg and buttock area

Previous FE studies have investigated the influence of both internal and external factors that affects stresses/strains distribution in thigh-buttock area during sitting. Dabnichki *et al.* [60] showed that, when sitting on a rigid surface, if friction occurs at the body/seat interface the stresses in the tissue adjacent to the seat increased, but at the same time the maximum stress, which occurred some distance away from the contact area, decreased. As regard to cushion, it has been concluded by previous studies that a softer cushion not only reduces the interface stress substantially [16], but also contributes to decreasing internal stresses [61]. Furthermore, it has been shown that a thicker cushions can effectively reduce seat-interface and subcutaneous compressive stress [27]. Regan et al indicated, however, the existence of an optimal cushion thickness, the showed that increasing cushion thickness over a certain level could compromise postural stability, leading to asymmetrical loading, elevated seat-interface pressures, and loss of function [27]. Not only the mechanical properties of the seating surface, but also the mechanical characteristic of soft tissues play an important role in the magnitude and subdermal stresses/strains distribution. By employing uniaxial tension testing and FE model on rat gracilis muscles, Linder-Ganz and Gefen concluded that injured muscles were significantly stiffer than uninjured ones as a result of exposure to prolonged and intensive loads [15]. This increased muscle stiffness in widening region could lead to elevated tissue stresses that exacerbate the potential for tissue necrosis.

Nonlinear mechanical behavior data in vivo and parameters estimation. Despite all the findings about contributing factors to PUs formation from previous FE studies, one critical aspect that is still missing is the address of nonlinear mechanical behavior of FE models. There are two aspects involved to validate the nonlinear mechanical behavior of the FE model: (1) *in vivo* experimental data exhibiting the full range (from being relaxed to being fully compressed) nonlinear mechanical behavior need to be collected. (2) A parameter estimation process that

actively reduces the difference between the experimental data and corresponding FE output is needed to achieve the accurate constitutive parameters for the FE model. However, both of the two aspects were largely overlooked in the literature. To further illustrate this issue, the model development and validation process of some state-of-the-art FE studies focusing on leg and buttock area are discussed as below.
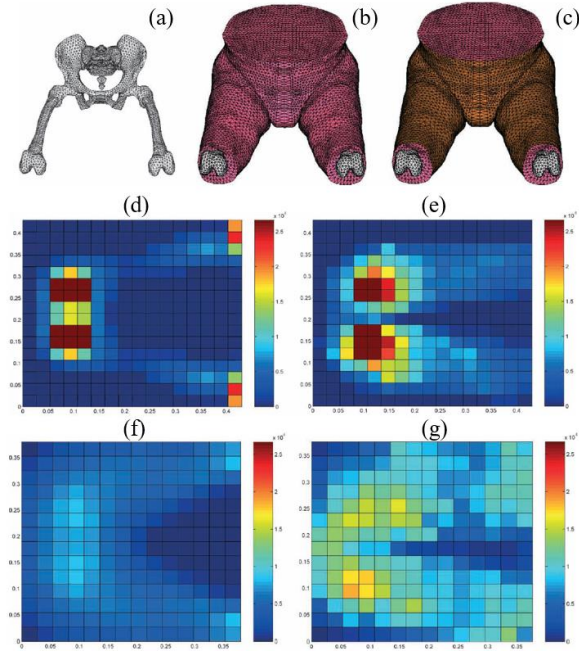
Figure 7. FE model of the pelvis and thighs published in [21]. (**a**) Bony structures, (**b**) bony structures and human soft tissues, and (**c**) complete model (i.e., bony structures, human tissues, and skin). (**d-e**) Pressure distributions (Pa) predicted by the FE pelvis model (shown in **d**) and measure experimentally for a human male (shown in **e**) for a rigid surface boundary condition. (**f-g**) Pressure distributions (Pa) predicted by the FE pelvis model (shown in **f**) and measure experimentally for a human male (shown in **g**) for a soft cushion boundary condition. All results previously published in [21].

Verver et al [21] developed a 3D buttock-thigh sitting model (**Figure 7 a-c**) to investigate the interface pressure distribution during sitting and how variations in human tissue and cushion properties would affect these distributions. The buttock-thigh outer geometry and bone geometry were collected from two different subjects. The skin was modeled using triangular shells elements, while fat and muscle were modeled together as a whole using 4 node tetrahedron elements. The skin was described employing a linear elastic isotropic constitutive model, and bulk properties of

fat and muscle were described using the Mooney-Rivlin constitutive model. Finally, all the constitutive parameters were chosen from previously published work. This model was validated by comparing interfacial pressure fields predicted by the FE model and measured experimentally, associated with siting on a rigid surface (**Figure 7 d-e**) and on a soft cushion (**Figure 7 f-g**). The Authors concluded that FE model showed reasonable correlation with the human data, pressure distribution differences between FE model and *in vivo* data were not quantified, and the Authors did not define the term "reasonable correlation" in a quantifiable manner. Finally, there was no optimization process implemented in the study to attempt to minimize the difference between FE model and *in vivo* data.
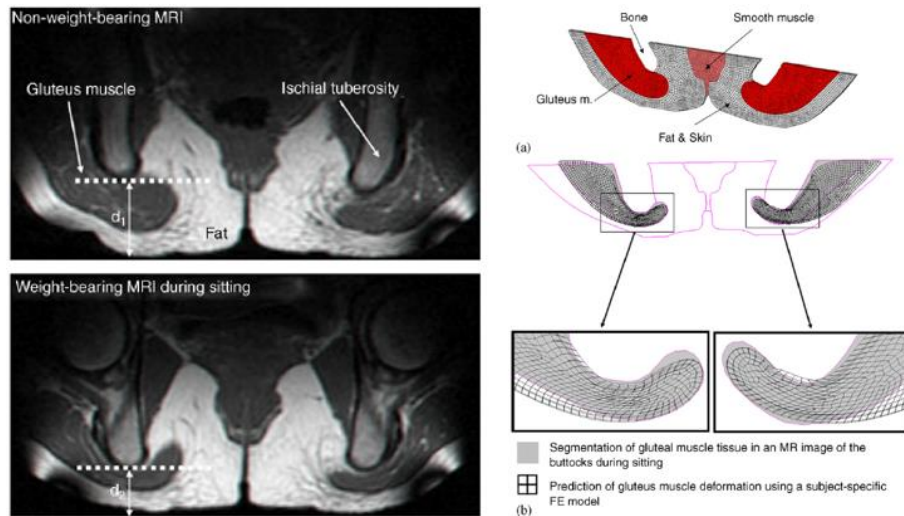
Figure 8. **Left**: Examples of coronal MRI images of the buttock from a healthy 29-year-old female at a non-weight-bearing posture (top frame) and during weight-bearing sitting (bottom frame). **Right**: (**a**) Mesh of the subject-specific FE model (for subject #4). (**b**) An example of the fit between MRI measured (gray areas) and FE-calculated (meshed areas) gluteal muscle contours during weight-bearing sitting. The right and left frames show data for the gluteus muscles at the right and left body sides, respectively. Pictures are from [19].

In another study, Linder-Ganz *et al.* [19] developed subject-specific semi-3D model, defined has having one dimension significantly smaller when compared to the others (i.e., the model has a thickness of 4 mm) for 6 subjects. The model geometry was constructed based on MRI images obtained from a single plane. Muscle and fat were modeled separately and skin was modeled as

part of the fat layer (**Figure 8**). The FE models were then validated using two indicators: (1) the contour of the gluteal muscle from the FE solution was compared to that measured from MRI images, and (2) the peak interface pressure under the ischial tuberosity predicted by the FE analysis was compared to that measured experimentally, for each subject. This study used quantifiable indicators (i.e., correlation coefficient R^2 and p-values of two-tailed probability) to describe the output difference between FE model and *in vivo* data. However, there was still no optimization process to minimize the error between FE model and *in vivo* data. This model was then employed in a later study to investigate the strains and stresses differences in buttock subdermal tissue between paraplegic participants and healthy participants [62].
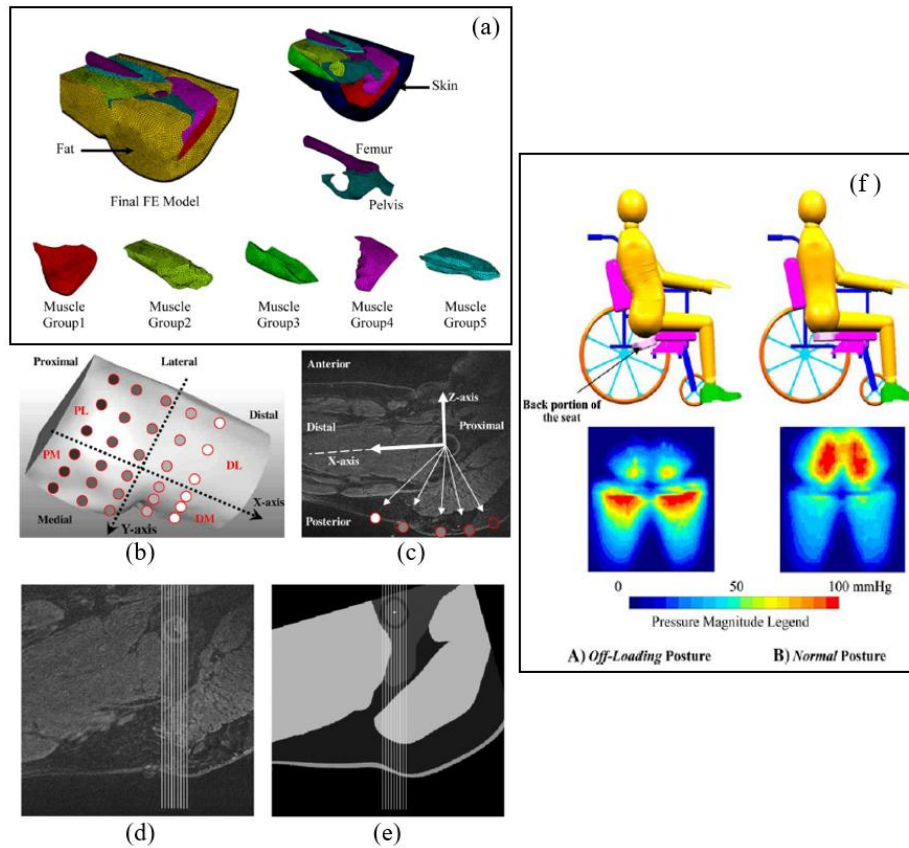
Figure 9. (**a**) 3D thigh-buttock FE model and the included muscle groups and bony structure. (**b-c**) Representation of the 30 regions of interest that were identified on the thigh-buttock surface and definition of the local reference system. (**d-e**) Sagittal view of the small area right beneath the ischial tuberosity that was selected to calculate the deformation shift of the gluteus muscle. (**d-e**) Representation of the selected area in the MRI and corresponding FE simulation, respectively. All figures are from [20]. (**f**) Results are from [63].

A work published by Makhsous *et al.* [20] focused on the development of a 3D thigh-buttock FE model with detailed muscle geometry. 5 muscle groups were identified in the model, which also contained separate fat and skin layer. In this study, fat and muscle layers were meshed using 4 nodes tetrahedral elements, while skin was meshed using 3 nodes triangular elements. All the soft tissues mechanical behaviors were described employing Mooney-Rivlin constitutive models, and the constitutive parameters were obtained for each component from literature. The FE model was validated comparing the values of two quantities, specifically the gross displacement of 30 regions of interest (**Figure 9 b-c**) and shift of gluteus muscle (**Figure 9 d-e**), between FE and *in vivo* data during the compression introduced by an inflated bladder. This is the first study that developed a FE model that could accurately represent the soft tissues anatomical structure. The model developed here was then employed in a later study to evaluate the effectiveness of a new sitting concept, "off-loading posture", which lowered the sitting surface of the buttock area, to partly transfer the loads from the ischial tuberosities to thigh soft tissues [63] (**Figure 9 f**).
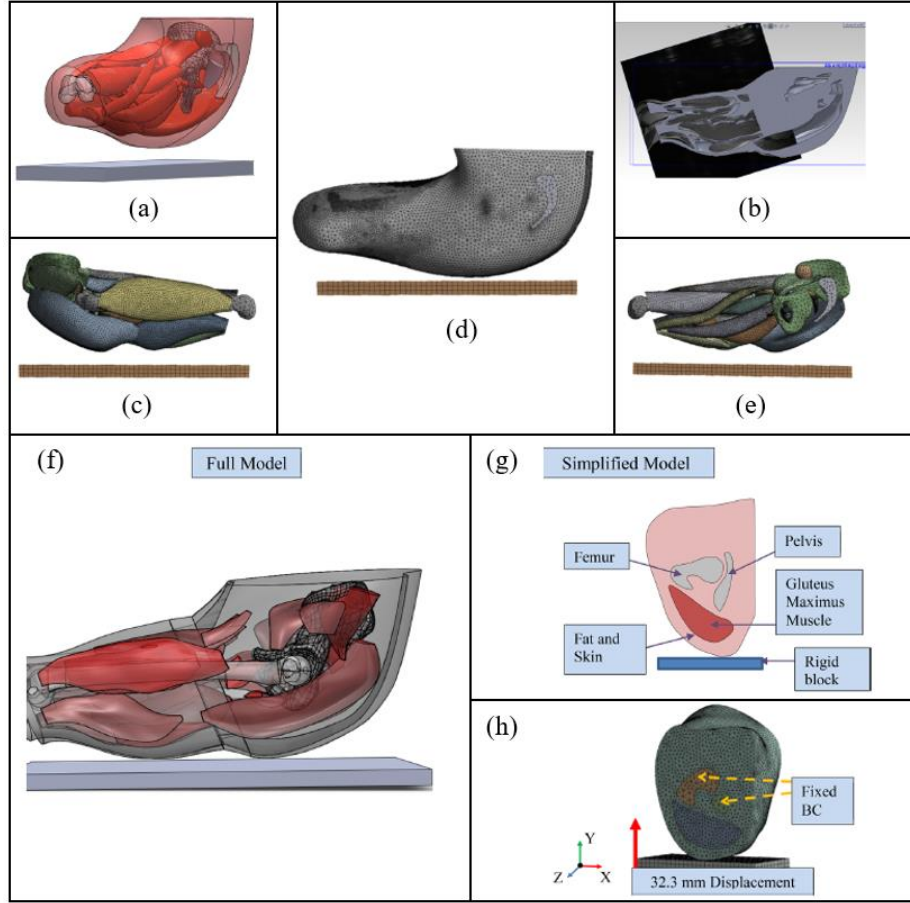
Figure 10. (**a-e**) Three-dimensional CAD model of the left buttock and thigh. The model was created from MRI scan segmentation. This included: manual tracing over contours of muscles, fat and bones in transverse MRI scans using, and then creating a lofted geometry that connects the segmentation contours. (**a**) An isometric view of the 3D subject-specific CAD model. (**b**) A side view of the 3D subject-specific CAD model overlaid on to the sagittal non-weight-bearing MRI scan of the upper thigh. (**c**) The right view of the meshed muscles and bones, (**d**) the left view of the mesh for the fat layer and the sacrum, and (**e**) the left view of the meshed muscles and bones. (**f-h**) An illustration of the detailed FE model (**f**) and the simplified FE model (**h**). (**g**) The anatomical structures included in the segmentation of the simplified model. (**h**) The boundary and loading conditions applied to the simplified model. All figures are from [28].

In a recent study, Al-Dirini *et al.* [28] developed a subject-specific model through MRI images (**Figure 10 a-e**). The model geometry composed of very detailed muscle structure, which contained 28 muscles, and inter-muscular fat, fascia, and subcutaneous fat were modeled together. Tetrahedron elements were used to mesh the geometry, and first order Ogden model was employed to describe the material behavior. In this study, for the first time, a parameter optimization process was employed. Briefly, a simplified model containing only the tissues surrounding the ischial

tuberosity and the lesser trochanter was isolated from the full 3D model (**Figure 10 f-h**). Initial Ogden parameters were obtained through literature. Then Genetic Algorithm was used to search for proper constitutive parameters by minimizing the difference between FE estimates and MRI measurements on 1-D thickness change of the Gluteus Maximus, intermuscular fat, subcutaneous fat below ischial tuberosity and the lesser trochanter. The FE model with optimized constitutive parameters was further validated by comparing the FE calculation and MRI measurements for the displacement of gluteus maximus muscle. This study for the first time utilized an optimization process to estimate constitutive parameters, however the *in vivo* data used for the comparison only included two loading conditions, weight-bearing and non-weight bearing conditions. Due to the nonlinear nature of soft tissue, data collected in only two loading conditions might not be enough to characterize the nonlinear mechanical behavior of soft tissue. As discussed above, there is still a need for experimental data collected *in vivo* that can represent mechanical behavior of soft tissues in large deformation, and for an optimization procedure that can estimate best-fit constitutive parameters in a 3-dimensional FE model.

2D, semi-3D, and 3D FE model. Geometry of the early FE models were largely simplified: the buttocks were modeled as a hemisphere [64] or a slab [27], and the ischial tuberosity were modeled as a cylinder with hemispherical end-point [60], as shown in **Figure 11 a-c**. The FE models in these studies were usually further simplified to 2D models by assuming axisymmetry, while other studies developed 2D models from the start by assuming plane strain or plane stress conditions [60], [61], [65], as shown in **Figure 11 d-e**. More recently, researchers were able to develop anatomically accurate 3D models for the thigh and buttock areas by employing medical images [20], [28], [66]. Despite increasing computational capabilities, 2D and semi-3D FE models still remain popular among researchers [19], [67], [68]. The model from Linder-Ganz *et al.* [19]

20

(**Figure 8**) is a typical semi-3D model: it has three dimensions, but the measurement in one dimension (4 mm in thickness) is significantly smaller than the other two. All elements had direct contact to the plane strain boundary condition. Therefore, semi-3D FE model would behave more like 2D model than 3D model. Considering its nearly incompressible nature, soft biological tissue will significantly expand/shrink in the transverse directions when subjected to the large deformations associated with seating. It has been shown by recent studies that soft tissues in the leg-buttock area are subject to three-dimensional deformations. Al-Dirini *et al.* [69] measured deformations below the ischium and the proximal femur across 6 seated subjects through MRI scans on both transverse and sagittal planes. Their results showed that deformation of gluteus maximus muscle in the direction along the thigh was almost equivalent to the deformation below the ischium perpendicular to the sitting surface. In a typical semi-3D model (**Figure 8**), deformation of gluteus muscle in the direction along the thigh is lost. Sonenblum *et al.* [70] conducted multi-planar scans on the buttocks of 7 subjects. Their results also show that a single slice of MRI hinders the ability to identify tissue accurately. Therefore, 2D and semi-3D FE models are limited in their ability to accurately represent the *in vivo* mechanical behavior of the soft, due to the influence of boundary conditions.

Figure 11. (**a**) The buttock model geometry from [64]. (**b**) Cross-section of the FE model of seat-interface and buttock soft tissue from [27]. (**c**) The finite element model of buttock and seat surface from [60]. (**d-e**) Finite element model [61] during sitting position: (**d**) before loading. (**e**) after loading on stiff target. Plane stress was assumed on the boundary plane on this 2D model.

Constitutive model choice. Early FE studies commonly employed linear elastic material description for soft tissue. For example, Chow & Odell [64] used Young's modulus that was measured from synthetic gel from literature for their buttock model. Todd & Thacker [71] obtained Young's modulus from experimental data by considering only the initial linear proportion of the force-deflection curve. Ragan et al [27] employed the same Young's modulus as Todd & Thacker in their study. With the growing computation power and FE platform advancement, the constitutive models applied in the FE models have shifted to nonlinear hyperelastic material. Four hyperelastic models can commonly be found in literature, namely neo-Hookean model [19], [61], [66], [68], Mooney-Rivlin model [20], [21], [60], first order Ogden model [16], [28], [65], and Fung-type model [72], [73]. However, a constitutive model being nonlinear does not guarantee that it is able to match the nonlinear behavior of certain soft tissues. Different nonlinear models have been developed to describe specific soft tissues, but might not be suited to describe others. Due to the lack of *in vivo* data in large deformations and protocols to estimate constitutive parameters,

22

currently no guidelines exist for the choice of constitutive model when it comes to soft tissue. Researcher have acknowledged the need for proper nonlinear constitutive models, for example Moes & Horváth [66] pointed out that a constitutive model with increasing stiffness was required to describe the behavior of soft tissues. Also, Makhsous *et al.* [20] suggested that the primary factor causing the difference between their model prediction and the measurement on MRI images is the lack of an optimal constitutive model and precise material properties in the FE analysis. The apparent nonlinearity of human soft tissue cannot be precisely described by the Mooney-Rivlin model they used in that study. Taken together, there is a pressing need for proper constitutive model choice in human soft tissue modeling.

1.4. Objectives of this dissertation

Taken together all the remaining issues and challenges in the literature, we determine the objectives of this dissertation to be as follows:

(1) Propose a microstructurally based skin constitutive model. Quantify collagen network structure and incorporate it into the structural model.

(2) Develop an optimization procedure that is able to match nonlinear behaviors between FE simulation and *in vivo* experimental data. Quantify the different between 3D and semi-3D FE model in an individual-specific case. Compare the accuracy of four commonly used constitutive model representing soft tissue nonlinear mechanical behavior.

(3) Construct a thigh FE model that has detailed anatomical representation of different soft tissue types, i.e., skin, fat, and muscle. Identify constitutive parameters for the different soft tissue types that can describe the *in vivo* experimental data accurately.

2. **CHARACTERIZATION OF THE MECHANICAL PROPERTIES OF SKIN USING RAT AND A MICROSTRUCTRUALLY BASED CONSTITUVIE MODEL**

2.1. Overview

The goal of this chapter is to develop a microstructural constitutive model that links collagen microstructure and skin macroscopic level mechanical behavior. Some important aspects of mechanical properties of skin were investigated, and a microstructural model of skin was developed in this chapter. First, storage condition effects on skin mechanical properties were studies. We developed three different storage protocols. The mechanical parameters of skin samples stored in those conditions were evaluated and compared to those of the fresh samples. The best storage protocol among the three was determined. Effects of orientation, location, and sex on skin mechanical properties were also investigated. Automated image analysis routine were developed to quantify collagen structure, i.e., fibers orientation distribution and collagen relative content, using histology images. Those quantified collagen structure data were then implemented into the microstructural constitutive model.

2.2. Methods

2.2.1. Mechanical testing

Sample collection. Skin samples from sixteen Sprague Dawley rats (eight males and eight females, 10 to 12 weeks old) were collected for mechanical tensile tests. The dorsal skin of each animal was shaved after sacrifice and the entire back skin flap was excised. A custom-made dog bone shaped die was used to punch samples out of the flap (see **Figure 12 b-c** for sample dimensions). Four samples were collected from each animal, two from the upper back, on each side of the spine (i.e., upper left and upper right locations), and two from the lower back, on each side of the spine (i.e., lower left and lower right locations). The sixteen animals used for

mechanical tensile tests were divided into two groups of eight animals (four males and four females) each: in Group I, samples were cut in the axial direction (i.e., direction parallel to the spine); in Group II, samples were cut in the transverse direction (i.e., direction perpendicular to the spine, see **Figure 12 a**). Finally, the thickness of each sample was measured employing a Fowler digital Vernier caliper. Samples from male rats have thickness of $1.66\ mm \pm 0.34\ mm$ and samples from female rats have thickness of $1.24\ mm \pm 0.25\ mm$.
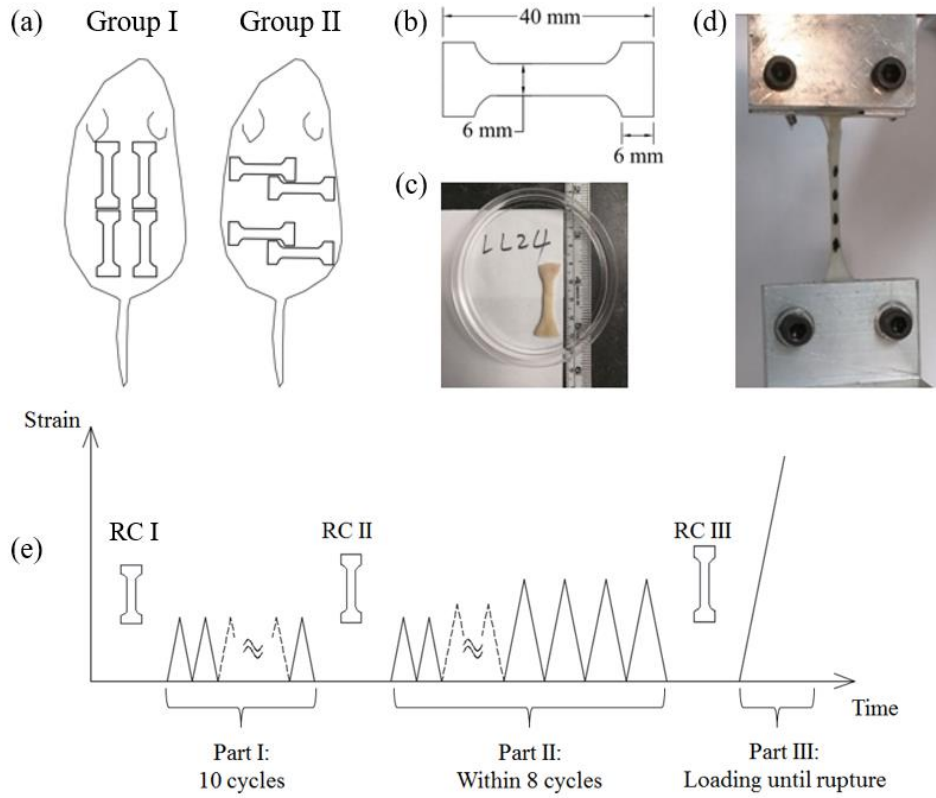
Figure 12. (**a**) Sample location and orientation on animals in Group I (left in the picture) and Group II (right in the picture). (**b**) Dimensions of dog bone shape skin sample. (**c**) A skin sample placed in Hank's Balanced Salt Solution (HBSS) after it was cut out of the skin flap. (**d**) A mounted skin sample during the tensile test. The position of the four markers placed on the central part of the sample were tracked by a CCD camera to calculate its stretch ratio during the test. The gauge length (i.e., the distance between the highest and lowest fiducial marker on the skin sample) was $16.2\ mm \pm 1.5\ mm$, as measured before the test. (**e**) Loading scheme of the uniaxial tensile test. RC: reference configuration.

Storage condition. To investigate the influence of storage condition on skin mechanical properties, three different storage protocols were developed as follows, Protocol I: samples were

stored at 4°C in Hank's Balance Salted Solution (HBSS) for 24 hours before testing. Protocol II: samples were flash frozen in isopentane that was cooled down by dry ice (-78.5°C). The flash frozen samples were then stored in a -80°C chamber for up to two weeks, and thawed at 4°C for 6 hours before testing. Protocol III: flash-freezing and storage temperature were the same as Protocol II, but samples were thawed at 4°C for 24 hours before testing. Control: samples were tested fresh, within 2 hours of excision. Skin samples obtained from each animal in Group I were randomized into the four groups (three storage protocols plus control), while skin samples obtained from animals in Group II were stored using Protocol II.

After the mechanical testing, an analysis of variance (ANOVA) was carried out to examine the influence of storage condition on skin mechanical parameters. While the averaged stress-stretch behavior difference between the control group and each storage protocol was evaluated using normalized root-mean-square deviation (NRMSD), which was calculated as

$$NRMSD = \frac{\sqrt{\frac{\sum_{j=1}^{n}(\lambda^{prtcl}-\lambda^{cntrl})_j^2}{n}}}{\max_{1\leq j\leq n}(\lambda^{cntrl})_j}, \tag{4}$$

where λ^{prtcl} and λ^{cntrl} represented stretch ratios of a sample from a storage protocol and a control sample, respectively, at 20 (i.e., $n = 20$) different evenly spaced stress values along the stress-stretch curve.

Tensile test. Quasi-static uniaxial tensile tests were performed at a speed 20 mm/min on skin samples. Sandpaper was used to increase the grip between the clamp and skin samples. Four markers were placed on the central part of the skin sample (**Figure 12 d**) to track the variation in length using a CCD camera (Hitachi model KP-M2AN). A load cell (Futek model LSB200) was used to record forces applied to the samples during the tensile test. Before each part of the test, a preload of 10g (~ 0.1N) was applied to the sample and dimensions of the sample in different

reference configurations were recorded. The tensile test protocol consisted of three parts (**Figure 12 e**): (1) 10 loading-unloading preconditioning cycles at 20% strain; (2) a step-increase loading protocol, starting with two loading-unloading cycles at 20% strain; followed by a series of increasing strain levels (5% ~ 8% increase) each performed for two loading-unloading cycles. The highest level of strain for each sample was repeated for an additional two loading-unloading cycles. The 5% ~ 8% strain range was estimated to accommodate the inter-specimen variation, so that similar peak stresses could be achieved for the last cycle. Peak stresses were determined during the test by live readings of the loads and dimensions of the cross-section measured. (3) Rupture loading. Skin mechanical behavior has been previously estimated in a multitude of conditions, e.g., through cyclic loading-unloading test [74]–[76], through rupture test [77]–[79], and through *in vivo* test [80]–[82]. In order to cover the mechanical response of skin under quasi-static loading comprehensively, we chose to investigate both preconditioned hyperelastic behavior and rupture behavior in this study. Part I of the loading protocol was to precondition the lower stress range of the skin mechanical response. Part II of the loading protocol was to obtain preconditioned hyperelastic mechanical behavior of skin that within the similar stress range (0 - 1.5 MPa). Due to the fact that the uniaxial machine was strain-controlled, slight adjustment had to be made in strain increments for different samples to achieve the similar stress range for the last cycle in Part II. By the data from Part II, we were able to model the hyperelastic behavior of a sample and evaluate the corresponding constitutive parameters. Part III of the loading protocol enabled us to characterized skin stress-stretch behavior to its full capacity (i.e., until rupture) and evaluate the mechanical parameters associated with it.

Due to the assumption of incompressibility, $A_0 L_0 = AL$, where L_0 and L are the sample length in the reference and current configuration, respectively; A_0 and A are the sample cross-sectional

area in the reference and current configuration, respectively. True stress σ (i.e., Cauchy stress) is

calculated as $\sigma = \frac{F}{A} = \frac{F}{A_0}\lambda$, where F is the force value in the current configuration measured by

the load cell, and the stretch in the current configuration is measured by $\lambda = \frac{L}{L_0}$. The stress-stretch

curve of each skin sample during the loading of the last cycle in Part II of the tensile test (**Figure**

12 e) was used for constitutive modeling purposes due to its well preconditioned behavior, while

the stress-stretch curve during the rupture loading was used to evaluate the mechanical parameters

of skin samples as described in the following section *Mechanical parameter and statistical test*.

  Mechanical parameters and statistical test. We evaluated five mechanical parameters of skin

[83], defined as follows and as shown in **Figure 13**. **Initial slope**, represented the stiffness of the

rupture stress-stretch curve at the first 2% deformation strain. We hypothesized that this response

was dominated by the ground matrix content and exhibits approximately linear behavior.

Maximum slope, described the stiffness of the quasi-linear part of the rupture stress-stretch curve

at high stress levels, which we hypothesized was dominated by the mechanical behavior of

collagen. **Rupture stretch** and **Ultimate tensile strength (UTS)**, represented the stretch and stress

value at point of rupture, respectively. **Toughness**, represented the work input done per unit

volume of a sample during rupture loading, defined as the area under the rupture stress-stretch

loading curve. Upon completion of tensile tests, the mechanical parameters of each sample, as

described above, were evaluated. Three-way ANOVA was utilized to determine the influence of

location, orientation, and sex on skin mechanical parameters. Significant level of statistical tests

was set to be $p = 0.05$.
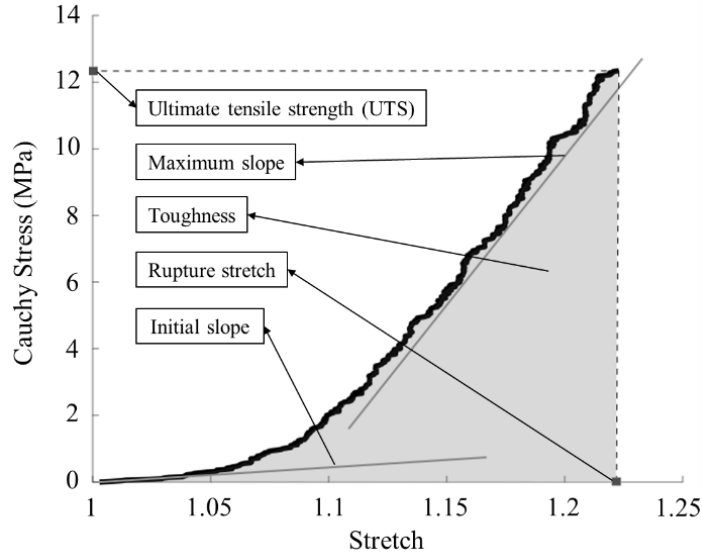
Figure 13. Mechanical parameters on a representative rupture stress-stretch curve of a rat skin sample.

2.2.2. Histology and collagen network analysis

Dog bone shape skin samples along the spine were obtained from another five male Sprague Dawley rats (10 to 12 weeks old) at the same four locations where samples for mechanical tensile testing were collected (i.e., upper left, upper right, lower left, and lower right). Biopsies were excised parallel to the skin plane at the middle of the dermis layer. Two biopsies from each sample were stained using picrosirius red (PSR) and Masson's trichrome, respectively. Stained biopsies were examined using a Nikon microscope Eclipse 80i at a $10 \times$ magnification. Nikon Digital Camera DXM 1200c was used to take digital images of the examined field.

Measurement of relative collagen content. Relative collagen content was measured through its percentage area of Masson's trichrome stained histology slide [84], [85]. Images of total field area of $52\ mm^2$ were taken for each sample. It has been shown that collagen area percentage measured through Masson's trichrome stained biopsies are highly correlated with collagen dry weight measured by a hydroxyproline assay [86]. A color-based segmentation algorithm from the MATLAB image processing toolbox was used to separate different colors from the images, i.e.,

29

black (nuclei), red (cytoplasm, muscle, erythrocyte), and blue (collagen), as shown in **Figure 14 a-d**. Different to other algorithms which require thresholds to define colors [87], the LAB color space based algorithm allows the investigator to choose reference colors from the image and then categorize each pixel of the image into the closest reference color. This approach provided good agreement with visual observations. Relative collagen content was calculated as the ratio between pixels identified as collagen and the total pixels identified as non-background. Finally, the relative collagen content of each back location was obtained by averaging measurements over $n = 5$ animals.

Automated detection of collagen fiber bundle orientation. PSR stained biopsies were examined under polarized light. Images of total field area $26 \, mm^2$ were taken for each sample. Due to the birefringent nature of collagen fiber bundles, which was further enhanced by the PSR stain, thick, medium, and thin collagen fiber bundles exhibited red, yellow, and green colors under polarized light, respectively [87], [88]. Using the LAB color space based segmentation algorithm described above, we separated each PSR stained histology image into three images (**Figure 14 e-h**) that each contained only thick fibers (red), medium fibers (yellow), and thin fibers (green). After collagen fiber bundles were grouped based on thickness, a previously validated algorithm [38] was used to detect fibers orientation. Briefly, first, each color-segmented image was binarized by turning pixels representing collagen fiber bundles into white pixels and pixels representing background into black pixels. Second, an erosion process was performed to detach cross-linked bundle from each other, and then a hole-filling process was performed to make each individual fiber bundle a solid recognizable piece. Then, each fiber bundle was fitted with an ellipse that satisfied the eccentricity and minimum size criterion, to exclude out-of-plane fibers from the analysis. An average of 16,372 collagen fiber bundles per sample were detected. The orientation

of the major axis of each ellipse (positive in counter-clockwise direction) with respect to the rat dorsal midline (i.e., spine direction) was calculated. Finally, the total fiber orientation of each sample from the same location were averaged over $n = 5$ animals and the probability density of collagen fiber bundle orientations were plotted for each location.

Manual examination of collagen straightness. Collagen fiber bundles are undulated when skin is in a stress-free state [42]. Collagen undulation was measured by introducing a straightness parameter, defined as $G_q = \frac{l_q}{L_q}$, where l_q represented the distance between two ends of each fiber, and L_q represented the total length of each fiber (**Figure 14 i** & **j**) [89], [90]. 200 collagen fiber bundles in total (50 collagen fiber bundles per location) were measured across all 20 samples for straightness.
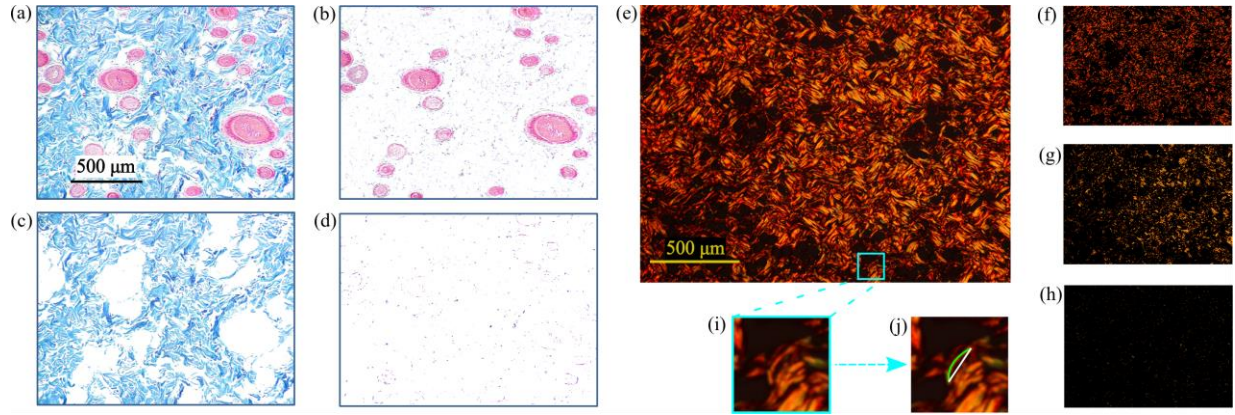
Figure 14. Masson's trichrome stained rat back skin histology slide, as shown in (**a**), were segmented into images with different components based on colors, i.e., (**b**) red (cytoplasm, muscle, erythrocyte), (**c**) blue (collagen), (**d**) black (nuclei). Collagen fiber bundles in a PSR stained rat back skin histology slide observed under polarized light, as shown in (**e**), were grouped based on colors, i.e., (**f**) red, (**g**) yellow, and (**h**) green, which indicated thick, medium, and thin fibers, respectively. Straightness of a single collagen fiber, as shown in (**i**), was measured in the following way as shown in (**j**). The green curve following the shape of the fiber bundle represented the original length L_q, while the white straight line connecting the two ends of the fiber bundle represented the compressed length l_q. Straightness G_q was calculated as $G_q = \frac{l_q}{L_q}$.

2.2.3. Constitutive model

We described the nonlinear, anisotropic behavior of skin employing a mass-averaged strain energy function (SEF) of the form

$$W = \phi^{gm}W^{gm}(\mathbf{F}^{gm}) + \sum_{k=1}^{n}\phi^{(k)}W^{(k)}(\lambda^{(k)}), \tag{5}$$

where ϕ^{α} and W^{α} represented the mass fraction and the SEF for each constituent, respectively, with $\alpha = gm$ for the ground matrix (elastin, glycosaminoglycan (GAG), proteoglycans and glycoproteins), $\alpha = k$ and the kth collagen fiber family ($k = 1, 2, \ldots n$). A collagen family was defined as a collection of collagen fiber bundles oriented within a specified range, defined as $(180/n)°$, with respect to the dorsal midline. The mass fraction of a collagen family was defined as $\phi^{(k)} = \sum_{k=1}^{n}\phi^{(k)}\left(\frac{x^{(k)}}{x^{total}}\right)$, where $x^{(k)}$ represented the number of collagen fiber bundles in the kth collagen family, and x^{total} represented the total number of collagen fiber bundles. The total collagen mass fraction $\sum_{k=1}^{n}\phi^{(k)}$ of a sample was determined by location-averaged values measured from Masson's trichrome stained histology slides. The total mass fraction for the ground matrix of a sample was calculated as $\phi^{gm} = 1 - \sum_{k=1}^{n}\phi^{(k)}$. The relative collagen content measured by area percentage in histology images should be converted to mass fraction by a coefficient. However, the collagen area percentage in our study actually fell in the 60% - 80% range of collagen dry weight [33]. Therefore, the relative collagen content measured by percentage area was implemented directly into the constitutive model for the mass fraction parameter ϕ^{α}. Additionally, the skin was assumed to be an incompressible material, and plain strain conditions were assumed during uniaxial tensile test.

The mechanical behavior of the ground matrix has been described by using a neo-Hookean constitutive model [50],

$$W^{gm}(\mathbf{F}^{gm}) = \frac{c^{gm}}{2}(tr\mathbf{C}^{gm} - 3), \qquad\qquad (6)$$

where c^{gm} was a constitutive parameter with the dimension of a stress and $\mathbf{C}^{gm}$ represented the right Cauchy-Green deformation tensor for the ground matrix, defined as $\mathbf{C}^{gm} = (\mathbf{F}^{gm})^T\mathbf{F}^{gm}$, where $\mathbf{F}^{gm}$ represented the deformation gradient for the ground matrix.

The mechanical behavior of the collagen fiber network has been described by using a Fung-type exponential SEF [91],

$$W^{(k)}(\lambda^{(k)}) = \begin{cases} \frac{c_1^{(k)}}{4c_2^{(k)}}\left\{e^{c_2^{(k)}\left((\lambda^{(k)})^2 - 1\right)^2} - 1\right\}, & for\ \lambda^{(k)} > 1 \\ 0, & for\ \lambda^{(k)} < 1 \end{cases}, \qquad (7)$$

where $c_1^{(k)}$ and $c_2^{(k)}$ were constitutive parameters, the first with the dimension of a stress and the second being dimensionless, and $\lambda^{(k)}$ described the stretch in the direction of kth collagen fiber family defined as $\lambda^{(k)} = G_q\sqrt{\mathbf{N}^{(k)} \cdot \mathbf{C}\mathbf{N}^{(k)}}$, where G_q was the straightness parameter, and $\mathbf{N}^{(k)} = (\cos\alpha^{(k)}, \sin\alpha^{(k)}, 0)$ represented the direction of the kth collagen fiber family. The angle α^k has been estimated by analyzing the histological images, and we considered the majority of the fibers to be contained within the plane of the skin [38]. Although in principle each family of fibers could show different mechanical behaviors, we assumed that all collagen families shared the same constitutive parameters within each sample, namely $c_1^{(k)} = c_1$, and $c_2^{(k)} = c_2$, for $k = 1, 2, \dots\dots n$. This simplification of the constitutive model helped to provide a clearer interpretation of the contribution of the skin microstructure to the macroscopic level mechanical response of skin. Finally, $\phi^{(k)}$ and $\alpha^{(k)}$ for each collagen family were estimated based on the location-specific collagen orientation distribution data (**Figure 18 a**). To determine the correct number of collagen families, we conducted a parameter convergence study with the constitutive model. Results

showed that the value of c_1 and c_2 converged when $n = 60$. Therefore, 60 collagen families were adopted for the collagen fiber orientation distribution and constitutive parameter estimation.

2.2.4. Parameter estimation

Constitutive model parameter estimation was carried out using the nonlinear least-squares algorithm implemented in MATLAB (i.e., *lsqnonlin* function). The objective function employed in the optimization problem was

$$e = \frac{\sum_{i=1}^{N}(\sigma_{EXP}-\sigma_{MODEL})_i^2}{\left[\max_{1\leq i\leq N}(\sigma_{EXP})_i\right]^2}, \tag{8}$$

where σ_{EXP} and σ_{MODEL} represented the stress values at different stretch ratios in experimental data and constitutive model, respectively. Stress values at 30 evenly spaced stretch values were considered in the parameter fitting process i.e. $N = 30$. Constitutive parameters c^{gm}, c_1, c_2, and G_q were obtained through the parameter estimation process.

The steps to obtain constitutive parameters for each sample were as follows. First, c^{gm} was estimated by fitting the stress-stretch curve at the initial stretch interval $\lambda = [1, 1.02]$ using only the neo-Hookean model, second, c^{gm} from the previous step was applied to the constitutive model, then c_1, c_2, and G_q were obtained by fitting the entire stress-stretch curve of the sample using the complete constitutive model, see **Equation (5)**. Initial values for each parameters were randomly generated, between 0 to 10^3 for c^{gm}, c_1, and c_2, and between 0.9 to 1 for G_q. Initial values for each parameters were randomly generated, between 0 to 10^3 for c^{gm}, c_1, and c_2, and between 0.9 to 1 for G_q.

2.3. Results

A total of 64 samples were successfully tested. Upon inspection of experimental data, the stress-stretch rupture curve from the upper left sample of animal 1 exhibited an "S" shape instead of the regular "J" shape of other samples, probably due to slipping in the clamps. This sample was therefore excluded from the analysis of rupture data.

2.3.1. Storage condition effect

The five mechanical parameters of Group I samples were evaluated and grouped based on storage protocol (**Figure 15**). A one-way ANOVA showed that storage protocol did not have a significant effect ($p > 0.05$) on initial slope, maximum slope, UTS, rupture strain, or toughness. Additionally, averaged cyclic loading stress-stretch curves and rupture loading stress-stretch curves of Group I samples from each storage protocol were shown in **Figure 16**. NRMSD between the control group (fresh samples) and each of the other three storage protocols were calculated to further compare the influence of the storage protocol on the nonlinear mechanical behavior of skin (**Table 1. The** NRMSD between each storage protocol and the control group for cyclic loading stress-stretch curves and rupture loading stress-stretch curves. were calculated. Results showed that Protocol II had the lowest total NRMSD (7.11%), followed by Protocol III (13.75%) and Protocol I (16.97%).

Since the influence of different storage conditions on the mechanical properties of skin was not significant, samples from Group I and Group II animals were put together to study the influence of location, orientation, and sex on skin mechanical properties.
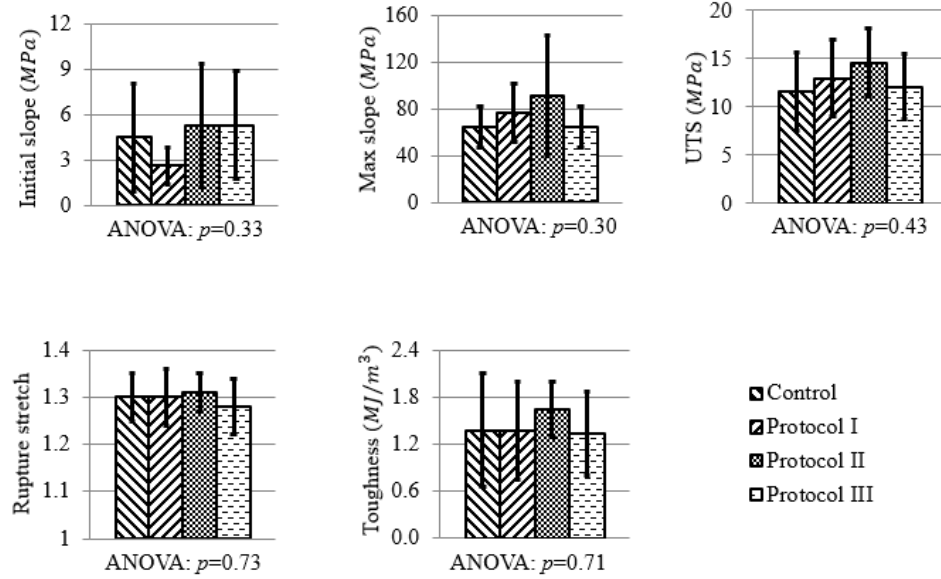
Figure 15. Influence of storage condition on initial slope, maximum slope, UTS, rupture strain, and toughness. Values shown in the bar graph are means and standard deviations. Values shown below each bar graph are *p*-values of one-way ANOVA comparing the mechanical parameter difference between four different storage conditions.
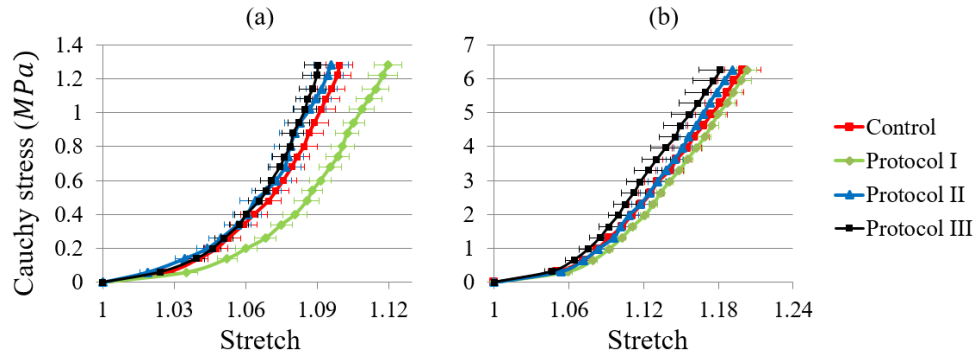
Figure 16 (**a**) Averaged cyclic loading curves and (**b**) averaged rupture loading curves of each storage protocol. Horizontal bars on each curve represent standard errors.

Table 1. The NRMSD between each storage protocol and the control group for cyclic loading stress-stretch curves and rupture loading stress-stretch curves.

	Cyclic loading	Rupture loading	Total
Protocol I	13.21%	3.77%	16.97%
Protocol II	4.67%	2.44%	7.11%
Protocol III	5.94%	7.81%	13.75%

2.3.2. *Location, orientation and sex effect*

Mechanical parameters evaluated from rupture stress-stretch curves were grouped based on three different factors, i.e., location (upper vs. lower back), orientation (axial vs. transverse direction), and sex (male vs. female). Group means and standard deviations based on different factors were shown in bar graphs in **Figure** 17. Influence of location, orientation and sex on (a) initial slope**,** (b) maximum slope**,** (c) rupture strain**,** (d) UTS, **and** (e) toughness. **Means** and standard deviations are shown in the bar graphs. P-values of the *three-way* ANOVA are shown below the bar graph for comparison within each factor, i.e., upper vs. lower, axial vs. transverse, male vs. female. Statistical significance ($p<0.05$) and strong statistical significance ($p<0.001$) are marked by single and double asterisks, respectively. *P*-values of the three-way ANOVA showing the effect of different factors on mechanical parameters were listed below the corresponding paired bar graphs. Factors that contributed statistical significance were marked using asterisks. No significant differences were found between sexes on mechanical parameters, except for sample thickness (male: $1.66\ mm \pm 0.34\ mm$, female: $1.24\ mm \pm 0.25\ mm$, $p < 0.001$). However, significant differences were detected between locations, and orientations. The lower back had significantly higher values of initial slope, maximum slope, UTS, and toughness when compared to the upper back. Orientation-wise, significant differences were detected between axial and transverse directions for the initial slope, maximum slope, rupture strain, and toughness. The axial direction had higher values of initial slope, rupture strain, and toughness. While transverse samples had higher values of maximum slope.
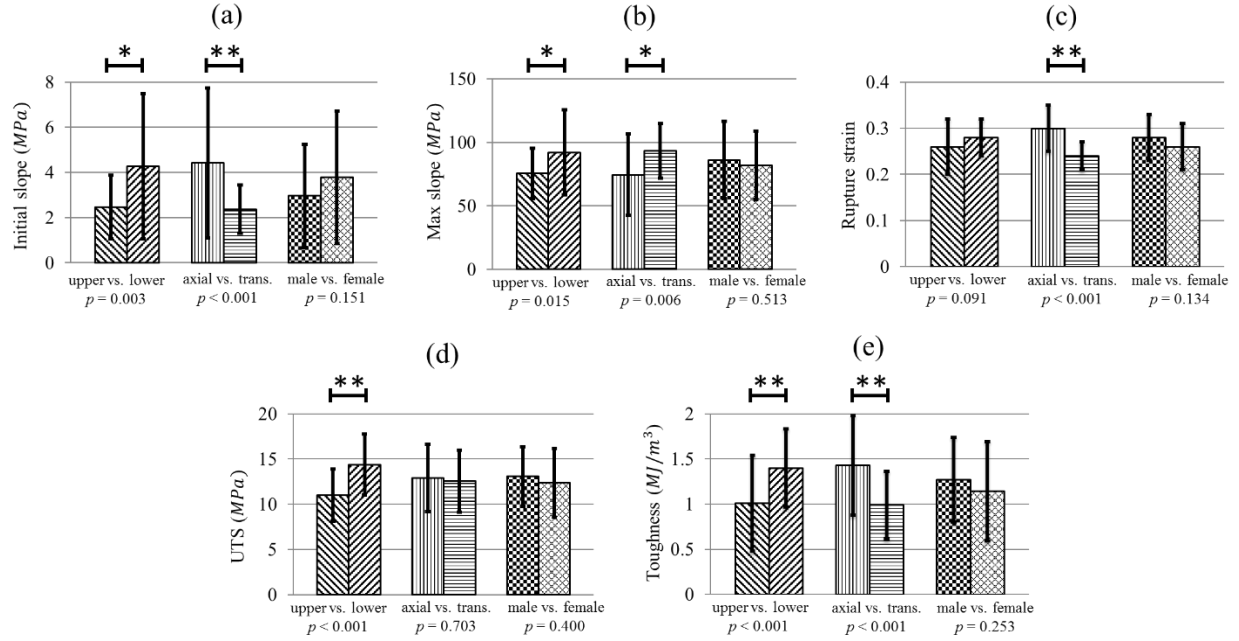
Figure 17. Influence of location, orientation and sex on (**a**) initial slope, (**b**) maximum slope, (**c**) rupture strain, (**d**) UTS, and (**e**) toughness. Means and standard deviations are shown in the bar graphs. *P*-values of the three-way ANOVA are shown below the bar graph for comparison within each factor, i.e., upper vs. lower, axial vs. transverse, male vs. female. Statistical significance ($p < 0.05$) and strong statistical significance ($p < 0.001$) are marked by single and double asterisks, respectively.

2.3.3. Fibers orientation, straightness and relative collagen content

Orientation probability density of collagen fiber bundles for upper right back location were shown in **Figure 18 a**. Each bin represented a collagen family, where the width of the bin w_i was the angle range that a collagen family covered (i.e., $w_i = 3°$), and the height of a bin was the probability density of that collagen family. Probability density was calculated as $v_i = \frac{c_i}{N \cdot w_i}$, where c_i was the number of fibers in the collagen family and N was the total fiber numbers detected. As to the pattern of fiber orientation distribution, collagen fiber bundles aligned predominantly in two directions, 40° to 50° and -40° to -50°, with respect to the spine at all four locations. The collagen fiber bundles straightness for each location was shown in **Figure 18 b**. No significant difference was found between locations. All back locations had mean collagen fiber straightness equal to ~0.95. Relative collagen content was shown for upper and lower back in **Figure 18 c**. A Student

t-test showed that samples from the lower back $(70.0\% \pm 15.1\%)$ have significantly higher relative collagen content when compared to samples from the upper back $(56.6\% \pm 10.2\%)$, with $p = 0.002$.
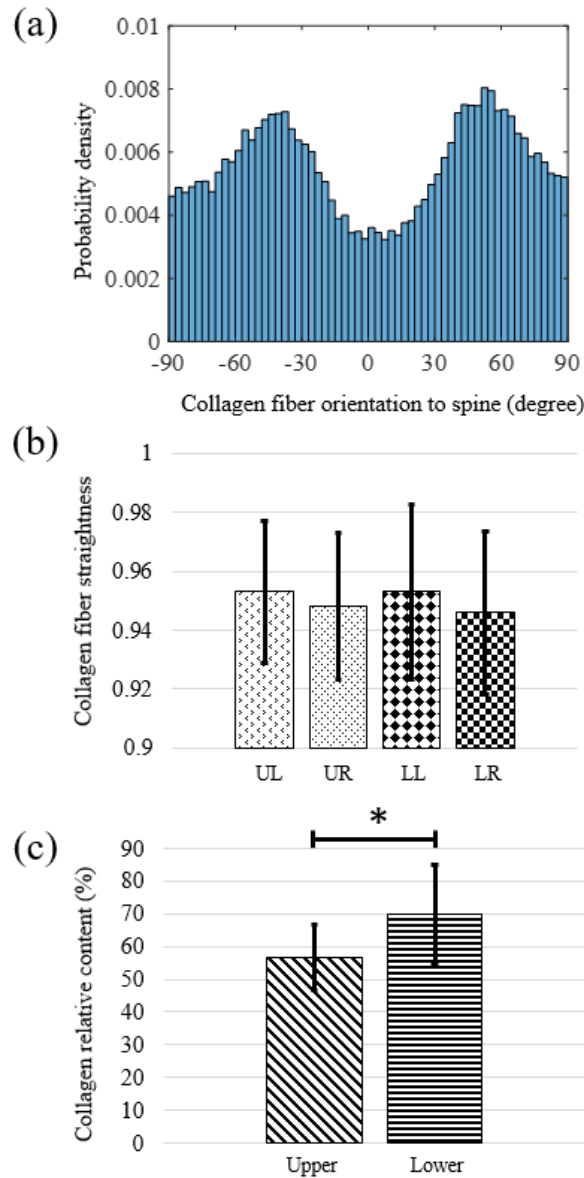
Figure 18. (a) Probability density of 60 collagen fiber families' orientation to spine at upper left location on rat back. **(b)** Means and standard deviations of collagen fiber straightness at four back locations measured in PSR stained histology images. 50 fibers/5samples were measured for each locations. UL – upper left, UR – upper right, LL – lower left, and LR – lower right. **(c)** Means and standard deviations of relative collagen content at upper and lower back measured by collagen area percentage in Masson's trichrome stained histology images. Statistical significance $(p < 0.05)$ is marked using asterisk.

2.3.4. Constitutive model parameters

Representative experimental data and constitutive model with corresponding best-fit constitutive parameters of back skin samples from 2 animals at upper and lower locations, and in axial and transverse directions were shown in **Figure 19**. NRMSD ($2.1\% \pm 0.59\%$ for 64 samples) showed a good agreement between experimental data and constitutive model. A uniqueness study showed that the best-fit constitutive parameters of each sample were independent by the initial guess values.

Best-fit constitutive parameters obtained from the parameter estimation process were then grouped based on three factors, i.e., location, orientation, and sex (**Table 2**). The influence of different factors were evaluated using a three-way ANOVA (**Figure 20**). No significant difference was found between sexes. Significant differences were detected between locations, as well as orientations. Upper back samples had significantly lower values of c^{gm} and G_q, but significantly higher values of c_1 when compared to lower back samples. With respect to the orientation, samples tested in the axial direction had significantly higher values of c^{gm} and G_q, and significantly lower values of c_2 when compared to the transverse direction.
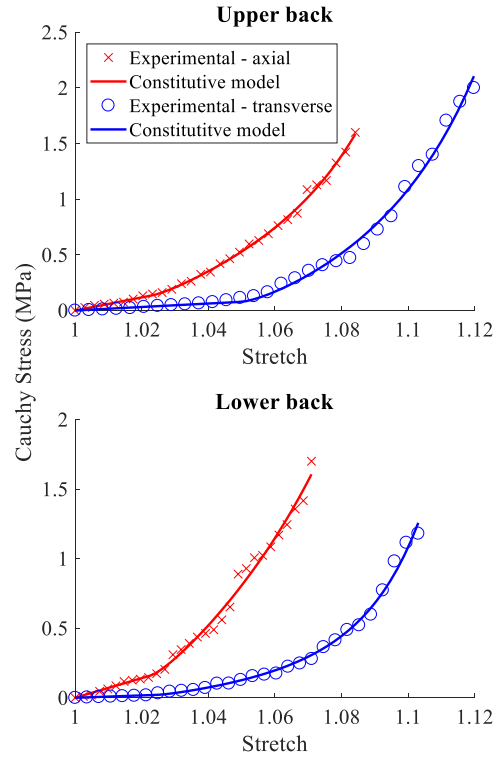
Figure 19. Representative experimental data and constitutive model with corresponding best-fit constitutive parameters at upper and lower rat back locations. Axial experimental data are from animal 5, while transverse experimental data are from animal 10. Best-fit constitutive parameters of the simulated stress-stretch curves shown in the figure are as follows. Upper back sample in axial direction (animal 5) $c^{gm} = 3.07\ MPa$, $c_1 = 53.27\ MPa$, $c_2 = 51.26$, $G_q = 0.977$; and transverse direction (animal 10) $c^{gm} = 0.82\ MPa$, $c_1 = 65.62 MPa$, $c_2 = 38.06$, $G_q = 0.952$. Lower back sample in axial direction (animal 5) $c^{gm} = 5.91\ MPa$, $c_1 = 69.94\ MPa$, $c_2 = 32.33$, $G_q = 0.978$; and transverse direction (animal 10) $c^{gm} = 0.72\ MPa$, $c_1 = 10.71\ MPa$, $c_2 = 66.88$, $G_q = 0.976$.

Table 2. Means and standard deviations of best-fit constitutive parameters $\boldsymbol{c^{gm}}$, $\boldsymbol{c_1}$, $\boldsymbol{c_2}$, and $\boldsymbol{G_q}$, grouped based on location, orientation, and sex.

	$c^{gm}(MPa)$	$c_1(MPa)$	c_2	G_q
upper	1.16 ± 0.66	61.4 ± 25.42	33.1 ± 15.82	0.96 ± 0.01
lower	2.67 ± 1.95	46.6 ± 27.86	34.8 ± 17.19	0.97 ± 0.01
axial	2.41 ± 2.06	55.4 ± 30.39	29.2 ± 14.99	0.97 ± 0.01
transverse	1.43 ± 0.82	52.7 ± 24.68	38.7 ± 16.59	0.96 ± 0.01
male	1.60 ± 1.36	52.5 ± 26.33	35.3 ± 16.75	0.96 ± 0.01
female	2.24 ± 1.83	55.6 ± 28.95	32.6 ± 16.22	0.96 ± 0.01
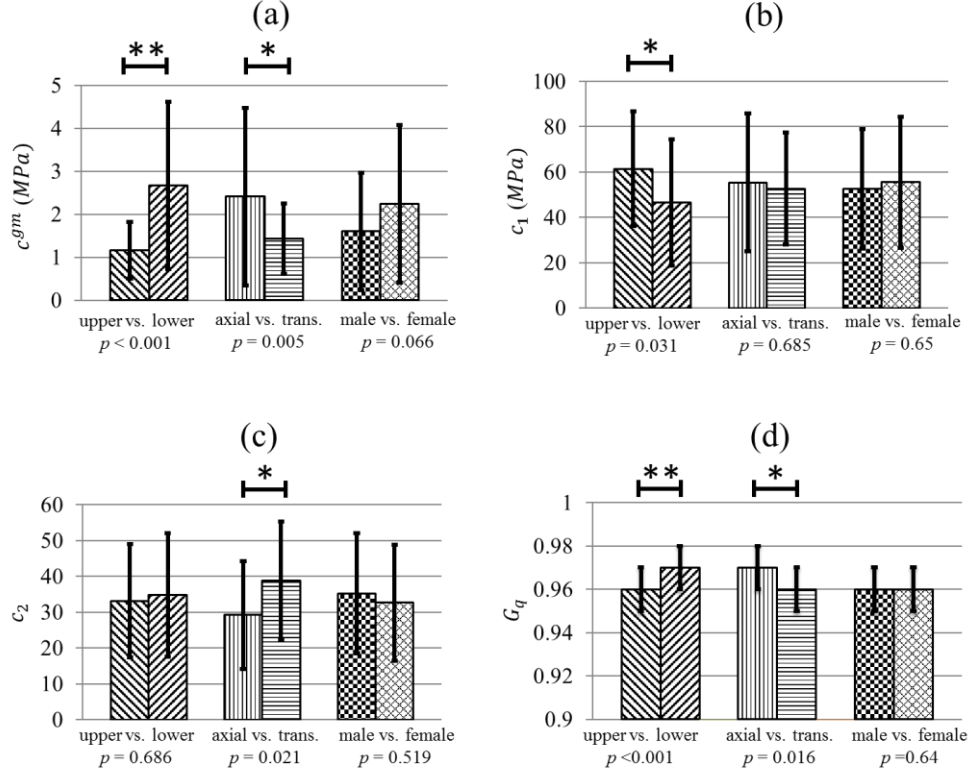
Figure 20. Influence of location, orientation, and sex on best-fit constitutive parameters, (**a**) c^{gm}, (**b**) c_1, (**c**) c_2, (**d**) G_q. Means and standard deviations are shown in the bar graphs. P-values of a three-way ANOVA are shown below the bar graph for comparison within each factor, i.e., upper vs. lower, axial vs. transverse, male vs. female. Statistical significance ($p < 0.05$) and strong statistical significance ($p < 0.001$) are marked by single and double asterisks, respectively.

2.4. Discussion and conclusions

Differences in the mechanical properties of human skin associated with sex have been reported in literature [82], [92]. Similar studies on murine skin were rare [93]. Considering the wide application of rat skin as an alternative model for human skin [94]–[97], it is important to investigate the influence of sex on the mechanical properties of rat skin. Results of our study showed that sex has no significant effect on any of the evaluated parameters of rat back skin. However, male animals showed significantly higher skin thickness when compared to females, which confirmed what had been observed in humans previously [98]. When we investigated the effect of location on the mechanical parameters, we found that the lower back had higher values

of initial slope, maximum slope, UTS, and toughness when compared to the upper back. Tensile test data collected by Haut [99] showed that the lower back had higher UTS compared to the upper back of 2 month-old rats, which agreed with our study. However, our results did not confirm the rupture strain difference between the upper and lower back that were reported in the same study [99]. When it comes to anisotropy, Karimi, *et al.* [76] reported that the transverse direction of mice back skin had higher maximum slope compared to the axial direction, which was supported by our results. Our results also confirmed the higher failure strain of samples tested in the axial direction compared to the transverse direction reported by Haut on 2 month-old rats [99]. However, our findings did not confirm the UTS difference between the axial and transverse direction of 2 month-old rats reported by Haut. Although there is no clear consensus in the literature regarding the influence of location and orientation on the mechanical parameters of rat skin, which may be due to different experimental conditions (preconditioning, testing rate, animal age etc.), the authors are confident in stating that heterogeneity and anisotropy are crucial characteristics of skin mechanical properties and should be addressed when testing this tissue. One limitation of the tests conducted here was that we kept the samples hydrated throughout the test by spraying saline solution (i.e., HBSS) directly on them, at 5 minutes intervals. This may however alter the tissue mechanical behaviors compared to the in vivo condition. Moreover, differences between hydration conditions could be one of the factors that contributed to the discrepancies reported in literature.

Numerous studies have investigated the storage condition effect on skin tissue cell survival rates [100]–[102] for the purpose of skin graft storage in clinical practice. Sample storage is also usually required for skin biomechanics study due to the time interval between sample collecting and sample testing. However, very few studies have reported the storage condition effect on mechanical properties of skin. Marangoni *et al.* [103] recorded the influence of three storage

conditions, i.e. (1) 1.6 °C, (2) 37.8 °C, and (3) -92.8 °C preceded by flash freezing, on mechanical properties of skin samples collected from guinea pigs during the time span of 6 hours. Their study concluded that -92.8 °C storage condition following flash freezing maintained values of maximum stress, maximum strain, maximum stiffness and maximum work input of the skin samples, while 1.6 °C and 37.8 °C significantly altered the values of those evaluated parameters. Foutz *et al.* [104] reported that tissue freezing significantly increased fracture strength, but didn't affect yield strength, ultimate strength. Although conclusions from previous studies are not consistent, it can be generalized that low temperature storage preceded by flash freezing may maintain mechanical properties of skin tissues. Our study compared the influence of three different storage protocols on skin mechanical parameters (**Figure 15**), and we found no significant difference between stored samples and fresh samples. When comparing averaged stress-stretch curves of different storage conditions to those of the controls, we found that Protocol II (i.e. flash freezing, then stored in -78.5 °C, and thawed at 4 °C for 6 hours before testing) led to the smallest NRMSD among the three protocols.

The structure of the collagen network in the dermis is the link that connects the macroscopic level mechanical response of skin to its microscopic structure, and the quantification of its characteristics remains a challenging task. Specifically, collagen fiber bundles orientation distribution, relative collagen content (either mass or volume), and collagen fiber undulation, have been previously shown to play an important role in defining a successful structural constitutive modeling framework [43], [50], [105]. For example, Jor *et al.* [37], [49] quantified collagen orientation distribution in the cross-section of porcine abdomen skin, and Ní Annaidh *et al.* [38] measured collagen orientation distribution in the parallel section of human back skin. In the current study, we developed an automated image analysis routine based on [38]. In order to improve fiber

identification, we used PSR histological staining instead of Van Gieson. One reason for this choice is that collagen fiber bundles can be more easily identified in PSR stained tissue when imaged under polarized light, because of the absence of other constituents in the image, which are instead still visible with Van Gieson stains. Another reason is that fibers with different thicknesses exhibit different colors in a PSR stain under polarized light, which effectively reduces fiber cross-linking and increases the efficiency of recognizing individual collagen fiber bundles, by grouping fibers through color segmentation. Also, Ní Annaidh *et al.* [38] isolated collagen fiber bundles by binarizing the histology image using Otsu's method, which could misidentify some collagen pixels as background. In this study, collagen fiber bundles of different thicknesses were first isolated by their color (**Figure 14 f** - **h**), then those exact collagen pixels were turned into binary images. This method decreased the amount of collagen pixels lost during image processing. Our results also showed that in-plane collagen fiber bundles were distributed mainly in two directions, ±40°~50° with respect to spine, although a certain percentage of fibers were distributed equally in every direction. A similar distribution of collagen fiber bundles has been reported previously in humans [38] and pigs [37]. On one hand, we found no difference in collagen orientation distribution (**Figure 18 a**) or straightness (**Figure 18 b**) between the four locations. On the other hand, we observed a significantly higher relative collagen content in the lower back when compared to the upper back (**Figure 18 c**), which could be a contributing factor to the difference in mechanical parameters observed here (**Figure 17**).

In the microstructural constitutive model presented, the collagen orientation distribution was described by a number of discrete collagen families, which led to a closed-form analytical solution for a collagen fiber bundle. Similar approaches in the literature include the models from Flynn *et al.* [105], Karimi, et al [41], and Groves, *et al.* [40]. The use of discrete collagen families avoids

the sometimes costly numerical integration compared to models that employ continuous fiber orientation distribution [38], [49]. The mass fraction ϕ^α not only described the distribution characteristics of collagen families, but weighed the contribution of ground matrix and collagen. The location-specific measurement of relative collagen content, along with the fiber bundles orientation distribution measurement, ensured that best-fit constitutive parameters could account for the real contribution of each constituent in skin to its macroscopic level mechanical response. Therefore, constitutive parameters from different samples can be further compared to investigate the influence from external factors. The influence of location and orientation detected on the mechanical parameters (**Figure 17**) were also reflected in the constitutive parameters (**Figure 20**), which covered both high-stress and lower-stress ranges of skin mechanical properties, respectively. In our model, the parameter values of c^{gm} (**Figure 20 a**) were directly related to values of initial slope (**Figure 17 a**) since we hypothesized that the ground matrix dominated the response in lower stress range in our constitutive model. It should be noticed that the standard deviations of initial slope and c^{gm} were large. This could be due to experimental errors at the early phase of the testing, whose force response were relatively small. The influence of location and orientation detected in best-fit G_q values differed from the manually measured results. Manually measured G_q values (**Figure 18 b**) showed no location difference, while best-fit G_q values from the constitutive model (**Figure 20 d**) showed significant difference between the upper and lower back, and also significant difference between axial and transverse directions. This discrepancy could come from the following reasons. (1) Limited number of manually measured fiber bundles: only 10 fibers per sample were manually measured, while the best-fit G_q values reflected the averaged straightness of all fiber bundles within a sample. (2) Different reference configuration: manually measured collagen fiber bundles were found in deformation-free samples, while best-fit G_q values for the

46

constitutive model were for samples that had been through preconditioning and cyclic-loading. (3) Inter-specimen variation. However, the averaged value of manually measured G_q had good agreement with that obtained from the parameter estimation process, being 0.95 and 0.96, respectively.

3. **A SUBJECT SPECIFIC MODEL THAT ADDRESSES NONLINEAR MECHANICAL BEHAVIOR OF HUMAN THIGH INFORMED BY IN VIVO EXPERIMENTAL DATA**

3.1.   Overview

The goal of this chapter is to develop a subject-specific FE model that addresses the nonlinear mechanical behavior of thigh soft tissue. A parameter estimation process that matched nonlinear force-deflection behavior of FE model to *in vivo* data was developed. Effects of modeling region dimension (3D vs semi-3D) and constitutive model (neo-Hookean, Mooney-Rivlin, first Order Ogden, and Fung orthotropic) were studied using a subject-specific thigh FE model. After the best two constitutive models were determined, a total of 20 thigh FE models were developed and corresponding best-fit constitutive parameters were obtained using the two constitutive models. Effects of sex and location on thigh soft tissue were also detected on those thigh mechanical parameters.

3.2.   Methods

3.2.1. *Mechanical testing*

We recorded force-deflection data sets from the leg for 20 individuals: 10 males (average age: 20.6 years old, average weight: 76.2 kg, average height: 170.4 cm) and 10 females (average age: 20.9 years old, average weight: 66.4 kg, average height: 162.8 cm), following a previously published protocol [106]. Briefly, we first recorded standard anthropometric measurements, such as height, weight, seated height, buttocks width, and leg dimensions for each participant. Each participant was seated on the ischial tuberosity so that the soft tissue of the thigh was unloaded and undeformed. Then, a custom made hand-held compression device was used to gather force-

deflection data on the proximal, middle, and distal locations on the posterior side of the thigh. Load was applied until a biological barrier was reached.

3.2.2. Geometry generation

The participant specific geometry was recorded for one representative participant (female) employing the following protocol. The participant was seated on the ischial tuberosity so that the thigh was not deformed and the knee was flexed at 90°. A Sense™ V2 3D scanner was used to record the CAD model of the thigh (**Figure 21 b**). A femur geometry obtained from GrabCAD [107] was placed within the model of the thigh, and we used anthropometric measurements of the participant and CT images of thigh cross-sections from literature [108] to ensure the correct size and the accurate position of the femur.

The geometry of the remaining 19 participants was obtained by employing a scaling technique starting from the geometry of the one representative participant. Specifically, the singular thigh CAD model developed was scaled to that of another participant by matching two key participant-specific measurements collected at the time of mechanical testing, namely the length from hip joint to knee joint and the circumference of the middle thigh. All participants' weight and height fell into the US mid-size male and female groups previously published [109]. This enabled us to use a constant diameter for the femur within the same sex group, while the diameter of the femur of male participants was increased by 4.8% with respect to that of female participants [110].

3.2.3. Finite element model

Mesh generation. Each CAD model was cut along two transverse planes, one passing through the joint between buttock and thigh and another passing through the joint between thigh and knee (**Figure 21 c**). Then, the model was meshed (HyperMesh ver.13.0) using 10 nodes tetrahedral elements of size 10 mm. The FE models had an average of 32,062 elements and 47,518 nodes. A

mesh sensitivity study was conducted using the representative participant's model with elements of size 10 mm (i.e., 27,724 elements, 41,227 nodes), elements of size 7.5 mm (i.e., 54,568 elements, 79,830 nodes), and elements of size 5 mm (i.e., 141,083 elements, 203,742 nodes). We compared the normalized root-mean-sqaure deviations (NRMSDs, **Equation (17)**) between force-deflection curves of the FE model with 10 mm-sized elements and the FE model with 7.5 mm and 5 mm-sized elements, at each tested location. All NRMSDs are below 2.2%. This confirms that mesh convergence was achieved using elements of size 10 mm. The soft tissue in the model was then divided into three locations, corresponding to the three testing sites. The same homogenous constitutive model but different constitutive parameters described the lumped mechanical properties of soft tissues (i.e., skin, fat, and muscle) at each location, and the femur was modeled as a rigid body.

3D model. Three $50\ mm \times 50\ mm$ areas were identified at the proximal, middle, and distal locations on the posterior side of the thigh (**Figure 21 d**, top row), each corresponding to a location tested during the *in vivo* experiment. Boundary conditions were applied to the femur (i.e., constrained against displacement and rotation in any direction), to the two cut planes at proximal and distal thigh (i.e., nodes were constrained against longitudinal displacements along the femur longitudinal direction), and to the three testing areas (i.e., nodes were restricted to move only in an anterior-posterior direction, to prevent instability during deformation). Additionally, participant-specific compression forces at each location, as recorded *in vivo*, were applied to one testing area at a time. Compression forces were applied in 20 evenly spaced steps from zero to the maximum value recorded in the experiment, and the nodal displacements of the compressed area

at each step were recorded and averaged. Simulated force-deflection curves were then compared

to the experimental data to estimate the best-fit constitutive parameters.
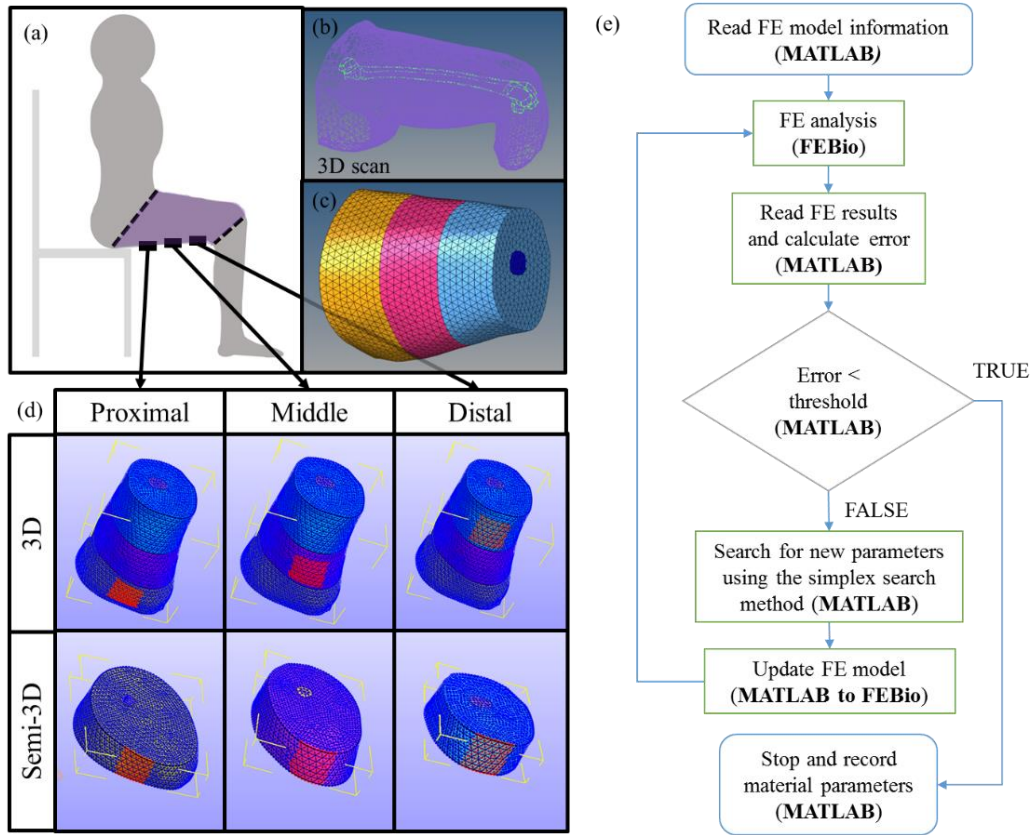
Figure 21. (**a**) Schematic of the seating positioning for a participant during 3D scanning. (**b**) Thigh CAD model obtained from 3D scanning of the thigh of a representative participant. (**c**) Representative 3D FE model. (**d**) Dimensions and positioning of testing areas for the 3D FE model, on top, and the semi-3D FE model, on the bottom. From left to right, proximal, middle, and distal thigh testing locations are shown in red. (**e**) Flow chart of the constitutive parameter optimization protocol.

Semi-3D model. Additionally, we developed three semi-3D FE models of one representative

participant. We cut the thigh CAD model at the proximal, middle, and distal tested areas

respectively, using two transverse planes placed at $50\ mm$ from one other. These three $50\ mm$

long (in the femur longitudinal direction) CAD models were then meshed using the same element

type and element size as the 3D FE model described above (**Figure 21 d,** bottom row). The

boundary conditions applied to the femur, cut planes, and tested areas, the load application

procedure, and the constitutive parameter estimation were the same as discussed above for the full

3D model. We then compared the best-fit constitutive parameters of 3D and semi-3D FE models that described the same set of experimental data, as well as the simulated force-deflection data of 3D and semi-3D FE model estimated employing the same set of constitutive parameters.

3.2.4. Constitutive models and parameter optimization

Neo-Hookean model. The strain energy function for the neo-Hookean model [111] was defined as

$$\Psi^{nH} = c_1^{nH}(I_{\mathbf{C}} - 3) + \frac{1}{2}K^{nH}(\ln J)^2, \tag{9}$$

where c_1^{nH} was a constitutive parameter with the dimension of a stress, $I_{\mathbf{C}} = tr(\mathbf{C})$ and $J = det(\mathbf{C})$ were respectively, the first and third invariant of the right Cauchy-Green strain tensor, $\mathbf{C} = \mathbf{F}^T\mathbf{F}$, where $\mathbf{F}$ was the deformation gradient. In the principal reference system, one could write $\mathbf{F} = diag[\lambda_1, \lambda_2, \lambda_3]$, where λ_1, λ_2, and λ_3 represented the stretches in the principal directions. The coefficient K^{nH} represented the bulk modulus-like penalty parameter, which was defined as $K^{nH} = \frac{2c_1^{nH}}{(1-2v)}$, where v represented the Poisson's ratio. In all the material descriptions presented in this work we considered the Poisson's ratio to be $v = 0.485$ [20] to ensure a nearly incompressible material description.

Mooney-Rivlin model. The strain energy function for the Mooney-Rivlin model [112] was defined as

$$\Psi^{MR} = c_1^{MR}(I_{\mathbf{C}} - 3) + c_2^{MR}(II_{\mathbf{C}} - 3) + \frac{1}{2}K^{MR}(\ln J)^2, \tag{10}$$

where c_1^{MR} and c_2^{MR} were constitutive parameters with the dimension of a stress, $I_{\mathbf{C}}$ and J were the first and third invariant of $\mathbf{C}$, as defined above, and $II_{\mathbf{C}} = \frac{1}{2}[(tr(\mathbf{C}))^2 - tr(\mathbf{C}^2)]$ was the

second invariant of the tensor $\mathbf{C}$. The bulk modulus-like penalty parameter K^{MR} in this case was

defined as $K^{MR} = \frac{2(c_1^{MR}+c_2^{MR})}{(1-2v)}$.

First order Ogden model. The strain energy function for the first order Ogden model [113]

was defined as

$$\Psi^{Ogd} = \frac{\mu^{Ogd}}{\alpha^{Ogd}} \left(\lambda_1^{\alpha^{Ogd}} + \lambda_2^{\alpha^{Ogd}} + \lambda_3^{\alpha^{Ogd}} - 3 \right) + \frac{1}{2} K^{Ogd} (\ln J)^2, \tag{11}$$

where μ^{Ogd} and α^{Ogd} were constitutive parameters with the dimension of a stress and

dimensionless, respectively, J was the third invariant of $\mathbf{C}$ and λ_1, λ_2, and λ_3 represented the

stretches in the principal directions, as defined above. The bulk modulus-like penalty parameter

K^{Ogd}, in this case was defined as $K^{Ogd} = \frac{\mu^{Ogd}\alpha^{Ogd}}{2(1-2v)}$. We defined also the parameter initial

stiffness as

$$E^{Ogd} = \frac{3}{2}\mu^{Ogd}\alpha^{Ogd}, \tag{12}$$

which corresponded to the Young's modulus in the infinitesimal elasticity theory, i.e., represented

the slope of the stress-strain curve under uniaxial loading when the material underwent small

deformation.

Fung orthotropic model. With the assumption of isotropic symmetry, the strain energy

function of the Fung orthotropic model [114] was defined as

$$\Psi^F = \frac{1}{2}c^F \left(e^{\tilde{Q}} - 1 \right) + \frac{1}{2} K^F (\ln J)^2, \tag{13}$$

where c^F was a constitutive parameter with the dimension of a stress, J was the third invariant of

$\mathbf{C}$, and $K^F = \frac{E^F}{3(1-2v)}$ was the bulk modulus-like penalty parameter, where E^F represented the

initial stiffness parameter, i.e., the Young's modulus in the infinitesimal elasticity theory. Finally,

we defined the exponential parameter $\tilde{Q}$ as

$$\tilde{Q} = \gamma^F (\boldsymbol{I} : \boldsymbol{E})^2 + \gamma^F \frac{(1-2\nu)}{\nu} \boldsymbol{I} : \boldsymbol{E}^2, \tag{14}$$

where $\boldsymbol{E} = \frac{1}{2}(\boldsymbol{C} - \boldsymbol{I})$ was the Green strain tensor, $\boldsymbol{I}$ was the identity tensor, and the dimensionless constitutive parameter γ^F was defined as

$$\gamma^F = \frac{E^F \nu}{c^F (1+\nu)(1-2\nu)} \,. \tag{15}$$

Constitutive parameter optimization. Constitutive parameters at proximal, middle, and distal thigh locations were optimized employing the simplex search method implemented in MATLAB (i.e., function *fminsearch*). The FE simulation in each optimization iteration was performed in FEBio. The flow chart of the optimization process is shown in **Figure 21 e**. The goal of the optimization process was to minimize the difference between the FE simulated force-deflection curves and the experimental data at each location. The objective function to be minimized was

$$e = NRMSD_{prx} + NRMSD_{mid} + NRMSD_{dis}, \tag{16}$$

where $NRMSD_{prx}$, $NRMSD_{mid}$, and $NRMSD_{dis}$ were normalized root-mean-square deviation (NRMSD) estimated at each location α as

$$NRMSD_\alpha = \frac{\sqrt{\frac{\sum_{i=1}^{n}(d_\alpha^{FE} - d_\alpha^{EXP})_i^2}{n}}}{(d_\alpha^{EXP})_{max}} \tag{17}$$

where n was the number of loading steps (i.e., $n = 20$), d_α^{FE} and d_α^{EXP} were the deflection values for the α location from the FE simulation and experimental measurement respectively, and $(d_\alpha^{EXP})_{max}$ represented the maximum experimental values of deflection for each location α (i.e., the deflection measure for the maximum load). The initial guess constitutive parameters for each constitutive model were obtained from literature, as shown in **Table 3**, and all material parameter values were constraint to be positive.

Table 3. Initial guess constitutive parameters for each constitutive model.

Constitutive model	Constitutive parameter	Initial guess parameter value	Reference
neo-Hookean	c_1^{nH} [kPa]	8.50	Linder-Ganz *et al.* [19]
Mooney-Rivlin	c_1^{MR} [kPa]	1.65	Verver *et al.* [21]
	c_2^{MR} [kPa]	3.35	
Ogden	μ^{Ogd} [kPa]	3	Oomens *et al.* [16]
	α^{Ogd}	30	
Fung orthotropic	E^F [kPa]	10	Pilot investigation of current study

3.2.5. *Statistical analysis*

After the best-fit constitutive parameters of all 20 participants were obtained, statistical analysis was carried out to determine the influence of sex and location on constitutive parameters. Student's t-test was utilized to determine the sex influence on constitutive parameters at each thigh location, while one-way repeated measures ANOVA, followed by Holm-Sidak post-hoc test, was utilized to determine the influence of location on constitutive parameters within each sex group.

3.3. Results

3.3.1. *Effects of the choice of constitutive model and of modeling region dimension*

All results in this section have been evaluated considering the geometry and mechanical properties collected experimentally for one representative participant.

Effect of the choice of constitutive model. Constitutive model effects were investigated using a 3D FE model. **Figure 22** showed experimentally measured (symbols) and numerically calculated (lines) compression force-deflection curves for each thigh location and for each constitutive model considered. All sections of **Figure 22 a - d** showed the same three sets of experimental data collected *in vivo*. Each section of **Figure 22** also showed the numerical results for a 3D FE model, each of these models had the same geometry, and the soft tissue was described employing one of the four constitutive models. The numerical results shown have been obtained employing the

optimized constitutive parameters, and the results were presented for each testing location, namely proximal (solid), middle (dashed), and distal thigh (dotted). Values of best-fit constitutive parameters for each constitutive model and each location were also reported in **Table 4.** The NRMSD, **Equation (17)**, between the 3D FE simulation and the experimental data was calculated for each tested location and for each constitutive model adopted, in addition to the total NRMSD, **Equation (16)**. The neo-Hookean model had the largest total NRMSD (35%), followed by the Mooney-Rivlin model (26%), the Fung model (18%), and finally the first order Ogden model (8%). In the analysis of the datasets of the overall 20 participants we employed fun orthotropic and the Ogden material models.
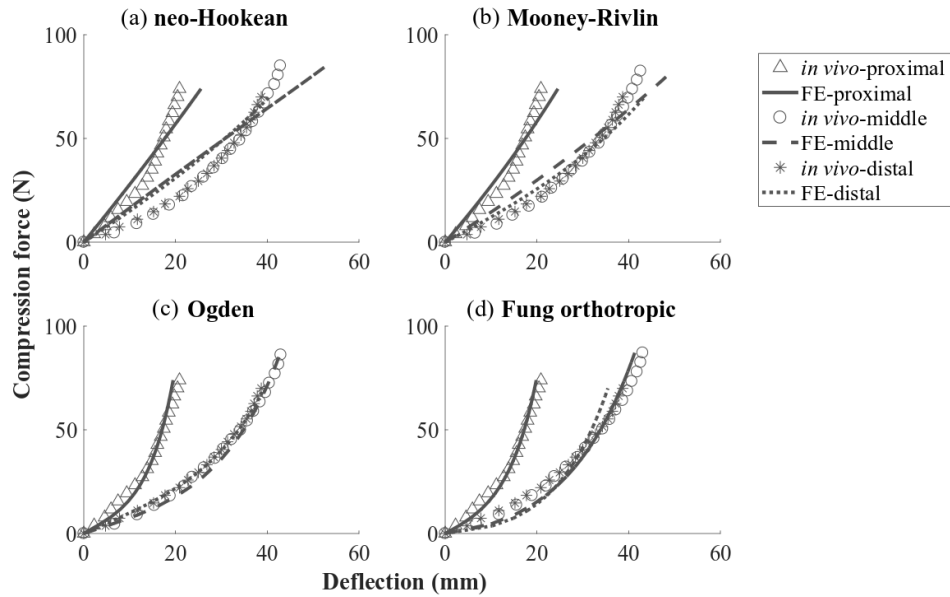
Figure 22. Compression force-deflection curves from experimental measures (symbols) and model predictions (lines) for each location and each constitutive model considered. (**a-d**) The same experimental data are shown in every section, representing the mechanical behavior for representative participant F6 at the proximal (triangles), middle (circles), and distal (asterisks) locations. Also shown are the model predictions after parameter optimization for each location, namely proximal (solid line), middle (dashed line), and distal (dotted line). The models considered are (**a**) neo-Hookean, (**b**) Mooney-Rivlin, (**c**) Ogden, and (**d**) Fung orthotropic.

Effect of the choice of modeling region dimension. First, we compared best-fit constitutive parameters optimized for 3D and semi-3D FE models for the three thigh regions, employing the same experimental data set. Percentage differences between the semi-3D and 3D models were

shown in **Table 4**. The largest difference occurred at the middle thigh location for each constitutive

model: 84% for neo-Hookean, 253.2% for Mooney-Rivlin, 385.7% for Ogden, and 99.3% for Fung.

We then compared force-deflection mechanical behavior of the 3D and semi-3D FE models

employing the best-fit constitutive parameters evaluated for the 3D FE model shown in **Table 4**.

Figure 23 shows deflection differences between the semi-3D FE model and 3D FE model (i.e.,

$d^{semi-3D} - d^{3D}$) for each constitutive model at each location (**Figure 23 a-c**, respectively).

The NRMSD between the semi-3D FE model and the 3D FE model at each location for each

constitutive model were also calculated. A total value of NRMSD is reported here, estimated as

the sum of the values at each location. The Mooney-Rivlin constitutive model showed the largest

total NRMSD (81%), followed by the neo-Hookean (64%), Ogden (38%), and Fung (29%). It is

important to notice that the effect of the modeling region dimension choice (semi-3D vs. 3D)

affects the predicted behavior more dramatically than the choice of constitutive model, based on

the value of total NRMSD.

Table 4. Best-fit constitutive parameters at proximal, middle, and distal thigh location for each constitutive model (i.e., neo-Hookean, Money-Rivlin, Ogden, Fung orthotropic). Experimental data collected for representative subject F6 have been used to inform the 3D and semi-3D FE model. The percentage difference of best-fit constitutive parameters between the two types of model at each thigh location are shown in the column titled as "%" (note: positive values indicate semi-3D model have higher parameter values, and negative values indicate 3D model have higher parameter values).

Constitutive model	Constitutive parameter	Proximal thigh			Middle thigh			Distal thigh		
		3D	Semi-3D	%	3D	Semi-3D	%	3D	Semi-3D	%
neo-Hookean	c_1^{nH} [kPa]	8.50	11.90	40.0	3.12	5.74	84.0	3.02	3.61	19.5
Mooney-Rivlin	c_1^{MR} [kPa]	2.18	2.22	1.8	1.49	1.74	16.8	1.73	1.84	6.4
	c_2^{MR} [kPa]	6.00	9.69	61.5	1.11	3.92	253.2	0.62	1.84	196.8
Ogden	μ^{Ogd} [kPa]	0.49	2.30	369.4	0.49	2.38	385.7	1.70	3.43	101.8
	α^{Ogd}	35.78	12.97	-63.8	11.85	6.00	-49.4	5.38	3.50	-34.9
Fung orthotropic	E^F [kPa]	25.30	18.25	-27.9	3.00	5.98	99.3	2.70	3.22	19.3
	c^F [kPa]	3.20	0.95	-70.3	16.70	13.41	-19.7	23.30	16.31	-30.0
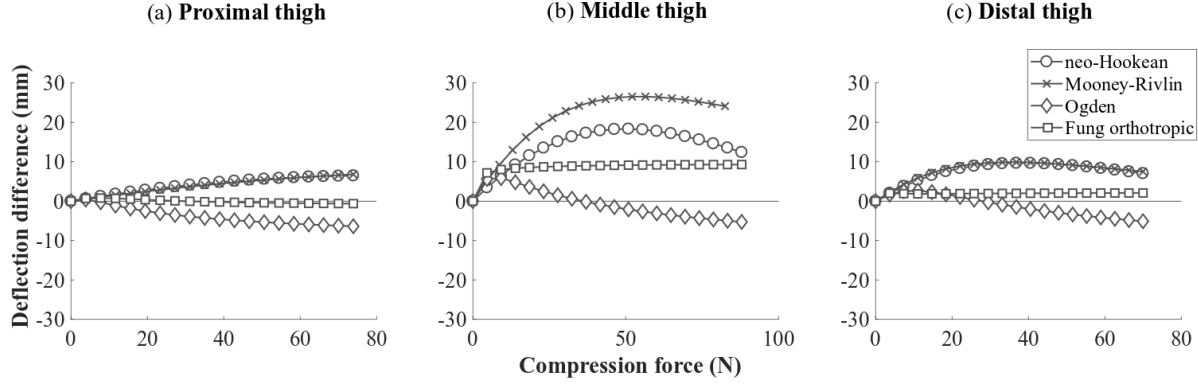
Figure 23. Mechanical behavior comparison between 3D and semi-3D FE thigh models of participant F6 at (**a**) proximal thigh, (**b**) middle thigh, and (**c**) distal thigh. Horizontal axis represents forces applied to the soft tissue of thigh at each loading step, while the vertical axis represents deflection difference between semi-3D FE model and 3D FE model at each loading step, i.e., $d^{semi-3D} - d^{3D}$.

3.3.2. Effect of sex and location

Best-fit constitutive parameters for Ogden and Fung models were obtained for all 20 participants, employing fully 3D geometries scaled to match the anatomical measures of each participant. **Figure 24** showed box plots for the constitutive parameters for both models, grouped by sex (i.e., male and female) and location (i.e., proximal, middle, and distal thigh). Specifically, **Figure 24** showed the parameters μ^{Ogd}, α^{Ogd}, and E^{Ogd} for the Ogden model on the left, where E^{Ogd} was calculated employing **Equation (12)**. The parameters c^F, γ^F, and E^F for the Fung orthotropic model are shown on the right, where γ^F was calculated employing **Equation (15)**.

Effect of sex. The constitutive parameters for each model were compared between males and females at each location. The results of the statistical analysis were presented in **Table 5**. For the Ogden model, Student's t-test found that males had a significantly higher value of μ^{Ogd} at the proximal thigh location ($p < 0.05$), as well as a higher value of E^{Ogd} at the proximal and middle thigh locations ($p < 0.05$ for both locations) when compared to females. For the Fung orthotropic model, males had a higher value of E^F at the middle thigh location ($p < 0.05$), and a higher value of γ^F at the proximal thigh location ($p < 0.05$).

Effect of location. Since we detected multiple differences in constitutive parameters between male and female participants, we analyzed the effect of location on the constitutive parameters within the same sex. One-way repeated measures ANOVA found that location had a significant effect on (1) α^{Ogd} and E^{Ogd} for the Ogden model ($p < 0.001$ for both parameters and for both male and female group) and (2) all constitutive parameters E^F, c^F, and γ^F for the Fung orthotropic model ($p < 0.001$ for both male and female group for all parameters). To better understand which location comparisons contributed to the differences in the constitutive parameters, we carried out a Holm-Sidak post-hoc pairwise test for the following locations: proximal vs. middle, proximal vs. distal, and middle vs. distal. The results of the statistical analysis were presented in Error! Reference source not found..

Table 5. *P*-values of Student's t-test comparing sex difference on Ogden and Fung orthotropic constitutive parameters at different thigh locations. The gray areas highlight the statistical significance, i.e., $p < 0.05$.

	Male vs Female		
	Proximal thigh	Middle thigh	Distal thigh
μ^{Ogd}	0.038	0.429	0.865
α^{Ogd}	0.682	0.235	0.547
E^{Ogd}	0.023	0.021	0.846
c^F	0.170	0.502	0.223
γ^F	0.035	0.252	0.105
E^F	0.101	0.004	0.297

Table 6. *P*-values of Holm-Sidak post-hoc pairwise tests comparing model parameter difference between different thigh locations, in male and female subjects group, for both Ogden and Fung constitutive models, respectively. The gray areas highlight the statistical significance, a lighter gray corresponds to statistical significance ($p < 0.05$), and a darker gray corresponds to strong statistical significance ($p < 0.001$).

	Male			Female		
	Prx vs Mid	Prx vs Dis	Mid vs Dis	Prx vs Mid	Prx vs Dis	Mid vs Dis
α^{Ogd}	<0.001	<0.001	<0.001	<0.001	<0.001	<0.001
E^{Ogd}	<0.001	<0.001	<0.001	<0.001	<0.001	0.052
c^F	<0.001	<0.001	0.020	<0.001	0.001	0.050
γ^F	<0.001	<0.001	0.186	<0.001	<0.001	0.017
E^F	<0.001	<0.001	<0.001	<0.001	<0.001	0.001
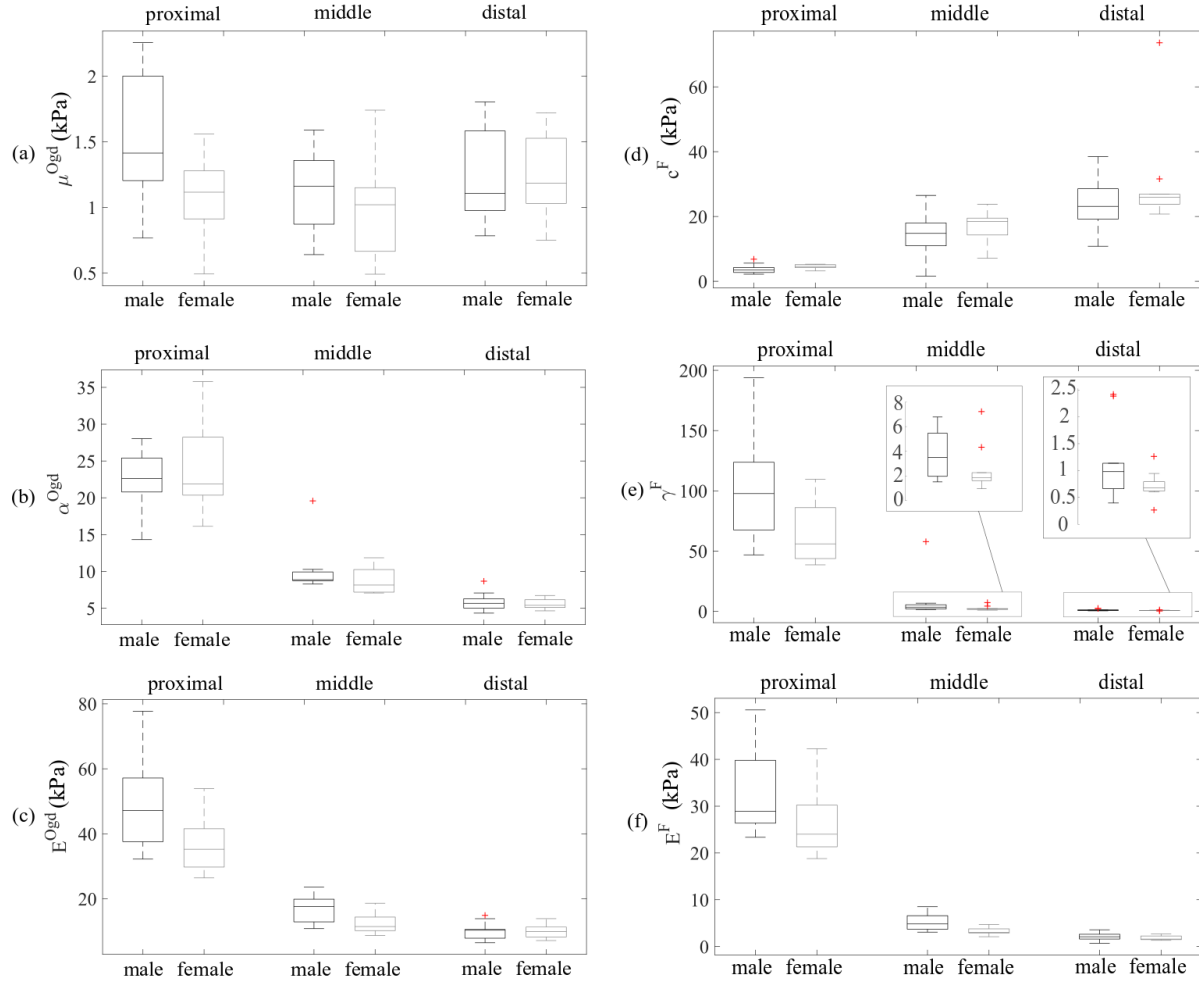
Figure 24. Best-fit Ogden model and Fung orthotropic model parameters, i.e., (**a**) μ^{Ogd}, (**b**) α^{Ogd}, (**c**) E^{Ogd}, (**d**) c^F, (**e**) γ^F, and (**f**) E^F for 20 tested subjects, at proximal, middle, and distal thigh locations, respectively. Parameter values are grouped based on location (marked at the top of each plot) and sex (marked at the bottom of each plot). The central mark within the box indicates the group median, and the bottom and top edges of the box indicate the 25th and 75th percentiles, respectively. The whiskers extend to the most extreme data points not considered outliers, and the outliers are plotted individually using the '+' symbol.

3.4.   Discussion and conclusions

Nonlinearity is a unique characteristic of soft biological tissues and failing to include that within models could significantly affect the accuracy of the predictions. However, to be able to capture non-linear behavior in large deformations, one needs to have access to experimental data that (1) record both forces and deformations simultaneously and (2) expand over an appropriate loading range. In other words, there is a need for data from a mechanical test that captures the *in*

vivo mechanical behavior of soft tissues under large deformations, in an appropriate full-body configuration (i.e., seated vs. laying down). Such data sets have not been available until recently [106]. Previously published data still made an effort to describe the nonlinearity of the thigh and buttocks soft tissues. For example, some studies obtained constitutive parameters from literature and later validated the FE model by reporting the error between the FE simulation and the experimental data [19]–[21]. Other studies performed an optimization to estimate the best-fit constitutive parameters that minimized the error between the FE simulation and the experimental data in one specific configuration [27], [28]. The experimental data available for both approaches were, however, limited and described the deformations corresponding to one loading configuration (i.e., weight-bearing configuration in upright sitting position). Due to the non-linear behavior of soft tissues, we propose that to have access to data in only two configurations, namely an unloaded position and a loaded seated position, is not sufficient to describe accurately the mechanical behavior of the tissues. This is a pressing issue, especially when determining the stress distributions within the tissue that cannot be directly experimentally validated.

The optimization process in this study used the simplex search algorithm (*fminsearch* function in MATLAB). A major reason of using this algorithm was that it was a derivative-free method. Algorithms like trust-region would require gradient information of the objective function. The objective function in our study had no analytic expression and perform like a black box: inputs were the constitutive parameters and outputs were the NRMSDs between the FE simulation and experimental data. Due to the lack of analytic expressions, the convexity of the objective function cannot be confirmed. Therefore the optimized constitutive parameters could be solutions to local minima instead of global minima. However, the optimized constitutive parameters were of the same magnitude as those in literature (**Table 3**) and provided good match to experimental data.

They could be seen as a subset of reasonable solutions, if multiple solutions existed. It is important to notice that *fminsearch* does not provide constraints for the optimized parameters. Therefore, constraints were added in the optimization process to give artificial high error values for parameter searching attempts that fell out of constrained area (i.e., constitutive parameters being positive).

The optimization procedure in this study compared deflection estimated by FE simulation to deflection from a unique experimental dataset collected *in vivo* for a value of loading that gradually increased from 0 to a maximum load [106]. Because of the continuous nature of the experimental dataset, this work had the capability of accurately describing the mechanical behavior of the thigh soft tissues for a large range of loading configurations. For this reason, we had the opportunity to compare the accuracy of four different materials models in describing the behavior of soft tissues. We showed that 3D FE models employing the neo-Hookean and the Mooney-Rivlin material models (i.e., NRMSD = 35% and 26% respectively) described the thigh soft tissue mechanical behavior of the representative subject less accurate than Fung orthotropic and first order Ogden material models (i.e., NRMSD = 18% and 8% respectively). As to the form of discrepancy between FE simulation and in vivo data, we observed that neo-Hookean and Mooney-Rivlin material model largely underestimated deformations at the low force level and overestimated deformations at the high force level (**Figure 22** a-b). In other words, neo-Hookean and Mooney-Rivlin material models were "less non-linear" than the in vivo data of the representative subject. In comparison, Fung orthotropic model overestimated deformations at the low force level and underestimated deformations at the high force level (**Figure 22** d). In other words, Fung orthotropic material model was "more non-linear" for the in vivo data of the representative subject. Meanwhile, first order Ogden material model offered the lowest error (**Figure 22** c). The strain energy function formulation of each material model also matched the mechanical behavior characteristics we

observed above. Being a polynomial function with exponents values (α^{Ogd}) adjustable, first order Ogden material model can describe non-linear mechanical behavior in a broad range. Being special cases of Ogden material model (i.e., neo-Hookean is a special case of first order Ogden material model, Mooney-Rivlin is a special case of second order Ogden material model), the exponents values of neo-Hookean and Mooney-Rivlin material models are fixed and therefore the non-linear mechanical behavior they can describe are largely limited. Similarly, the mechanical behaviors that Fung orthotropic material model can accurately describe are limited by the natural exponential function. With the results of first order Ogden model being more accurate than Fung orthotropic material, it suggests that the force-deflection curves in this dataset show a more polynomial than natural exponential behavior, overall. After examining the force-deflection behavior characteristics of data from the remaining 19 subjects, we determined the neo-Hookean and Mooney-Rivlin material model were not suitable to describe the highly non-linear in vivo data in this study. Therefore, Fung and first order Ogden model were employed for the remaining 19 FE models. It is important to notice that neo-Hookean and Mooney-Rivlin material models are still commonly used in soft tissue modeling [115], [116], our results however suggest that these material models should be used with care, along with proper experimental data, parameter optimization process, and detailed microstructural information [117].

In this study we also quantified the differences between 3D FE model and semi-3D FE model in two ways: (1) the constitutive parameter differences of the two types of model when fitting the same set of experimental data and (2) the force-deflection mechanical behavior difference when employing the same set of constitutive parameters. Regarding the first approach, as shown in **Table 4**, semi-3D models, when compared to 3D models, could overestimate certain mechanical parameters values (in the case of neo-Hookean, Mooney-Rivlin, the μ^{Ogd} parameter for Ogden,

and the E^F at middle and distal thigh location for Fung) and underestimate others (α^{Ogd} for Ogden, and c^F for all locations and E^F at proximal thigh location for Fung). This suggested that constitutive parameters provided by semi-3D model depicted experimental data in a stiffer fashion compared to the 3D model for *in vivo* data in current study, in terms of initial stiffness (i.e., $E^{nH} = 6c_1^{nH}$, $E^{MR} = 6(c_1^{MR} + c_2^{MR})$, $E^{Ogd} = \frac{3}{2}\mu^{Ogd}\alpha^{Ogd}$, and E^F given in **Equation (15)**, with E^F at proximal thigh being an exception). Regarding the second approach, as shown in **Figure 23**, a positive deflection difference value indicated that semi-3D models showed a more compliant behavior when compared to the 3D FE model, while a negative value indicated a less compliant behavior. When the neo-Hookean or the Mooney-Rivlin constitutive laws were employed, the deflection differences were positive for all values of load at all locations, suggesting that semi-3D models behaved in a more compliant way when compared to the 3D FE model for *in vivo* data in current study. The same behavior was observed for the Fung model at the middle and distal locations. In this case, the use of constitutive parameters estimated for a 3D model to perform a semi-3D analysis would lead to underestimating the load needed to cause a certain displacement and ultimately to underestimating the stress distribution within the thigh. On the other hand, when the Ogden model was employed in all locations and the Fung orthotropic model was employed at the proximal location, the deflection difference have positive values for small loads and negative values for large loads. This suggested that, when using parameters that have been optimized for a 3D model to perform a semi-3D FE analysis, one would overestimate the values of loads needed to apply a large deflection. This would likely lead to overestimating the stress state within the tissue, specifically for the seated condition.

We propose that the effect due to a choice of modeling region dimension (i.e., semi-3D vs. 3D) can largely affect mechanical prediction. The best-fit constitutive parameters can be

significantly different between a semi-3D model and a fully 3D model when optimized using the same experimental dataset (e.g., at middle thigh location, best-fit μ^{Ogd} values of semi-3D model was 3.9 times that of the 3D model). Furthermore, when using constitutive parameters optimized for a 3D model to perform a semi-3D analysis, the error in the prediction can be as high as 44.56%. While we do not think that the specific conclusions based on a single subject study are generalizable, due to the complexity of subject-specific soft tissue geometries and boundary conditions, we want to highlight that significant differences between semi 3D model and full 3D model exist and need to be taken into account when comparing results from different studies. Furthermore, even within the single-subject study, the difference between semi-3D and 3D model are inhomogeneous and unpredictable. For instance, the semi-3D model can, with respect to the 3D model, both underestimate and overestimated the values of E^F, based on location as shown in **Table 4**, and it can both overestimate and underestimate predicted displacement, based on material model as shown in **Figure 23**.**Figure 23.** Mechanical behavior comparison between 3D and semi-3D FE thigh models of participant F6 at (**a**) proximal thigh, (**b**) middle thigh, and (**c**) distal thigh. Horizontal axis represents forces applied to the soft tissue of thigh at each loading step, while the vertical axis represents deflection difference between semi-3D FE model and 3D FE model at each loading step, i.e., $d^{semi-3D} - d^{3D}$. These results suggested that, when describing the same *in vivo* mechanical behavior, constitutive parameters obtained from one modeling condition can be significantly different than parameters obtained from a different modeling condition; so comparison between them might be misleading. These results also suggested that one needs to be careful when using constitutive parameters that have been estimated in a specific modeling condition to perform an analysis in a different modeling condition. After showing that Ogden and Fung orthotropic were the most accurate models among the ones considered here for one

representative participant, the best-fit constitutive parameters were evaluated for the remaining 19 participants. A statistical analysis was carried out to highlight potential differences in mechanical properties between sexes and between locations. Male participants were found to have consistently higher initial tissue stiffness than female participants, regardless of constitutive model, at the proximal thigh (E^{Ogd} and E^F) and middle thigh (E^F) location (**Figure 24**). This might be caused by the different compositions of cross-sections between men and women, specifically women were found to have a higher fat content when compared to men [118]. Also, we detected a high location-dependence of constitutive parameters across constitutive models. Specifically, the proximal location showed to be significantly stiffer (higher values of E^{Ogd} and E^F) when compared to the middle and distal location for both men and women (Error! Reference source not found.). F urthermore, the middle location proved to be significantly stiffer when compared to the distal location for both men and women (Error! Reference source not found.). This suggested that the t high tissue increased its compliance moving distally from the buttocks. This result confirmed what have been reported in [119], where soft tissues in the thigh-buttock area were modeled using a linear elastic isotropic material, with four different regions described by four different Young's modulus values, respectively. The material parameters estimated in that study showed a similar stiffening trend across thigh locations as what we have reported here. The sex and location differences on initial stiffness found in the current study employing Ogden and Fung orthotropic constitutive law agreed with a previous study from this same group that used a simplified uniaxial compression model employing Mooney-Rivlin constitutive law to describe the same experimental dataset [106]. The sex and location influences on the constitutive parameters shown above indicated the importance of individual and location specific *in vivo* measurement of biological soft tissue in FE modeling. Furthermore, the present results showed that this modeling approach has

the capability of detecting mechanical differences between groups, in a consistent way, independent of the non-linear model of choice (e.g., Fung or Ogden model). We propose that, in the future, this modeling approach, supported with experimental data, will have the capability of detecting changes in mechanical properties due to other conditions, such ageing or disease.

The current study has some limitations. First, the thigh geometry generation lacked subject-specific data. While we have collected the specific surface geometry for the representative subject, the geometry of the femur and the determination of femur relative position within the thigh were based on literature sources. Furthermore, the FE models of the remaining 19 subjects also lacked surface geometry details, however we ensured that the femur size and its relative position were within anatomically reasonable ranges, and the hip-joint lengths and the middle thigh circumferences of the other 19 subjects were matched to subject-specific data. Second, the thigh soft tissues were modeled by the use of a bulk material, thus, the material parameters were evaluated based on different locations rather than soft tissue types. Having access to a more precise anatomy of the soft tissues within the thigh, possibly through medical imaging, will give us the capability of estimating mechanical properties correlated to specific tissues rather than locations. It has been shown by previous MRI study that the muscle strain is more sensitive to changes in seat support surface and load distribution than strain in subcutaneous fat [120], which could be an important characteristic to validate an anatomically accurate FE model and further increase its predicting capability. This will be the focus of future investigations. Third, the bulk properties of soft tissues in the present study were modeled using isotropic material models, although the mechanical properties of soft tissues (e.g., muscle and skin) have been known to be anisotropic. Due to the lack of multi-axial *in vivo* experimental data and to the choice of modeling the soft tissues as a bulk material, however, using isotropic material models is a reasonable option [115],

[116]. Fourth, the optimization process in this study used the simplex search algorithm (*fminsearch* function in MATLAB). The use of this algorithm was motivated by the fact that it was a derivative-free method. Algorithms like trust-region would require gradient information of the objective function, however the objective function in our study had no analytic expression and performed like a black box: inputs were the material parameters and outputs were the NRMSDs between the FE simulation and experimental data. Due to the lack of analytic expressions, the convexity of the objective function cannot be confirmed, which opened the possibility of the optimized material parameters to be local minima instead of global minima.

In the next chapter, a FE model of the buttock-thigh region with accurate participant-specific overall geometry and subdermal anatomical structure will be developed. Constitutive parameters of different soft tissue type, i.e., muscle, fat, skin will be evaluated.

4. A NONLINEAR HUMAN THIGH MODEL WITH HIGH ANATOMICAL AND MECHANICAL FIDELITY

4.1. Overview

The goal of this chapter is to develop a FE model of the thigh that is accurate in the description of both anatomical details and nonlinear mechanical behaviors. A 3D thigh FE model that contained accurate geometry of muscle, fat, and skin was developed based on the MRI images of a subject. Using the optimization process described in the previous chapter, the best-fit constitutive parameters for each tissue component were obtained to match the compressive force-deflection behavior observed *in vivo*.

4.2. Methods

4.2.1. Mechanical behavior of soft tissues in vivo

Thigh indentation test. Force-deflection data sets from the leg of one subject (male, 26 years old, 185 cm, 185 lb) were collected in our collaborator Dr. Tamara Reid Bush's lab. The indentation test was carried out on the subject's right thigh under a quadruped and a prone posture, respectively. An indenter was manually applied to each of the tested area on the thigh using a constant load rate. Force and deflection measurements were taken via a six-axis load cell and a linear potentiometer, respectively, calibrated to report zero deflection and force when the indenter was flush with the undeformed thigh. Load was applied until a biological barrier was reached. Three locations on the posterior side of the right thigh were tested (i.e., proximal, middle, and distal location).

Skin suction test. Skin mechanical data, collected *in vivo*, were obtained from a previous study [121]. Briefly, to measure the mechanical properties of the skin on the anterior surface of the forearm, Diridollou and colleagues employed a small cylinder device that could create partial

vacuum causing deformation of the skin by suction (**Figure 25 a**). An ultrasound transducer measured the resulting vertical displacement of the skin. The end of the cylinder device was attached to skin using doubled sided adhesive tape and the central aperture, through which the skin was under suction pressure, measured 6 mm in diameter. In this study, we extracted 20 data points from the pressure-displacement curve presented in [121] (**Figure 25 b**) and we employed this mechanical data to inform optimization process and obtain the constitutive parameters for skin.
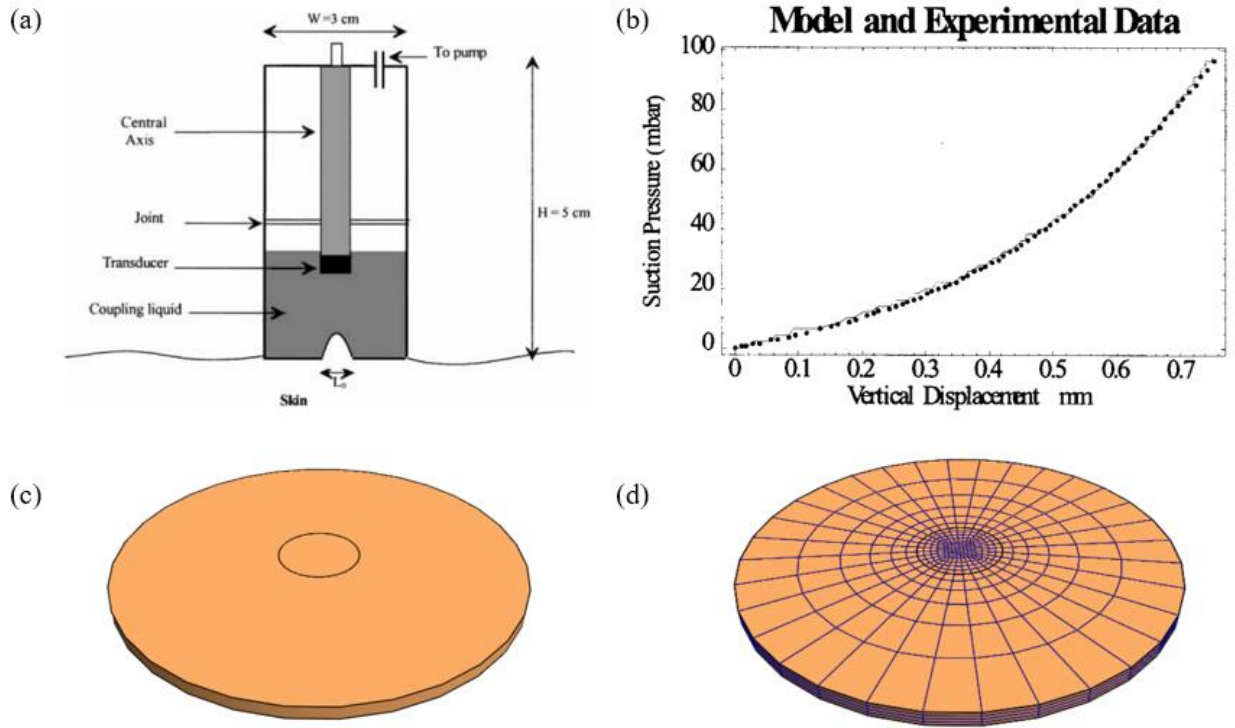
Figure 25. (**a**) A cylinder device that applies suction pressure on skin and measures the displacement of skin by an ultrasound transducer. $L_0 = 6mm$. (**b**) The ascendant part of pressure-displacement data of skin under suction pressure. The solid line represents experimental data, while the dotted line represents theoretical data. (**c**) FEM geometry to reproduce the suction test. The thickness of the skin is 0.95 mm. The diameter of the outer circle is 30 mm, corresponding to the cylinder suction device shown in (**a**) ($w = 30\ mm$). The diameter of the inner circle is 6 mm, corresponding to the aperture size shown in (**a**) ($L_0 = 6\ mm$). (**d**) Mesh of the FEM of the skin. (**a**) and (**b**) are from [121].

4.2.2. Geometry generation

Thigh model. A total of 38 MRI images that ranged from the distal end of the buttock to the proximal end of the patella of the right thigh of the subject were obtained (**Figure 26 a**). Image

processing for tissue isolation was done in Adobe Photoshop CS6. Pixels of individual tissue types were recognized by their different shading values (**Figure 26 b**). The boundary of each tissue types was then traced, smoothed, and exported (**Figure 26 c**). The cross-section boundary lines of all tissues were then stacked in the 3D space in Siemens NX 12.0 to guide the generation of 3D geometry of each tissue type, i.e., fat, muscle, femur (**Figure 26 d**-**f**). Skin layer was added on top of the fat layer in the meshing process.

For the most part, all muscle groups were lumped together into a single section, but eventually the muscle groups separate so much that it was not reasonable to continue lumping them. Toward the distal end of the thigh, it was found that the muscle started splitting from the generally homogenous whole into five separate groups. So, up to this point, the muscle groups were lumped, and after this point the muscle was split into five sections. The split in the geometry occurred at 216 mm from the proximal end of the thigh, where the separation between muscles exceeded 30 pixels (13.45 mm) in diameter. Geometry for the fat and bone were single solids for the entire length of the thigh.

Skin suction model. We developed a skin model that described the experimental setup in [121]. Specifically, to represent the skin area tested, we developed a model of a cylindrical area of the skin with a height of 0.95 mm, corresponding to skin thickness, and an outer diameter of 30 mm, corresponding to the diameter of the cylinder suction device. The diameter of the center circular area was 6 mm, corresponding to the aperture size (**Figure 25 a**).
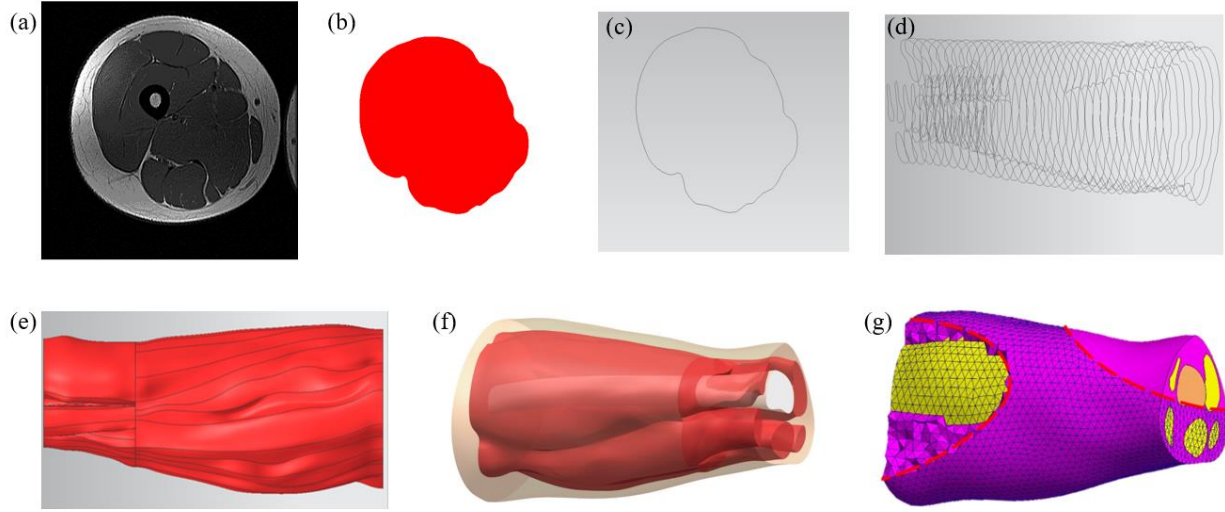
Figure 26. (**a**) A cross-section MRI image of the right thigh of the subject. (**b**) Isolated pixels of the muscle tissues from the cross-section MRI image. Femur geometry will be subtracted from the muscle geometry when the 3D models of femur and muscle are formed. (**c**) Boundary of the muscle tissues recognized from the cross-section muscle tissues. (**d**) Boundary lines of the muscle tissues stacked in the 3D space. (**e**) 3D geometry of the muscle tissues generated from the cross-section boundary lines. (**f**) 3D geometry of the thigh with fat, muscle, and femur. (**g**) Mesh of the thigh 3D geometry.

4.2.3. *Finite element model*

Mesh generation and boundary conditions of the thigh model. Each component of the 3D thigh geometry mentioned above (i.e., fat, muscle, femur) was meshed (HyperMesh ver.13.0) using 10 nodes tetrahedral elements with an average size of 7 mm (**Figure 26 g**). A skin layer mesh was generated on the thigh outer surface using 6 nodes triangular shell elements with thickness of 1.64 mm [122]. The FE model had 63,921 elements and 85,272 nodes. Following the procedure described in chapter **3**, we identified three $50\ mm \times 50\ mm$ areas at the proximal, middle, and distal locations on the posterior side of the thigh, corresponding to the tested regions of the *in vivo* indentation test (**Figure 27 a-c**). Boundary conditions were applied to the femur (i.e., constrained against displacement and rotation in any direction), to the two cut planes at proximal and distal thigh (i.e., nodes were constrained against longitudinal displacements along the femur longitudinal direction), and to the three testing areas (i.e., nodes were restricted to move only in an anterior-posterior direction). Additionally, subject-specific compression forces at each location,

as recorded *in vivo*, were applied to one testing area at a time. Compression forces were applied in 20 evenly spaced steps from zero to the maximum value recorded in the experiment, and the nodal displacements of the compressed area at each step were recorded and averaged. Simulated force-deflection curves were then compared to the experimental data to estimate the best-fit constitutive parameters.

Mesh generation and boundary conditions of the skin suction model. The skin model was meshed (Preview 1.19) using 8 nodes hexahedral elements (**Figure 25 d**). There were 4 layers of elements in the thickness direction. The averaged element size for the center part of the skin under pressure was 0.35 mm. The size of the elements gradually grew when it approached the edge. The FE model has 1536 elements and 2005 nodes. We applied boundary conditions to represent surface suction pressure to the central circular area with diameter of 6 mm, we also constrained displacements and rotations in every direction for the elements in the outer surrounding area of the skin surface, to represent the tied contact with the loading cylinder. The suction pressure was applied in 20 evenly spaced steps from zero to the maximum value of 10 kPa. Simulated press-displacement curves were then compared to the experimental data to estimate the best-fit constitutive parameters.
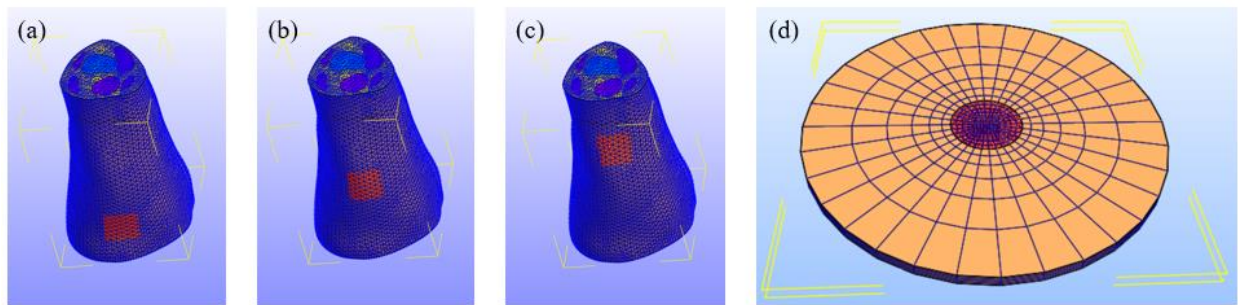
Figure 27. 50 mm × 50 mm indentation test areas at (**a**) proximal thigh, (**b**) middle thigh, and (**c**) distal thigh. (**d**) The central part of skin that is under suction pressure.

4.2.4. Constitutive models and parameter estimation

Constitutive models of fat and muscle. The mechanical behavior of fat and muscle were described by the first order Ogden Model. The strain energy function for fat and muscle were as follows, respectively.

$$\Psi^{fat} = \frac{\mu^{fat}}{\alpha^{fat}} \left(\lambda_1^{\alpha^{fat}} + \lambda_2^{\alpha^{fat}} + \lambda_3^{\alpha^{fat}} - 3 \right) + \frac{1}{2} K^{fat} (\ln J)^2, \tag{18}$$

$$\Psi^{musle} = \frac{\mu^{muscle}}{\alpha^{muscle}} \left(\lambda_1^{\alpha^{muscle}} + \lambda_2^{\alpha^{muscle}} + \lambda_3^{\alpha^{muslce}} - 3 \right) + \frac{1}{2} K^{muscle} (\ln J)^2, \tag{19}$$

where the meaning of each parameter is the same as explained in section **3.2.4.**

Constitutive model of skin. The mechanical behavior of skin was described by the Gasser-Ogden-Holzapfel (GOH) model [50], which was a solid mixture model that applied to incompressible solids with two preferred directions aligned along the unit vector α_1 and α_2. The strain energy function of skin was written as,

$$\Psi^{skin} = c^{gm}(I_\mathbf{C} - 3) + \sum_{i=1,2} \frac{c_1^{(k)}}{2c_2^{(k)}} \left\{ e^{c_2^{(k)}[tr(\mathbf{H}_i\mathbf{C})-1]^2} - 1 \right\} + \frac{1}{2} K^{skin} (\ln J)^2, \tag{20}$$

where c^{gm} was a constitutive parameter with the dimension of a stress, $I_\mathbf{C}$, J and $\mathbf{C}$ were as described in **Equation (9)**, $c_1^{(k)}$ was a constitutive parameter with the dimension of a stress, and $c_2^{(k)}$ was a dimensionless constitutive parameter. $\mathbf{H}_i$ was the structure tensor described as,

$$\mathbf{H}_i = \kappa_i \mathbf{I} + (1 - 3\kappa_i) \, \alpha_1 \otimes \alpha_2 \tag{21}$$

where κ_i was the dispersion factors from the normalized π-periodic von Mises distribution, α_i was the preferred fiber direction of collagen family i (**Figure 28 a**), and **I** was the identity tensor. We considered two collagen fiber families in this constitutive model. The dispersion of each collagen family followed the normalized π-periodic von Mises distribution [38]. The two collagen families were assumed to share the same constitutive parameters, i.e., $c_1^{(1)} = c_1^{(2)} = c_1$, $c_2^{(1)} = c_2^{(2)} = c_2$,

$\kappa_1 = \kappa_2 = \kappa$. The bulk modulus-like penalty parameter K^{skin} was defined as $K^{skin} = 100 \times (c^{gm} + 2c_1)$ to enforce incompressibility.
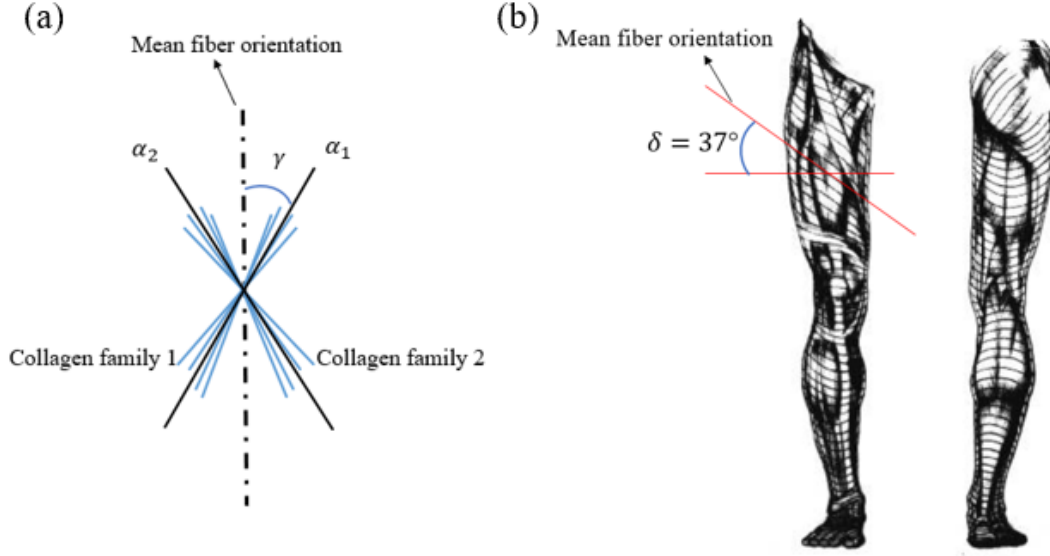
Figure 28. (**a**) Structure of two crossing collagen fiber families, where α_1 and α_2 represent the preferred collagen fiber directions of collagen family 1 and 2, respectively. The bisector of the direction α_1 and direction α_2 is defined as the preferred fiber orientation of the skin, and γ is the angle between the direction α_i and the preferred fiber orientation of skin. (**b**) The wrinkle line of the human leg that indicates the mean fiber direction. At the anterior side of the thigh, wrinkle lines run ~37° with respect to the circumferential direction. At the posterior side of the thigh, wrinkle lines run in transverse direction. Around the knee area, wrinkle lines run in transverse direction. (**b**) is from [57].

Preferred fiber orientation of skin. The wrinkle lines [57] (**Figure 28 b**) were used to determine the preferred fiber orientation vector for each skin element. As described by Kraissl in his original paper, the wrinkle line pattern was "generally oblique" at the anterior thigh, and "generally transverse" at the posterior aspect. The angle of wrinkle line direction with respect to transverse direction was measured as $\delta = 37°$ (ImageJ). For posterior aspect of the thigh and knee area, $\delta = 0°$. In the FE model, the preferred fiber orientation vectors were calculated for each skin element individually. Together with the angle γ, the preferred direction of each collagen family could be determined for each skin element (**Figure 29**). In the skin suction model, however, the preferred fiber orientation vectors of all elements were set in the same direction within the skin

surface plane since the represented skin area in the model is small (i.e., 30 mm in diameter). We assumed that the preferred fiber orientation of skin does not vary in such a small area.
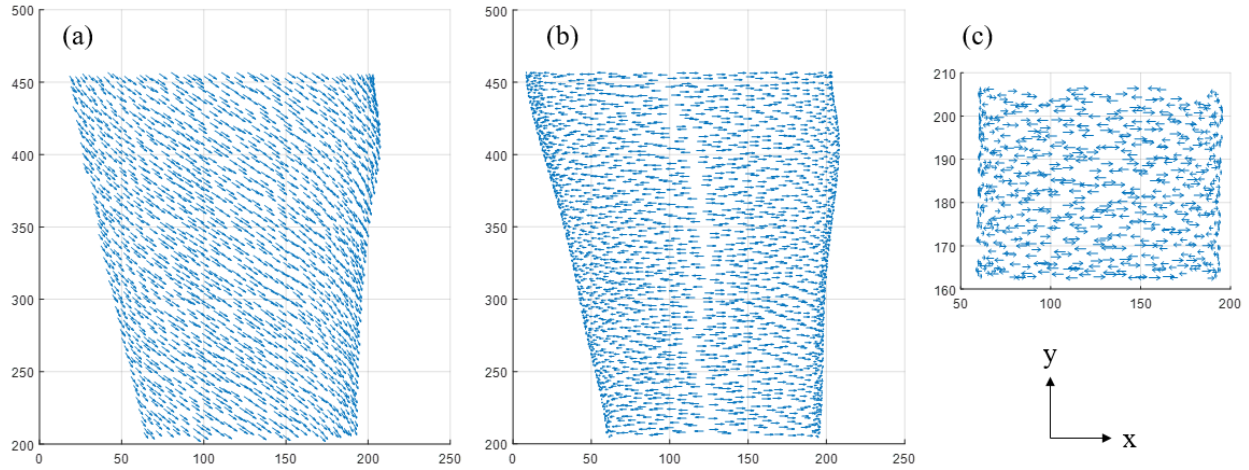
Figure 29. Preferred fiber orientation vector of each skin shell element at (**a**) anterior side of the thigh, (**b**) posterior side of the thigh, (**c**) knee area.

4.2.5. *Parameter estimation*

Best-fit constitutive parameters for fat and muscle. We estimated the best-fit constitutive parameters for fat and muscle using the thigh FE model without the skin layer. The FE model depended on four constitutive parameters (i.e., μ^{fat}, α^{fat}, μ^{muscle}, and α^{muscle}). They were determined in the optimization process, employing the simplex search method implemented in MATLAB (i.e., function *fminsearch*). The objective function to be minimized was described by **Equation (16), (17)**. The optimization iterations would stop if one of the two following stopping criteria was met: (1) the solver attempted to take a step that was smaller than $TolX$, which was set to be $TolX = 0.01$, and the change in the value of the objective function during a step was smaller than $TolFun$, which was set to be $TolFun = 0.01$; (2) the objective function value was smaller than the threshold, which was set to be $e_{threshold} = 0.15$. The initial guess values for the parameters to start the parameter estimation process were set to be $\mu^{muscle} = 1.91\ KPa$,

76

$\alpha^{muscle} = 4.6$, $\mu^{fat} = 1.17 \, KPa$, $\mu^{fat} = 16.2$ [28]. The best-fit constitutive parameters for fat and muscle were determined using the *in vivo* force-deflection data collected in quadruped and prone posture, respectively.

Skin constitutive parameters. The skin constitutive parameters *in vivo* were evaluated using the skin suction FE model and the *in vivo* data shown in **Figure 25 b**. The skin suction model had five constitutive parameters in total. Two of them (i.e., $\gamma = 41°$, $\kappa = 0.15$) were structural parameters informed by literature [38]. Three of them (i.e., c^{gm}, c_1, c_2) were determined in the optimization process, employing the simplex search method mentioned above. The FE simulation, in each optimization iteration, was performed in FEBio. The objective function to be minimized was described by

$$e = \frac{\sqrt{\frac{\sum_{i=1}^{n}(d^{FE} - d^{EXP})_i^2}{n}}}{(d^{EXP})_{max}} \tag{22}$$

where n was the number of loading steps (i.e., $n = 20$), d^{FE} and d^{EXP} were the displacement values of the central location of skin under pressure from the FE simulation and experimental measurement, respectively, and $(d^{EXP})_{max}$ represented the maximum experimental values of displacement (i.e., the displacement measurement for the maximum pressure). The optimization iterations would stop if one of the two following stopping criteria was met: (1) the solver attempted to take a step that was smaller than $TolX$, which was set to be $TolX = 0.001$, and the change in the value of the objective function during a step was smaller than $TolFun$, which was set to be $TolFun = 0.001$; (2) the objective function value was smaller than the threshold, which was set to be $e_{threshold} = 0.02$. The initial guess values to start the parameter estimation process were set to be $c^{gm} = 50 \, KPa$, $c_1 = 50 \, KPa$, $c_2 = 5$.

Effect of in vitro and in vivo skin constitutive parameters on thigh mechanical behavior. The effect of *in vitro* vs. *in vivo* skin constitutive parameters on the overall thigh FE model mechanical behavior during the indentation test was investigated using the thigh model with the skin layer. The skin structure parameters (i.e., κ, γ, δ) were informed by literature [38], [57], and the parameters for fat and muscles (μ^{fat}, α^{fat}, μ^{muscle}, and α^{muscle}) were the best-fit constitutive parameters obtained from the parameter estimation process matching the *in vivo* indentation test data as mentioned in the beginning of this section. Then the mechanical behavior of the thigh model with *in vitro* skin constitutive parameters (i.e., c^{gm}, c_1, c_2), which were extracted from [38], was compared to that of the thigh model with *in vivo* skin constitutive parameters, which was obtained from the skin suction model parameter estimation process informed by *in vivo* data mentioned above. The difference was evaluated using,

$$NRMSD = NRMSD_{prx} + NRMSD_{mid} + NRMSD_{dis}, \tag{23}$$

where $NRMSD_{prx}$, $NRMSD_{mid}$, and $NRMSD_{dis}$ were normalized root-mean-square deviation (NRMSD) estimated at each location α as

$$NRMSD_\alpha = \frac{\sqrt{\frac{\sum_{i=1}^{n}(d_\alpha^{(in\ vivo)} - d_\alpha^{(in\ vitro)})_i^2}{n}}}{\left(d_\alpha^{(in\ vivo)}\right)_{max}} \tag{24}$$

where n was the number of loading steps (i.e., $n = 20$), $d_\alpha^{(in\ vivo)}$ and $d_\alpha^{(in\ vitro)}$ were the deflection values for the α location from the thigh model with *in vivo* skin constitutive parameters and the thigh model with *in vitro* skin constitutive parameters, respectively, and $\left(d_\alpha^{(in\ vivo)}\right)_{max}$ represented the maximum experimental values of deflection for each location α (i.e., the deflection measurement for the maximum load).

4.3. Results

4.3.1. Best-fit constitutive parameters for fat and muscle

The best-fit constitutive parameters for fat and muscle tissues matching the *in vivo* indentation test data in quadruped and prone postures were obtained using the thigh FE model without the skin layer. The best-fit constitutive parameters were listed in **Table 7**. The *in vivo* indentation test data were represented by red markers in **Figure 30 a-b** (i.e., dotted markers for proximal thigh, circular markers for middle thigh, and cross markers for distal thigh). The force-deflection behavior of FE simulation with best-fit constitutive parameters were represented by lines (i.e., solid line for proximal thigh, dashed line for middle thigh, and dahs-dotted line for distal thigh). The normalized RMSD between FE simulation and *in vivo* indentation test data are right below 15% for both quadruped posture and prone posture, as shown in **Table 7**.
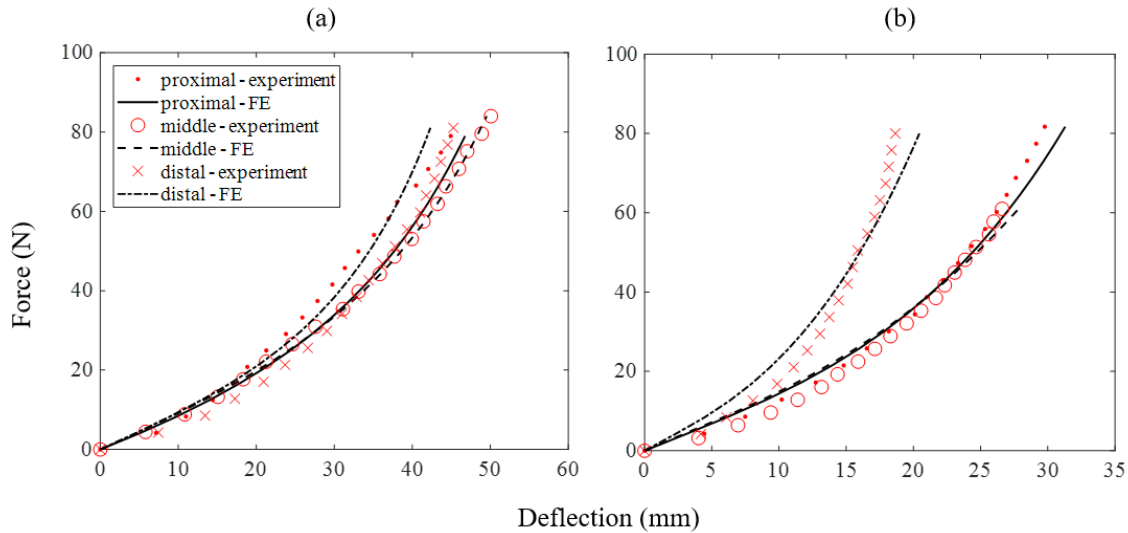
Figure 30. (**a**) Force-deflection behavior of thigh soft tissue from *in vivo* indentation data in quadruped posture and the FE simulation. (**b**) Force-deflection behavior of thigh soft tissue from *in vivo* indentation data in prone posture and the FE simulation.

Table 7. Best-fit constitutive parameters for fat and muscle tissues that describe the *in vivo* indentation test data collected in quadruped and prone postures.

Testing posture of *in vivo* data	μ^{msucle}	α^{muscle}	μ^{fat}	α^{fat}	Total NRMSD
Quadruped	1.80 kPa	5.75	0.36 kPa	8.43	15.0%
Prone	0.26 kPa	9.91	3.13 kPa	53.97	14.9%

4.3.2. Skin constitutive parameters in vivo

The best-fit constitutive parameters for the *in vivo* skin suction test, obtained through the parameter estimation process, were $c^{gm} = 7.6\ kPa$, $c_1 = 135.5\ kPa$, $c_2 = 18.4$. **Figure 31 a** showed the displacement contour map of the tested skin area under the maximum suction pressure of $10\ kPa$. **Figure 31 b** showed the pressure-displacement curve of the central point of tested area during the suction pressure load, for both *in vivo* data (represented by circular markers) and FE simulation data (represented by solid line). The normalized RMSD between *in vivo* data and FE simulation was 1.15%.
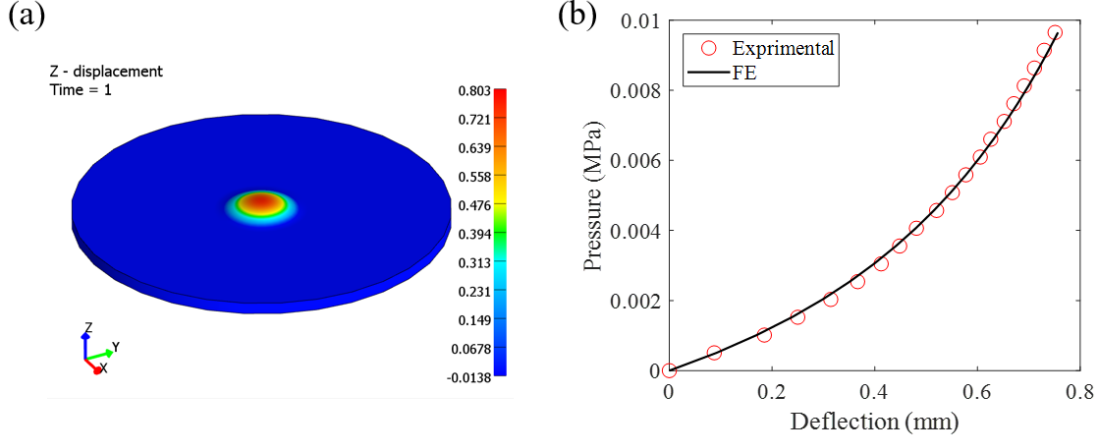
Figure 31. (**a**) Displacement contour map of the skin suction model with best-fit constitutive parameters with maximum pressure load. The displacement unit in the figure is millimeter. (**b**) Pressure-displacement curves of experimental data collected *in vivo* and FE simulation data with best-fit constitutive parameters.

4.3.3. Effect of in vitro and in vivo skin constitutive parameters on thigh mechanical behavior

The force-deflection behavior of thigh FE model with *in vitro* and *in vivo* skin constitutive parameters were compared to that of the thigh *in vivo* indentation test data. The best-fit constitutive

parameters for fat and muscle obtained for quadruped posture in section *4.3.1* were applied to the thigh models. In **Figure 32 a**-**b**, the *in vivo* indentation test data were represented by red markers, specifically dotted markers for proximal thigh, circular markers for middle thigh, and cross markers for distal thigh. In addition, the force-deflection behavior of FE simulation were represented by lines, specifically solid line for proximal thigh, dashed line for middle thigh, and dahs-dotted line for distal thigh. **Figure 31 a** showed model results for the FE model of the thigh employing *in vitro* skin parameters, and **Figure 31 b** showed model results for the FE model of the thigh employing *in vivo* skin parameters (**Table 8**). The normalized RMSD between FE simulation and *in vivo* indentation test data collected in the quadruped posture are shown in **Table 8**.
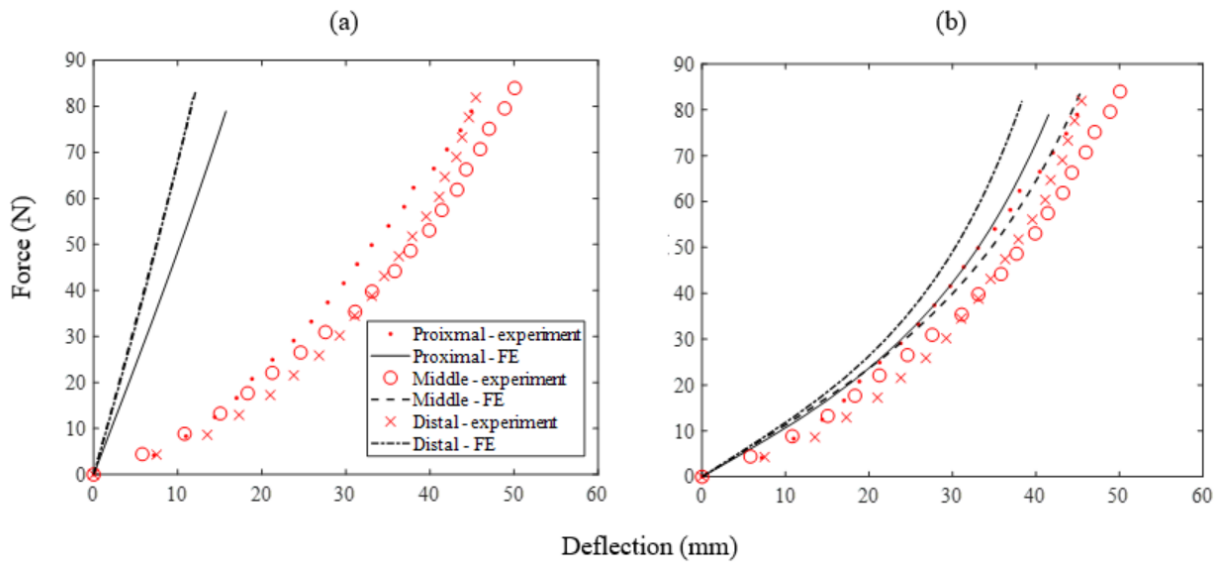
Figure 32. Force-deflection behavior of thigh soft tissue collected from *in vivo* indentation test and FE simulation. The *in vivo* force-deflection curve in (**a**) and (**b**) are the same data from the quadruped posture. The FE simulated force-deflection curves in (**a**) are from thigh FE model with *in vitro* skin constitutive parameters. The FE simulated force-deflection curves in (**b**) are from thigh FE model with *in vivo* skin constitutive parameters.

Table 8. The constitutive parameters of the thigh FE model with *in vitro* skin constitutive model and the thigh FE model with *in vivo* skin constitutive model. The NRMSD values show the normalized root-mean-square deviations between the FE simulated force-deflection curve and the *in vivo* indentation data collected in quadruped posture.

	Thigh FE model with *in vitro* skin constitutive model	Thigh FE model with *in vivo* skin constitutive model
NRMSD	157.75%	25.69%
c^{gm}	100.7 kPa	7.6 kPa
c_1	24530 kPa	135.5 kPa
c_2	0.1327	18.4
γ	41°	
κ	0.15	
μ^{muscle}	1.80 kPa	
α^{muscle}	5.57	
μ^{fat}	0.36 kPa	
α^{fat}	8.43	

4.4. Discussion and conclusions

Previous studies that modeled thigh-buttock area soft tissue mechanical behaviors either modeled the bulk properties of all soft tissues (i.e., skin, fat, muscle) together [21], [27], or modeled skin and fat as one component [19], [28]. The only few studies that modeled the skin separately used simple phenomenological constitutive models [16], [20]. In this study, we constructed a thigh model with an added skin layer and included the collagen fiber structure in the skin layer to account for the nonlinear and anisotropic behavior of skin. The use of a location-specific continuous fiber distribution to model the skin layer, resulted in a significantly high computational cost. The FE simulation of each set of constitutive parameters took more than 3 hours, and usually hundreds of sets of constitutive parameters needed to be evaluated to obtain the best-fit results. To keep the computational time to a reasonable length was important in the framework of this study. In fact, an excessively high computational cost would prevent this model to be used in a clinical setting. With this goal in mind, first we performed the parameter estimation

for fat and muscle constitutive parameters only, employing the subject specific FE model with no skin layer, and then we quantified the effect of introducing a skin layer with material parameters estimated from *in vivo* and *in vitro* data collected separately.

Although our FE model was intended to simulate the thigh-buttock area while seated, indentation tests could be difficult while in the seated posture, especially for people with disabilities. Thus, a quadruped and a prone posture were adopted for indentation tests. The quadruped posture had the same hip and knee flexion as the seated posture, while the prone posture closely resembles the supine position in which MRI images were taken. The best-fit constitutive parameters obtained from different *in vivo* posture differed significantly (e.g., μ^{fat} and α^{fat} obtained from prone posture data were more than 8 and 6 times of those obtained from quadruped posture data, respectively). We propose that the different reference configurations of soft tissues in the FE model and *in vivo* indentation tests could be a contributing factor. The thigh FE model was developed based on MRI images taken in supine posture, while the indentation test was taken in quadruped and prone posture. The hip and knee flexion would change the reference configuration of soft tissues for different postures, which was not represented correspondingly in the FE model. This could potentially be solved by building the FE model using MRI images taken at the same posture in which *in vivo* data were collected. However, the lack of data of a fully relaxed configuration for all soft tissues could still lead to discrepancy in best-fit constitutive parameters that match *in vivo* data collected in different postures. Our best-fit constitutive parameters of fat and muscle for *in vivo* data of different postures strongly suggested the importance of the proper reference configuration for FE model development and *in vivo* data collection. It is common for simulation studies to extract constitutive parameters from literature to apply to the FE model directly [20], [21]. However, soft tissues tested in different environment

(i.e., *in vivo* vs. *in vitro)* exhibit very different mechanical properties [38], [121]. The GOH model adopted in this chapter for skin mechanical properties was also used in [38], which obtained the best-fit GOH model parameters for human back skin samples tested *in vitro*. However, when these constitutive parameters were applied to the skin layer of the thigh model presented here, along with the best-fit *in vivo* constitutive parameters for fat and muscle, the FE model output differed from *in vivo* indentation test drastically (**Figure 32 a**), with normalized RMSD being 157.75%. For this reason, we developed a skin FE model (**Figure 27 d**) to search for constitutive parameters of skin that match *in vivo* experimental data. Pressure suction, as an important means for *in vivo* skin mechanical properties testing [121], [123], [124], was chosen as the source of *in vivo* data. The best-fit constitutive parameters for skin estimated from *in vivo* data, differed from those estimated from *in vitro* data of several orders of magnitude, as shown in **Table 8**. When the constitutive parameters for skin estimated from the skin suction model were used to the thigh FE model, along with same *in vivo* constitutive parameters for fat and muscle used previously, the difference between FE model output and *in vivo* data from indentation test dropped to a relative low level (**Figure 32 b**), with normalized RMSD being 25.69%. Our results here show that (1) the skin layer has significant contribution to the thigh mechanical properties, and (2) *in vitro* skin constitutive parameters might not be suitable to model soft tissue mechanical behavior *in vivo*.

As to the limitations of the current study, the interface interaction between different soft tissues were not counted in current FE model. The deep fascia that separated muscles into different fascia compartments and allowed relative movement between muscle-bone interface [125] were not described in current model. Another known relative movement that could happen at the soft tissue interface is between skin layer and the underlying fascia, which has been shown by ultrasound transducer during skin suction test [121]. However, *in vivo* data regarding the interface

movement (i.e., friction coefficients, relative movement limits) are still rare in literature. The expensive computational cost of friction contact in the FE model could also make solutions for parameter estimation process hard to achieve. In addition, it should be noted that best-fit constitutive parameters obtained for both the skin suction model and the thigh indentation model were not the sole solutions to describe the *in vivo* experimental data. The first factor affecting the solution values was the stopping criteria of the parameter estimation process (i.e., $TolX$, $TolFun$, and $e_{threshold}$ in section *4.2.5*). We chose the stopping criteria in consideration of both accuracy (i.e., difference between simulation output and *in vivo* data) and computational cost (i.e., calculating time). Different stopping criteria could lead to different sets of constitutive parameters. Even the stopping criteria was the same, different initial guesses or fitting approach might lead to different best-fit solutions. For instance, in a different parameter estimation approach for the skin suction model, the c_2 value was fixed at 0.1327 [38], with initial guess $c^{gm} = 50\ KPa$, $c_1 = 50\ KPa$ and the same stopping criteria as mentioned in section *4.2.5*. The resulting best-fit values were $c^{gm} = 0.6\ KPa$, $c_1 = 0.1981\ KPa$. This meant the following two sets of parameters: $c^{gm} = 0.6\ KPa$, $c_1 = 198.1\ KPa$, $c_2 = 0.1327$ and $c^{gm} = 7.6\ KPa$, $c_1 = 135.5\ KPa$, $c_2 = 18.40$ are deemed to represent the same pressure-displacement behavior in the current skin suction model setup. More data that describe ground matrix properties (i.e., c^{gm}) and collagen properties (i.e., c_1, c_2) separately could help identify the unique solution. With the current available *in vivo* data for skin suction model and thigh indentation model, no alternative solutions, if found, can be rejected.

5. CONCLUSIONS AND FUTURE WORK

This research was aimed at proposing a finite element modeling approach that can accurately describe the nonlinear mechanical behavior of soft tissues in thigh-buttock area, so that the stress/strain distribution within soft tissue can be described precisely for a better understanding of pressure ulcers formation mechanism.

First, we conducted a comprehensive investigation of skin biomechanics using rat skin samples. Differences in mechanical properties between the upper and lower back, and the axial and transverse direction were detected. The collagen network structure was quantified through automated image analysis routines and manual measurements from histology images. Results showed that: (1) Collagen fiber bundles on the back of rats distributed about two predominate oblique-crossed directions: $\pm 40°\sim 50°$ to spine. (2) Collagen content of skin at the lower back was higher than the upper back, with $56.6\% \pm 10.2\%$ vs. $70.0\% \pm 15.1\%$. A microstructurally based constitutive model that described the nonlinear, anisotropic mechanical behavior of skin was proposed and showed good agreement with experimental data. This study contributed valuable primary data to the skin mechanics research community and contributed to improved understanding of variation and similarities in skin mechanical properties across different species.

Second, we looked into finite element modeling parameter estimation regarding non-linear mechanical behavior of human thigh soft tissues. We proposed an optimization process that addressed the non-linear characteristic of *in vivo* force-deflection data, which has been neglected in the literature. For the first time, we compared the ability of four widely used constitutive models in describing soft tissue non-linear behavior. Results showed that first order Ogden and Fung orthotropic model were more suitable to describe the nonlinear mechanical behavior of soft tissues, compared to neo-Hookean and Mooney-Rivlin model. Also, for the first time in literature, we investigated the effect of the choice of modeling region dimension (3D vs. semi-3D). Results

86

showed that the mechanical properties between 3D and semi-3D model differed significantly. Therefore, semi-3D FE models were not recommend for soft tissues modeling. We also reported constitutive parameter range for Ogden and Fung orthotropic models based on *in vivo* force-deflection data for 20 participants. This study provided deep insights and reliable data for researchers interested in non-linear mechanical behavior of human soft tissues.

In the last chapter, we focused on the *in vivo* mechanical properties of different soft tissue groups. We developed a human thigh model with detailed geometric details using MRI images. A state-of-the-art FE model of skin layer was created and the best-fit constitutive parameters were obtained using *in vivo* data in literature. Fat and muscle mechanical behavior were described using first order Ogden model and best-fit constitutive parameters were obtained using subject-specific *in vivo* experimental data collected in different postures (i.e. quadruped and prone posture). Results showed that testing postures in which *in vivo* data were collected could affect the constitutive parameters of soft tissues. By comparing the force-deflection behavior of the thigh model with *in vitro* and *in vivo* skin constitutive parameters, we concluded that (1) the skin layer had significant contribution to the thigh mechanical properties, and (2) *in vitro* skin constitutive parameters might not be suitable to model soft tissue mechanical behavior *in vivo*.

Future work will focus on (1) modification/simplification of skin FE model to achieve shorter solving time, (2) stress/strain field within soft tissues introduced by sitting action, with consideration of the sitting interface condition (i.e., friction, sitting surface contours), and (3) the interaction/relative movement between different soft tissue groups.

BIBLIOGRAPHY

BIBLIOGRAPHY

[1] A. Gefen, "How much time does it take to get a pressure ulcer? Integrated evidence from human, animal, and in vitro studies," *Ostomy Wound Manage*, vol. 54, no. 10, pp. 26–8, 30–5, Oct. 2008.

[2] M. Reddy, S. S. Gill, and P. A. Rochon, "Preventing Pressure Ulcers: A Systematic Review," *JAMA*, vol. 296, no. 8, pp. 974–984, Aug. 2006.

[3] GBD 2013 Mortality and Causes of Death Collaborators, "Global, regional, and national age-sex specific all-cause and cause-specific mortality for 240 causes of death, 1990-2013: a systematic analysis for the Global Burden of Disease Study 2013," *Lancet*, vol. 385, no. 9963, pp. 117–171, Jan. 2015.

[4] C. Nordqvist, "Bed sores or pressure sores: What you need to know," *Medical News Today*, Dec-2017. [Online]. Available: https://www.medicalnewstoday.com/articles/173972.php. [Accessed: 10-Apr-2018].

[5] T. J. Ryan, "Cellular Responses to Tissue Distortion," in *Pressure Sores - Clinical Practice and Scientific Approach*, Palgrave, London, 1990, pp. 141–152.

[6] N. P. Reddy, G. V. B. Cochran, and T. A. Krouskop, "Interstitial fluid flow as a factor in decubitus ulcer formation," *Journal of Biomechanics*, vol. 14, no. 12, pp. 879–881, Jan. 1981.

[7] E. C. Herrman, C. F. Knapp, J. C. Donofrio, and R. Salcido, "Skin perfusion responses to surface pressure-induced ischemia: Implication for the developing pressure ulcer," *Journal of Rehabilitation Research and Development; Washington*, vol. 36, no. 2, pp. 109–20, Apr. 1999.

[8] R. K. Daniel, D. L. Priest, and D. C. Wheatley, "Etiologic factors in pressure sores: an experimental model.," *Arch Phys Med Rehabil*, vol. 62, no. 10, pp. 492–498, Oct. 1981.

[9] C. V. Bouten, C. W. Oomens, F. P. Baaijens, and D. L. Bader, "The etiology of pressure ulcers: Skin deep or muscle bound?," *Archives of Physical Medicine and Rehabilitation*, vol. 84, no. 4, pp. 616–619, Apr. 2003.

[10] A. A. Manorama, S. Baek, J. Vorro, A. Sikorskii, and T. R. Bush, "Blood perfusion and transcutaneous oxygen level characterizations in human skin with changes in normal and shear loads — Implications for pressure ulcer formation," *Clinical Biomechanics*, vol. 25, no. 8, pp. 823–828, Oct. 2010.

[11] A. Manorama, R. Meyer, R. Wiseman, and T. R. Bush, "Quantifying the effects of external shear loads on arterial and venous blood flow: Implications for pressure ulcer development," *Clinical Biomechanics*, vol. 28, no. 5, pp. 574–578, Jun. 2013.

[12] J. B. Reuler and T. G. Cooney, "The pressure sore: pathophysiology and principles of management," *Annals of Internal Medicine*, vol. 94, no. 5, pp. 661–666, 1981.

[13] D. M. Brienza, P. E. Karg, M. Jo Geyer, S. Kelsey, and E. Trefler, "The relationship between pressure ulcer incidence and buttock-seat cushion interface pressure in at-risk elderly wheelchair users," *Archives of Physical Medicine and Rehabilitation*, vol. 82, no. 4, pp. 529–533, Apr. 2001.

[14] J. Fletcher, "Pressure-relieving equipment: criteria and selection," *Br J Nurs*, vol. 6, no. 6, pp. 323–328, Mar. 1997.

[15] E. Linder-Ganz and A. Gefen, "Mechanical compression-induced pressure sores in rat hindlimb: muscle stiffness, histology, and computational models," *Journal of Applied Physiology*, vol. 96, no. 6, pp. 2034–2049, Jun. 2004.

[16] C. W. J. Oomens, O. F. J. T. Bressers, E. M. H. Bosboom, C. V. C. Bouten, and D. L. Bader, "Can Loaded Interface Characteristics Influence Strain Distributions in Muscle Adjacent to Bony Prominences?," *Computer Methods in Biomechanics and Biomedical Engineering*, vol. 6, no. 3, pp. 171–180, Jun. 2003.

[17] D. L. Bader and F. P. Baaijens, "A theoretical analysis of damage evolution in skeletal muscle tissue with reference to pressure ulcer development," 2003.

[18] M. Makhsous and F. Lin, "A Finite-Element Biomechanical Model for Evaluating Buttock Tissue Loads in Seated Individuals with Spinal Cord Injury," *Bioengineering Research of Chronic Wounds*, pp. 181–205, 2009.

[19] E. Linder-Ganz, N. Shabshin, Y. Itzchak, and A. Gefen, "Assessment of mechanical conditions in sub-dermal tissues during sitting: A combined experimental-MRI and finite element approach," *Journal of Biomechanics*, vol. 40, no. 7, pp. 1443–1454, 2007.

[20] M. Makhsous, D. Lim, R. Hendrix, J. Bankard, W. Z. Rymer, and F. Lin, "Finite Element Analysis for Evaluation of Pressure Ulcer on the Buttock: Development and Validation," *IEEE Transactions on Neural Systems and Rehabilitation Engineering*, vol. 15, no. 4, pp. 517–525, Dec. 2007.

[21] M. M. Verver, J. van Hoof, C. W. J. Oomens, J. S. H. M. Wismans, and F. P. T. Baaijens, "A Finite Element Model of the Human Buttocks for Prediction of Seat Pressure Distributions," *Computer Methods in Biomechanics and Biomedical Engineering*, vol. 7, no. 4, pp. 193–203, Aug. 2004.

[22] D. Brienza *et al.*, "A Randomized Clinical Trial on Preventing Pressure Ulcers with Wheelchair Seat Cushions," *Journal of the American Geriatrics Society*, vol. 58, no. 12, pp. 2308–2314, Dec. 2010.

[23] G. N. Healy, C. E. Matthews, D. W. Dunstan, E. A. H. Winkler, and N. Owen, "Sedentary time and cardio-metabolic biomarkers in US adults: NHANES 2003–06," *Eur Heart J*, vol. 32, no. 5, pp. 590–597, Mar. 2011.

[24] B. G. Raijmakers, M. G. Nieuwenhuizen, H. Beckerman, and S. de Groot, "Differences in the Course of Daily Activity Level Between Persons with and Without Chronic Pain:," *American Journal of Physical Medicine & Rehabilitation*, vol. 94, no. 2, pp. 101–113, Feb. 2015.

[25] A. V. Rowlands *et al.*, "Assessing sedentary behavior with the GENEActiv: introducing the sedentary sphere.," Jun. 2014.

[26] J. E. Grey, K. G. Harding, and S. Enoch, "Pressure ulcers," *BMJ*, vol. 332, no. 7539, pp. 472–475, Feb. 2006.

[27] R. Ragan, T. W. Kernozek, M. Bidar, and J. W. Matheson, "Seat-interface pressures on various thicknesses of foam wheelchair cushions: A finite modeling approach," *Archives of Physical Medicine and Rehabilitation*, vol. 83, no. 6, pp. 872–875, Jun. 2002.

[28] R. M. A. Al-Dirini, M. P. Reed, J. Hu, and D. Thewlis, "Development and Validation of a High Anatomical Fidelity FE Model for the Buttock and Thigh of a Seated Individual," *Ann Biomed Eng*, vol. 44, no. 9, pp. 2805–2816, Sep. 2016.

[29] G. A. Holzapfel, "Biomechanics of soft tissue," *The handbook of materials behavior models*, vol. 3, pp. 1049–1063, 2001.

[30] T. Husain, "An experimental study of some pressure effects on tissues, with reference to the bed-sore problem," *The Journal of Pathology and Bacteriology*, vol. 66, no. 2, pp. 347–358, Oct. 1953.

[31] I. A. Brown, "A scanning electron microscope study of the effects of uniaxial tension on human skin," *British Journal of Dermatology*, vol. 89, no. 4, pp. 383–393, Oct. 1973.

[32] R. Reihsner, B. Balogh, and E. J. Menzel, "Two-dimensional elastic properties of human skin in terms of an incremental model at the in vivo configuration," *Medical Engineering & Physics*, vol. 17, no. 4, pp. 304–313, Jun. 1995.

[33] F. Xu and T. Lu, *Introduction to Skin Biothermomechanics and Thermal Pain*. Berlin, Heidelberg: Springer Berlin Heidelberg, 2011.

[34] B. Finlay, "Scanning electron microscopy of the human dermis under uni-axial strain," *Biomedical engineering*, vol. 4, no. 7, pp. 322–327, 1969.

[35] P. P. van Zuijlen *et al.*, "Morphometry of dermal collagen orientation by Fourier analysis is superior to multi-observer assessment," *J. Pathol.*, vol. 198, no. 3, pp. 284–291, Nov. 2002.

[36] H. J. C. de Vries, D. N. H. Enomoto, J. van Marle, P. P. M. van Zuijlen, J. R. Mekkes, and J. D. Bos, "Dermal Organization in Scleroderma: The Fast Fourier Transform and the Laser Scatter Method Objectify Fibrosis in Nonlesional as well as Lesional Skin," *Laboratory Investigation*, vol. 80, no. 8, pp. 1281–1289, Aug. 2000.

[37] J. W. Y. Jor, P. M. F. Nielsen, M. P. Nash, and P. J. Hunter, "Modelling collagen fibre orientation in porcine skin based upon confocal laser scanning microscopy," *Skin Research and Technology*, vol. 17, no. 2, pp. 149–159, May 2011.

[38] A. Ní Annaidh *et al.*, "Automated Estimation of Collagen Fibre Dispersion in the Dermis and its Contribution to the Anisotropic Behaviour of Skin," *Ann Biomed Eng*, vol. 40, no. 8, pp. 1666–1678, Mar. 2012.

[39] H. Alexander and T. H. Cook, "Accounting for Natural Tension in the Mechanical Testing of Human Skin," *J Investig Dermatol*, vol. 69, no. 3, pp. 310–314, Sep. 1977.

[40] R. B. Groves, S. A. Coulman, J. C. Birchall, and S. L. Evans, "An anisotropic, hyperelastic model for skin: Experimental measurements, finite element modelling and identification of parameters for human and murine skin," *Journal of the Mechanical Behavior of Biomedical Materials*, vol. 18, pp. 167–180, Feb. 2013.

[41] A. Karimi, S. M. Rahmati, and M. Navidbakhsh, "Mechanical characterization of the rat and mice skin tissues using histostructural and uniaxial data," *Bioengineered*, vol. 6, no. 3, pp. 153–160, May 2015.

[42] Y. Lanir, "A structural theory for the homogeneous biaxial stress-strain relationships in flat collagenous tissues," *Journal of Biomechanics*, vol. 12, no. 6, pp. 423–436, Jan. 1979.

[43] Y. T. Lanir, "Constitutive equations for fibrous connective tissues," *Journal of biomechanics*, vol. 16, no. 1, pp. 1–12, 1983.

[44] P. Tong and Y.-C. Fung, "The stress-strain relationship for the skin," *Journal of Biomechanics*, vol. 9, no. 10, pp. 649–657, 1976.

[45] D. R. Veronda and R. A. Westmann, "Mechanical characterization of skin—Finite deformations," *Journal of Biomechanics*, vol. 3, no. 1, pp. 111–124, Jan. 1970.

[46] M. Comninou and I. V. Yannas, "Dependence of stress-strain nonlinearity of connective tissues on the geometry of collagen fibres," *Journal of Biomechanics*, vol. 9, no. 7, pp. 427–433, Jan. 1976.

[47] J. W. Y. Jor, M. D. Parker, A. J. Taberner, M. P. Nash, and P. M. F. Nielsen, "Computational and experimental characterization of skin mechanics: identifying current challenges and future directions," *WIREs Syst Biol Med*, vol. 5, no. 5, pp. 539–556, Sep. 2013.

[48] J. A. Weiss, B. N. Maker, and S. Govindjee, "Finite element implementation of incompressible, transversely isotropic hyperelasticity," *Computer Methods in Applied Mechanics and Engineering*, vol. 135, no. 1–2, pp. 107–128, Aug. 1996.

[49] J. W. Y. Jor, M. P. Nash, P. M. F. Nielsen, and P. J. Hunter, "Estimating material parameters of a structurally based constitutive relation for skin mechanics," *Biomech Model Mechanobiol*, vol. 10, no. 5, pp. 767–778, Oct. 2011.

[50] T. C. Gasser, R. W. Ogden, and G. A. Holzapfel, "Hyperelastic modelling of arterial layers with distributed collagen fibre orientations," *Journal of The Royal Society Interface*, vol. 3, no. 6, pp. 15–35, Feb. 2006.

[51] K. Holmstrand, J. J. Longacre, and G. A. Destefano, "THE ULTRASTRUCTURE OF COLLAGEN IN SKIN, SCARS AND KELOIDS," *Plastic and Reconstructive Surgery*, vol. 27, no. 6, p. 597, Jun. 1961.

[52] B. J. Wilhelmi, S. J. Blackwell, and L. G. Phillips, "Langer's Lines: To Use or Not to Use," *Plastic and Reconstructive Surgery*, vol. 104, no. 1, p. 208, Jul. 1999.

[53] S. W. Carmichael, "The tangled web of Langer's lines," *Clinical Anatomy*, vol. 27, no. 2, pp. 162–168, 2014.

[54] G. Dupuytren, *Traité théorique et pratique des blessures par armes de guerre*. H. Dumont, 1835.

[55] K. Langer, "On the anatomy and physiology of the skin," *British Journal of Plastic Surgery*, vol. 31, no. 1, pp. 3–8, Jan. 1978.

[56] J. C. Waldorf, G. Perdikis, and S. P. Terkonda, "Planning incisions," *Operative Techniques in General Surgery*, vol. 4, no. 3, pp. 199–206, Sep. 2002.

[57] C. J. Kraissl, "THE SELECTION OF APPROPRIATE LINES FOR ELECTIVE SURGICAL INCISIONS," *Plastic and Reconstructive Surgery*, vol. 8, no. 1, p. 1, Jul. 1951.

[58] A. F. Borges, "Relaxed skin tension lines (RSTL) versus other skin lines," *Plast Reconstr Surg*, vol. 73, no. 1, pp. 144–150, Jan. 1984.

[59] A. F. Borges and J. E. Alexander, "Relaxed skin tension lines, z-plasties on scars, and fusiform excision of lesions," *British Journal of Plastic Surgery*, vol. 15, pp. 242–254, Jan. 1962.

[60] P. A. Dabnichki, A. D. Crocombe, and S. C. Hughes, "Deformation and Stress Analysis of Supported Buttock Contact," *Proceedings of the IMechE*, vol. 208, no. 1, pp. 9–17, Mar. 1994.

[61] T. Brosh and M. Arcan, "Modeling the body/chair interaction – an integrative experimental–numerical approach," *Clinical Biomechanics*, vol. 15, no. 3, pp. 217–219, 2000.

[62] E. Linder-Ganz, N. Shabshin, Y. Itzchak, Z. Yizhar, I. Siev-Ner, and A. Gefen, "Strains and stresses in sub-dermal tissues of the buttocks are greater in paraplegics than in healthy during sitting," *Journal of Biomechanics*, vol. 41, no. 3, pp. 567–580, 2008.

[63] D. Lim, F. Lin, R. W. Hendrix, B. Moran, C. Fasanati, and M. Makhsous, "Evaluation of a new sitting concept designed for prevention of pressure ulcer on the buttock using finite element analysis," *Med Bio Eng Comput*, vol. 45, no. 11, pp. 1079–1084, Nov. 2007.

[64] W. W. Chow and E. I. Odell, "Deformations and Stresses in Soft Body Tissues of a Sitting Person," *J Biomech Eng*, vol. 100, no. 2, pp. 79–87, May 1978.

[65] E. M. H. Bosboom, M. K. C. Hesselink, C. W. J. Oomens, C. V. C. Bouten, M. R. Drost, and F. P. T. Baaijens, "Passive transverse mechanical properties of skeletal muscle under in vivo compression," *Journal of Biomechanics*, vol. 34, no. 10, pp. 1365–1368, Oct. 2001.

[66] N. Moes and I. Horváth, "Finite elements model of the human body: geometry and non-linear material properties," in *Proceedings of the TMCE*, 2002, vol. 2002.

[67] K. K. Ceelen *et al.*, "Validation of a Numerical Model of Skeletal Muscle Compression With MR Tagging: A Contribution to Pressure Ulcer Research," *J Biomech Eng*, vol. 130, no. 6, pp. 061015-061015–8, Oct. 2008.

[68] E. Linder-Ganz and A. Gefen, "The Effects of Pressure and Shear on Capillary Closure in the Microstructure of Skeletal Muscles," *Ann Biomed Eng*, vol. 35, no. 12, pp. 2095–2107, Dec. 2007.

[69] R. M. A. Al-Dirini, M. P. Reed, and D. Thewlis, "Deformation of the gluteal soft tissues during sitting," *Clinical Biomechanics*, vol. 30, no. 7, pp. 662–668, Aug. 2015.

[70] S. E. Sonenblum, S. H. Sprigle, J. M. Cathcart, and R. J. Winder, "3D anatomy and deformation of the seated buttocks," *Journal of Tissue Viability*, vol. 24, no. 2, pp. 51–61, May 2015.

[71] B. A. Todd and J. G. Thacker, "Three-dimensional computer model of the human buttocks, in vivo," *Journal of Rehabilitation Research and Development; Washington*, vol. 31, no. 2, pp. 111–9, 1994.

[72] W. Sun and M. S. Sacks, "Finite element implementation of a generalized Fung-elastic constitutive model for planar soft tissues," *Biomech Model Mechanobiol*, vol. 4, no. 2–3, pp. 190–199, Nov. 2005.

[73] G. A. Holzapfel, T. C. Gasser, and R. W. Ogden, "Comparison of a Multi-Layer Structural Model for Arterial Walls With a Fung-Type Model, and Issues of Material Stability," *J Biomech Eng*, vol. 126, no. 2, pp. 264–275, May 2004.

[74] Y. Lanir and Y. C. Fung, "Two-dimensional mechanical properties of rabbit skin—II. Experimental results," *Journal of biomechanics*, vol. 7, no. 2, pp. 171IN9175–174182, 1974.

[75] Z. Liu and K. Yeung, "The preconditioning and stress relaxation of skin tissue," *Journal of Biomedical & Pharmaceutical Engineering*, vol. 2, no. 1, pp. 22–28, 2008.

[76] A. Karimi, M. Navidbakhsh, M. Haghighatnama, and A. M. Haghi, "Determination of the axial and circumferential mechanical properties of the skin tissue using experimental testing and constitutive modeling," *Computer Methods in Biomechanics and Biomedical Engineering*, vol. 18, no. 16, pp. 1768–1774, Dec. 2015.

[77] H. S. Ranu, "Effects of radiotherapy on the mechanical properties of human skin," *IEEE Engineering in Medicine and Biology Magazine*, vol. 10, no. 2, pp. 55–57, Jun. 1991.

[78] E. Balli *et al.*, "Exposure to gamma rays induces early alterations in skin in rodents: Mechanical, biochemical and structural responses," *Ecotoxicology and environmental safety*, vol. 72, no. 3, pp. 889–894, 2009.

[79] M. Ottenio, D. Tran, A. Ní Annaidh, M. D. Gilchrist, and K. Bruyère, "Strain rate and anisotropy effects on the tensile failure characteristics of human skin," *Journal of the Mechanical Behavior of Biomedical Materials*, vol. 41, pp. 241–250, Jan. 2015.

[80] H. G. Vogel and K. Denkel, "In vivo recovery of mechanical properties in rat skin after repeated strain," *Arch Dermatol Res*, vol. 277, no. 6, pp. 484–488, 1985.

[81] A. Delalleau, G. Josse, J.-M. Lagarde, H. Zahouani, and J.-M. Bergheau, "A nonlinear elastic behavior to identify the mechanical parameters of human skin in vivo," *Skin research and Technology*, vol. 14, no. 2, pp. 152–164, 2008.

[82] S. Luebberding, N. Krueger, and M. Kerscher, "Mechanical properties of human skin in vivo: a comparative evaluation in 300 men and women," *Skin Res Technol*, vol. 20, no. 2, pp. 127–135, May 2014.

[83] A. Ní Annaidh, K. Bruyère, M. Destrade, M. D. Gilchrist, and M. Otténio, "Characterization of the anisotropic mechanical properties of excised human skin," *Journal of the Mechanical Behavior of Biomedical Materials*, vol. 5, no. 1, pp. 139–148, Jan. 2012.

[84] C. Bellini, J. Ferruzzi, S. Roccabianca, E. S. Di Martino, and J. D. Humphrey, "A Microstructurally Motivated Model of Arterial Wall Mechanics with Mechanobiological Implications," *Ann Biomed Eng*, vol. 42, no. 3, pp. 488–502, Mar. 2014.

[85] J. Ferruzzi, M. R. Bersi, and J. D. Humphrey, "Biomechanical Phenotyping of Central Arteries in Health and Disease: Advantages of and Methods for Murine Models," *Ann Biomed Eng*, vol. 41, no. 7, pp. 1311–1330, Jul. 2013.

[86] R. H. Hoyt, S. M. Collins, D. J. Skorton, E. E. Ericksen, and D. Conyers, "Assessment of fibrosis in infarcted human hearts by analysis of ultrasonic backscatter.," *Circulation*, vol. 71, no. 4, pp. 740–744, Apr. 1985.

[87] L. Rich and P. Whittaker, "Collagen and picrosirius red staining: a polarized light assessment of fibrillar hue and spatial distribution," *Braz J Morphol Sci*, vol. 22, no. 2, pp. 97–104, 2005.

[88] P. Arun Gopinathan, G. Kokila, M. Jyothi, C. Ananjan, L. Pradeep, and S. Humaira Nazir, "Study of Collagen Birefringence in Different Grades of Oral Squamous Cell Carcinoma Using Picrosirius Red and Polarized Light Microscopy," *Scientifica*, 2015. [Online]. Available: https://www.hindawi.com/journals/scientifica/2015/802980/abs/. [Accessed: 27-Sep-2017].

[89] R. Rezakhaniha *et al.*, "Experimental investigation of collagen waviness and orientation in the arterial adventitia using confocal laser scanning microscopy," *Biomech Model Mechanobiol*, vol. 11, no. 3–4, pp. 461–473, Mar. 2012.

[90] S. Zeinali-Davarani, Y. Wang, M.-J. Chow, R. Turcotte, and Y. Zhang, "Contribution of Collagen Fiber Undulation to Regional Biomechanical Properties Along Porcine Thoracic Aorta," *J Biomech Eng*, vol. 137, no. 5, p. 051001, May 2015.

[91] S. Baek, R. L. Gleason, K. R. Rajagopal, and J. D. Humphrey, "Theory of small on large: Potential utility in computations of fluid–solid interactions in arteries," *Computer Methods in Applied Mechanics and Engineering*, vol. 196, no. 31, pp. 3070–3078, Jun. 2007.

[92] F. Auriol, L. Vaillant, L. Machet, S. Diridollou, and G. Lorette, "Effects of short-time hydration on skin extensibility.," *Acta Derm Venereol*, vol. 73, no. 5, pp. 344–347, Oct. 1993.

[93] M. J. Muñoz *et al.*, "An experimental study of the mouse skin behaviour: Damage and inelastic aspects," *Journal of Biomechanics*, vol. 41, no. 1, pp. 93–99, 2008.

[94] E. Guan, S. Smilow, M. Rafailovich, and J. Sokolov, "Determining the Mechanical Properties of Rat Skin with Digital Image Speckle Correlation," *DRM*, vol. 208, no. 2, pp. 112–119, 2004.

[95] H. Takeuchi *et al.*, "Usefulness of Rat Skin as a Substitute for Human Skin in the in Vitro Skin Permeation Study," *Experimental Animals*, vol. 60, no. 4, pp. 373–384, 2011.

[96] J. C. J. Wei, G. A. Edwards, D. J. Martin, H. Huang, M. L. Crichton, and M. A. F. Kendall, "Allometric scaling of skin thickness, elasticity, viscoelasticity to mass for micro-medical device translation: from mice, rats, rabbits, pigs to humans," *Scientific Reports*, vol. 7, no. 1, p. 15885, Nov. 2017.

[97] C. You, X. Wang, Y. Zheng, and C. Han, "Three types of dermal grafts in rats: the importance of mechanical property and structural design," *Biomed Eng Online*, vol. 12, p. 125, Dec. 2013.

[98] C. Escoffier, J. de Rigal, A. Rochefort, R. Vasselet, J.-L. Lévêque, and P. G. Agache, "Age-related mechanical properties of human skin: an in vivo study," *Journal of Investigative Dermatology*, vol. 93, no. 3, 1989.

[99] R. C. Haut, "The Effects of Orientation and Location on the Strength of Dorsal Rat Skin in High and Low Speed Tensile Failure Experiments," *J Biomech Eng*, vol. 111, no. 2, pp. 136–140, May 1989.

[100] R. E. Billingham and P. B. Medawar, "The Freezing, Drying and Storage of Mammalian Skin," *Journal of Experimental Biology*, vol. 29, no. 3, pp. 454–468, Sep. 1952.

[101] J. P. Webster, "Refrigerated Skin Grafts," *Ann Surg*, vol. 120, no. 4, pp. 431–448, Oct. 1944.

[102] R. Briggs and L. Jund, "Successful grafting of frozen and thawed mouse skin," *Anat. Rec.*, vol. 89, no. 1, pp. 75–85, May 1944.

[103] R. D. Marangoni *et al.*, "Effect of Storage and Handling Techniques on Skin Tissue Properties," *Annals of the New York Academy of Sciences*, vol. 136, no. 16, pp. 441–453, Nov. 1966.

[104] T. L. Foutz, E. A. Stone, and C. F. Abrams, Jr., "Effects of freezing on mechanical properties of rat skin.," *Am J Vet Res*, vol. 53, no. 5, pp. 788–792, May 1992.

[105] C. Flynn, M. B. Rubin, and P. Nielsen, "A model for the anisotropic response of fibrous soft tissues using six discrete fibre bundles," *International Journal for Numerical Methods in Biomedical Engineering*, vol. 27, no. 11, pp. 1793–1811, Nov. 2011.

[106] Z. Sadler, J. Scott, J. Drost, S. Chen, S. Roccabianca, and T. R. Bush, "Initial estimation of the in vivo material properties of the seated human buttocks and thighs," *International Journal of Non-Linear Mechanics*, Oct. 2018.

[107] B. Alexis, "James (Human Body for scale) | 3D CAD Model Library | GrabCAD," *GRABCAD*, 22-Aug-2016. [Online]. Available: https://grabcad.com/library/james-human-body-for-scale-1. [Accessed: 10-Apr-2018].

[108] S. Strandberg, M.-L. Wretling, T. Wredmark, and A. Shalabi, "Reliability of computed tomography measurements in assessment of thigh muscle cross-sectional area and attenuation," *BMC Medical Imaging*, vol. 10, p. 18, Aug. 2010.

[109] C. C. Gordon *et al.*, "Anthropometric Survey of U.S. Army Personnel: Summary Statistics, Interim Report for 1988," Anthropology Research Project Inc., Yellow Springs, OH, Mar. 1989.

[110] A. C. Looker, T. J. Beck, and E. S. Orwoll, "Does Body Size Account for Gender Differences in Femur Bone Density and Geometry?," *J Bone Miner Res*, vol. 16, no. 7, pp. 1291–1299, Jul. 2001.

[111] R. S. Rivlin, "Large elastic deformations of isotropic materials. I. Fundamental concepts," *Phil. Trans. R. Soc. Lond. A*, vol. 240, no. 822, pp. 459–490, Jan. 1948.

[112] R. S. Rivlin, "Large elastic deformations of isotropic materials VI. Further results in the theory of torsion, shear and flexure," *Phil. Trans. R. Soc. Lond. A*, vol. 242, no. 845, pp. 173–195, Dec. 1949.

[113] R. W. Ogden, "Large deformation isotropic elasticity – on the correlation of theory and experiment for incompressible rubberlike solids," *Proc. R. Soc. Lond. A*, vol. 326, no. 1567, pp. 565–584, Feb. 1972.

[114] G. A. Ateshian and K. D. Costa, "A frame-invariant formulation of Fung elasticity," *Journal of Biomechanics*, vol. 42, no. 6, pp. 781–785, Apr. 2009.

[115] B. Manafi-Khanian, L. Arendt-Nielsen, and T. Graven-Nielsen, "An MRI-based leg model used to simulate biomechanical phenomena during cuff algometry: a finite element study," *Med Biol Eng Comput*, vol. 54, no. 2, pp. 315–324, Mar. 2016.

[116] E. Silva, M. Parente, S. Brandão, T. Mascarenhas, and R. Natal Jorge, "Characterizing the Biomechanical Properties of the Pubovisceralis Muscle Using a Genetic Algorithm and the Finite Element Method," *J Biomech Eng*, vol. 141, no. 1, pp. 011009-011009–11, Oct. 2018.

[117] K. M. Myers *et al.*, "A continuous fiber distribution material model for human cervical tissue," *Journal of Biomechanics*, vol. 48, no. 9, pp. 1533–1540, Jun. 2015.

[118] H. Kanehisa, S. Ikegawa, and T. Fukunaga, "Comparison of muscle cross-sectional area and strength between untrained women and men," *Europ. J. Appl. Physiol.*, vol. 68, no. 2, pp. 148–154, Feb. 1994.

[119] C. Mergl, T. Anton, R. Madrid-Dusik, J. Hartung, A. Librandi, and H. Bubb, "Development of a 3D Finite Element Model of Thigh and Pelvis," SAE International, Warrendale, PA, SAE Technical Paper 2004-01–2132, Jun. 2004.

[120] R. M. A. Al-Dirini, J. Nisyrios, M. P. Reed, and D. Thewlis, "Quantifying the in vivo quasi-static response to loading of sub-dermal tissues in the human buttock using magnetic resonance imaging," *Clinical Biomechanics*, vol. 50, pp. 70–77, Dec. 2017.

[121] S. Diridollou *et al.*, "In vivo model of the mechanical properties of the human skin under suction," *Skin Research and Technology*, vol. 6, no. 4, pp. 214–221, 2000.

[122] A. Laurent *et al.*, "Echographic measurement of skin thickness in adults by high frequency ultrasound to assess the appropriate microneedle length for intradermal delivery of vaccines," *Vaccine*, vol. 25, no. 34, pp. 6423–6430, Aug. 2007.

[123] H. Alexander and T. Cook, "Variations With Age In The Mechanical Properties of Human Skin in Vivo," in *Bed Sore Biomechanics*, R. M. Kenedi and J. M. Cowden, Eds. Macmillan Education UK, 1976, pp. 109–117.

[124] F. M. Hendriks, D. Brokken, J. T. W. M. V. Eemeren, C. W. J. Oomens, F. P. T. Baaijens, and J. B. a. M. Horsten, "A numerical-experimental method to characterize the non-linear mechanical behaviour of human skin," *Skin Research and Technology*, vol. 9, no. 3, pp. 274–283, 2003.

[125] S. Shacham, D. Castel, and A. Gefen, "Measurements of the Static Friction Coefficient Between Bone and Muscle Tissues," *J Biomech Eng*, vol. 132, no. 8, pp. 084502-084502–4, Jun. 2010.